MULTI-SPECIES DYNAMIC RESPONSE AND KINETIC PHENOMENA IN HIGH ENERGY DENSITY PLASMAS

By

Thomas Chuna

A DISSERTATION

Submitted to
Michigan State University
in partial fulfillment of the requirements
for the degree of

Physics—Doctor of Philosophy
Computational Mathematics, Science, and Engineering—Dual Major

Dec 7, 2023

ABSTRACT

High energy density (HED) science, concerned with matter at pressures in excess of 1 MBar, investigates the processes occurring inside nuclear fusion and giant planets, enhancing our understanding of the universe's most energetic events. This work contains three primary results. First, we incorporate conservation of momentum into the collisional multi-species dynamic response models. Second, we extend the single species hybrid kinetic-fluid model of Degond et al. [Degond, Pierre, Shi Jin, and Luc Mieussens. JCP 209.2 (2005): 665-694] to multi-species. Third, we present data-driven observations of system equilibration, which can assess the quality of machine-learned model closures in extended moment hydrodynamics. Each result uses expansions about equilibrium, but contributes to HED science in different ways.

Measuring the material properties of HED matter is challenging since they exist for a short time in a confined space at conditions that damage nearby equipment. Thus, experimental diagnostics rely on scattered and emitted electromagnetic spectra to investigate material properties. Connecting the spectra to material properties requires theoretical models of dynamic response. Typical dynamic response models include the Mermin model, predicting Drude-like conductivity [Mermin, N. David. PRB 1.5 (1970): 2362], and the Drude-Smith model, predicting non-Drude-like conductivity [Smith, N. V. PRB 64.15 (2001): 155106]. However, the often used Mermin model of dynamic response does not satisfy the relevant sum rules, and the Drude-Smith model lacks interpretability. In this dissertation, we include number and momentum conserving multi-species collisions to develop a new dynamic dielectric function for multi-species plasmas which satisfies relevant sum rules. We demonstrate the impact of each conservation law on the predicted dynamic structure factor of a pure deuterium-tritium (DT) HED plasma as well as a carbon contaminated (DT) HED plasma. Additionally, we present a new dynamic non-Drude conductivity model that has a clear interpretation. Comparing our conductivity model to the Drude-Smith conductivity model, we conclude that Smith's intensely debated phenomenological parameter violates local number conservation.

Simulations are conducted to complement and inform HED experiments. Historically, HED

scientists have used radiation–hydrodynamic codes. However, Eulerian codes assume the mean free path in the plasma is infinitesimally small, placing the system in local equilibrium. This assumption neglects dissipation and forces species in the same location to share a bulk velocity and temperature. Current codes correct for dissipation, which improves predictions, but they cannot correct for velocity and temperature separation. A fully kinetic code could account for these phenomena, but such a code is computationally infeasible for realistic 3D simulations. In this dissertation, we present a hybrid model which can smoothly transition between Haack et al.'s multi-species kinetic PDE [Haack, Hauck and Murillo, J. Stat. Phys. 168, 4] and multi-species hydrodynamic PDEs. We validate the hybrid model on the Sod shock problem and then investigate multi-species mixing in HED experiments. Within our simulation, we identify electro-diffusion at the interfaces as well as persistent velocity and temperature separation between species, phenomena that are missed by purely hydrodynamic codes.

As an alternative to hybrid models, extended moment hydrodynamic models can be employed [Hoffman, Nelson M., et al. Physics of Plasmas 22.5 (2015)]. However, to close the hierarchy of moments, these models often assume local equilibrium. Machine learning is an emerging approach to the moment closure problem, which can avoid such assumptions. We construct a complex-valued, multi-step neural network to close Grad's extended moment equations [Grad, Harold. Comm. pure and applied mathematics 2.4 (1949): 331-407]. Additionally, the quality of a closure is typically assessed in terms of its ability to describe diffusion/dissipation and its long time stability. We use dimension reduction techniques and dynamic mode decomposition to observe the equilibration process. This collection of data-driven techniques provides new metrics to assess a neural network's ability to inform on dissipation.

ACKNOWLEDGEMENTS

Chapter 4 of this work was supported by the U.S. Department of Energy through the Los Alamos National Laboratory. Los Alamos National Laboratory is operated by Triad National Security, LLC, for the National Nuclear Security Administration of U.S. Department of Energy (Contract No. 89233218CNA000001). Research presented in this article/presentation/report was supported by the Laboratory Directed Research and Development program of Los Alamos National Laboratory under project number 20190005DR. Chapter 5 of this work was performed under the auspices of the U.S. Department of Energy by Lawrence Livermore National Laboratory under contract DE-AC52-07NA27344 Lawrence National Security, LLC.

I acknowledge the academic advisors from Michigan State University and Wittenberg University. First, I acknowledge my PhD advisor Michael Murillo. I thank Michael for expanding my presentation and publication skill set as well as my knowledge of machine learning. I recognize the patience it took to help me express ideas succinctly and the skill it took to select relevant projects that were within my reach. I acknowledge Alexei Bazavov, under whom I earned my MSc, I thank Alexei for expanding the number of mathematical tools at my disposal. I acknowledge Elizabeth George, under whom I earned my BSc, I thank Elizabeth George for fostering my curiosity and giving me space and support to explore.

I acknowledge the scientists from Los Almos National Laboratory. Jeff Haack who guided my understanding of near-equilibrium expansions and computational fluid dynamics and Irina Sagert who guided the editing process on my first published paper. As well as the scientists from Lawrence-Livermore National Laboratory. Frank Graziani who guided my understanding of emergent phenomena and Lee Ellison who guided me through his exciting post-doctoral research.

I acknowledge the members of the MSU community who have helped my along my professional path. To my committee members (in alphabetical order): Metin Aktulga, Wade Fisher, Michael Murillo, Brian O'Shea, and Scott Pratt, after many committee meetings, I was not sure I would make it, but we have arrived at a dissertation. I acknowledge Kim Crosslan, Remco Zegers, and Steve Zeph who maintain Michigan State's physics graduate program. To the veteran MurilloLab

members David, Lucciano, and Luke your support and many sanity checks were crucial. To new members: Zach, Chris, Jorge, and Yannick, I wish the absolute best. Additionally to: Yannis, Yash, and Alejandro, I wish the absolute best.

I acknowledge the many personal connections that sustained my emotional well-being. To my family: Karen, Trevor, Alex, Kelsie, Erin, Eric, Trevor, Pam, and the cousins Sam, Keith, Gabe, Kyle, Sarah, thank you for your unending lines of communication. To Camila Monsalve Avendaño, I will be with you tomorrow. To my Michigan State friends: Alyssa Turcsak and Corey Cooling, Abbie Cathcart and Isaac Yandow, Maggie Magilligan and Morgan Koetje, Tom-Erik Haugen and Adam Anthony, Tamas Budner and Kyle Krowpman, Meredith Wagner and Tino Burse, Roy Salinas, Jordan Owens-Fryer, Tracy Edwards, Dan Salazar, Mostafa Ali, Camille Mikolas, Sheng Lee thank for helping me heal. To my loved ones: Jordan, Sage, Alex **Q**uinn **D**urham, Guillermo, TK(fire!), Wam Sitman, Senor, Autumn Hill and the Hills, That1kid, and Yung Grady, thank you for balancing me. To Margaret Dutko and Thomas E. Chuna may you rest in peace.

To everyone I have named here, I let my stress prevent me from cherishing our connections; I have learned my lesson and I look forward to loving more.

TABLE OF CONTENTS

LIST OF TABLES

LIST OF FIGURES

CHAPTER 1

INTRODUCTION

1.1 Definition of Plasma

Plasmas are systems of charged particles formed through ionization, the process where electrons are stripped from atoms, creating a mix of free electrons and ions, *i.e.*, atoms that have lost electrons. Traditionally, physicists are first exposed to ionization in the context of spectroscopy or the Einstein work function. In these cases, ionization occurs in the presence of electromagnetic radiation. However, ionization can occur if the system's thermal energy is high enough for electrons to be knocked loose by collisions. Additionally, ionization can occur if the system's pressure is high enough for electrons to be squeezed from their bound states. Examples of plasmas can be found looking up at the night sky. Stars are massive plasma spheres undergoing thermonuclear fusion. While thermonuclear fusion can be initiated here on earth, it is not yet an energy source like the sun is. Currently, plasmas are utilized in industrial processes.

The properties of a plasma are distinct from a solid, liquid, or gas because the constituents of the plasma carry charge. The presence of charge leads to two key properties. The first property is "quasi-neutrality" meaning that number of positive and negative charges in a plasma tends to balance out over large distances, resulting in an overall electrically neutral medium. The second property is "collective behavior" meaning that the long range of the Coulomb force gives rise to emergent phenomena, *i.e.*, behavior that only occurs when many particles interact simultaneously. Violations of either of these two properties (*e.g*, non-neutral plasmas [1]) are interesting and hence the exceptions prove the rule.

Plasmas exhibit quasi-neutrality because of charge conservation; when a free electron is created in a plasma, an ion is also created. However, even if the plasma is globally neutral, there will be local fluctuations in the charge. Fluctuations refer to sub-domains that are not charge-neutral. Assuming the plasma is in thermodynamic equilibrium, the local deviations in the average charge,

which arise from particle interactions, are [2, section 116]

$$\langle e\delta n(r)\rangle = en_0\left(e^{-e\Phi(r)/T} - 1\right). \tag{1.1}$$

Here $\Phi(r)$ is the average potential per particle and T has units of eV.

A system's tendency towards quasi-neutrality can be seen from a back-of-the-envelope calculation [3]. Consider a charged particle system of electrons and ions with number density n_e and n_I respectively. Consider a sphere of fully ionized hydrogen plasma with radius $r = 10^{-3}$ and ion number density $n_I = 10^{20}$. Assume the electron number density is 1% smaller $n_e = 0.99n_I$, then the total charge in the sphere is

$$Q_{\text{net}} = \frac{4}{3}\pi r^3 \frac{en_I}{100} \tag{1.2}$$

and the electric potential at the surface would be

$$\Phi = \frac{1}{4\pi\epsilon_0}\frac{Q_{\text{net}}}{r} = \frac{r^2 e}{3\epsilon_0}\frac{n_I}{100} \tag{1.3}$$

where ϵ_0 is the permittivity of free space. Evaluating this expression indicates that the potential on our plasma's surface is approximately 6000 volts, enough to create a 2 mm electrical arc through air (also more than double the voltage used in Nebraska's electric chair executions) [4]. In short, violating quasi-neutrality produces an electric potential which attempts to rectify the uneven distribution, thus it takes a lot of work to create macroscopic charge imbalances.

Collective phenomena occur in plasmas because the long range electromagnetic force allows a single charged particle to influence and be influenced by many charged particles. Consider a test charge in a volume of plasma; a sub-volume of plasma located a distance r away acts on the test charge with a force that diminishes as $1/r^2$. However, for a given solid angle (that is, where $\Delta r/r$ = constant), the volume of plasma acting on the test charge increases as r^3. [5, section 1.2]. Therefore, while any one particle from the plasma has little impact, the collection of particles can impact the test charge.

A quick derivation shows that background charges screen a test charge's potential. Consider Poisson's equation

$$-\frac{1}{4\pi}\nabla^2\Phi(r) = e\delta n(r) + Q\delta(r) \tag{1.4}$$

where $e\delta n(r)$ is the local deviation from uniform charge density, given in Eq(1.1), and $Q\delta(r)$ is a test charge placed at the origin. In Fourier space, this equation is given as

$$\frac{k^2}{4\pi}\Phi(k) = e\delta n(k) + Q \tag{1.5}$$

Assume that the average potential energy is much greater than the average kinetic energy $U = e\Phi(r) << T$, this is known as the "weakly coupled" limit. Then Eq(1.1) gives $\delta n(k) = -n_0 eV(k)/T$. Inserting this expression into the Poisson equation Eq(1.5) yields the screened-Coulomb potential

$$\Phi(k) = 4\pi\frac{Q}{k^2 + k_D^2}, \tag{1.6}$$

where $k_{D,e} = \frac{4\pi n_e e^2}{T}$ is the Debye wavenumber. In short, by allowing many electrons to redistribute themselves, test charges interact with other charges via a screened charge.

Another well known collective phenomenon is plasma oscillation or, if quantized, the plasmonic mode. A quick derivation can expose a plasma's ability to produce plasmonic modes. Consider a slab of quasi-neutral plasma

$$n_e = \sum_i Z_i n_i, \tag{1.7}$$

where Z_i is the effective ionization of the i^{th} species and n_i is uniform. If we displace the electrons by an infinitesimal distance δx, the portions of the ions and the displaced electrons that do not overlap are effectively like two plates of a capacitor, each with a surface charge $\sigma = \pm e n_e \delta x$. The resulting electric field is uniform $E = 4\pi\sigma = 4\pi e n_e \delta x$. Because the mass of the ions is much greater than the mass of the electrons we approximate the ions as stationary and consider the motion of the electrons. The electrons feel a force

$$F \equiv m_e \ddot{\delta x}, \tag{1.8}$$

$$F = -eE(\delta x) = -4\pi e^2 n \delta x, \tag{1.9}$$

which together describe an oscillatory equation of motion

$$\ddot{\delta x} = -\omega_p^2 \delta x. \tag{1.10}$$

Here $\omega_{p,e} = \sqrt{\frac{4\pi e^2 n_e}{m_e}}$ is known as the electron plasma frequency.

Together, charge fluctuation, charge screening, and plasma oscillation form a small subset of the rich and interconnected behaviors that are characteristic of plasmas. Charge fluctuations demonstrate that free electrons have non-trivial local arrangements, while maintaining global charge neutrality. Non-trivial local charge arrangements lead to charge screening, which alter the interactions between particles in a plasma. Charged particle interactions give rise to collective behavior like plasma oscillations. Investigating the characteristic behaviors enables plasma scientists to utilize plasmas in new technologies.

1.2 Classification of a Plasma

Plasmas exist across a wide range of number densities and temperatures. It is useful to classify the various types of plasma in ρT space (density-temperature space) with a collection of dimensionless parameters. Further, these dimensionless parameters are often expansion parameters in derivation, *e.g.*, the weakly coupled limit.

The first dimensionless plasma parameter we focus on is the coupling parameter Γ which is the ratio of an ion's average potential energy from ion-ion interactions with the ion's average kinetic energy

$$\Gamma = \frac{4\pi e^2}{a_s T}. \tag{1.11}$$

Here $a_s = (3n_e/4\pi)^{1/3}$ is the Wigner-Sietz radius, the average distance between ions in a plasma. $\Gamma \ll 1$ indicates a weakly coupled plasma where kinetic energy dominates. This is the assumption we used to derive screened Coulomb Eq(1.6). Whereas $\Gamma \gg 1$, implies a strongly coupled plasma. In contrast with the screened Coulomb interaction, a purely repulsive force, we expect that the ion-ion interactions acquire attractive wells in the strongly coupled limit [6, chapter 10].

The dimensionless quantum degeneracy parameter Θ is the ratio of the electron's average kinetic

energy at a given temperature T to its kinetic energy at $T = 0$, *i.e.*, its Fermi energy

$$\Theta = \frac{T}{E_F}. \tag{1.12}$$

Θ is crucial in characterizing the significance of quantum effects. When $\Theta \ll 1$ the electrons interact with each other as a quantum degenerate fermi gas; the thermal de Broglie wavelength exceeds the interatomic spacing. Conversely, $\Theta \gg 1$ indicates electrons follow a Maxwellian distribution, where quantum effects can be neglected.

A collection of hydrogen (H) plasmas, along with their respective densities, temperatures, and dimensionless parameters, are listed in Table 1.1. These example plasmas are plotted on a heat map of H's ionization in Figure 1.1. The Saha ionization estimates for both ideal and Van der Waal's equation of state (EoS) were computed using [7]

$$\frac{Z^2}{1-Z} = \frac{1}{n_H}\left(\frac{2\pi m_e T}{h^2}\right)^{3/2} e^{E_{H-I1}/T} \tag{1.13}$$

where $E_{H-I1} = -13.6$ eV the ionization energy of an electron in the Hydrogen ground state. The Thomas-Fermi ionization heat map was generated using More's Thomas-Fermi fit [8, Table IV]. The 1 MBar pressure line was generated using the ideal gas equation of state.

Table 1.1 Table identifying the density ρ, temperature T, ion-ion coupling parameter Γ, and electron degeneracy parameter Θ of various plasmas. Omega indicates the density and temperature at peak capsule compression for Omega's direct drive inertial confinement fusion (ICF) experiments [9]. National Ignition Facility (NIF) estimates reflect density and temperature achieved at peak capsule compression from in-direct drive inertial ICF experiments [10].

Physical System	ρ (g/cc)	T (eV)	Γ	Θ
Typical Fusion Reactor [5]	4.2×10^{-5}	1.0×10^{2}	0.007	≈ 0
Ideal Fusion Reactor [5]	4.2×10^{-4}	3.0×10^{4}	≈ 0	≈ 0
Lightning [11]	1.3×10^{-4}	2.1×10^{0}	0.184	0.023
Jupiter Interior [12] [13]	3.0×10^{1}	2.2×10^{0}	7.68	20.72
Omega [9]	1.8×10^{2}	3.4×10^{2}	0.290	2.350
Solar Interior [14]	1.5×10^{2}	1.3×10^{3}	0.076	0.560
National Ignition Facility [10]	1.5×10^{3}	1.4×10^{4}	0.015	0.240
White Dwarf [15]	$> 10^{4}$	> 1	10^{3}	10^{4}

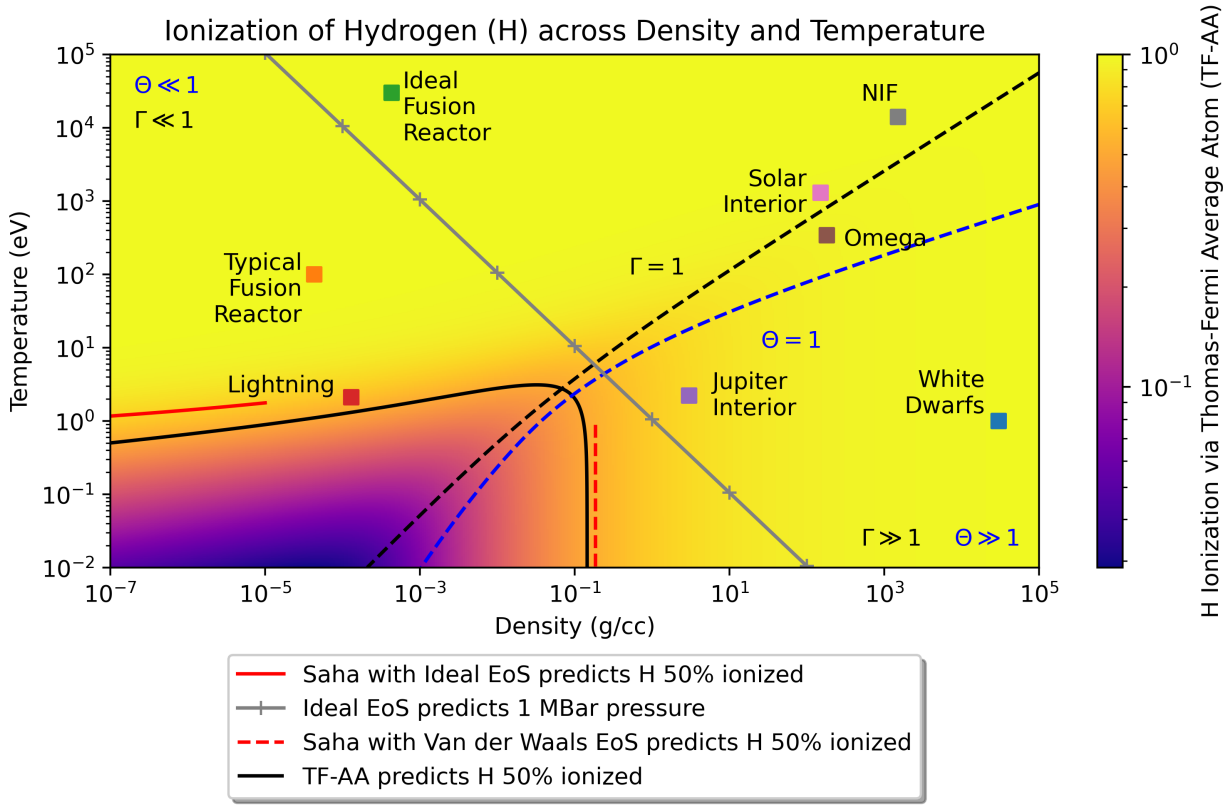

Figure 1.1 Plot mapping the ionization of hydrogen across density and temperature space. Different plasma examples from Table 1.1 are plotted for comparison. We see that the National Ignition Facility (NIF) and the Omega laser facility (OMEGA) can generate matter within the high energy density region (> 1 MBar)

1.3 High Energy Density Science

The upper right portion of ρT space is the high energy density (HED) regime, defined as having a pressure in excess of 1 Mbar [16]. HED can be loosely understood as the regime that is too dense for ideal plasma theory to work [5]. A subsection of the HED regime is the warm dense matter (WDM) regime, located in ρT space between the ideal gas regime (low ρ and high T) and the solid state regime (high ρ and low T). WDM is characterized as having an ion-ion coupling parameter Γ and an electron quantum degeneracy parameter Θ of order 1 [17].

In experimental settings, HED plasmas can be produced with direct laser drive, laser driven hohlraums (*i.e.* indirect laser drive), Z-pinches, ultra-fast lasers, or high energy density beams [5]. The final two methods, ultra-fast and high energy density lasers, produce pressure greater than a MBar by creating hot and fast (*i.e.* relativistic) charged particles. Such systems are not extremely

dense. Alternatively, the first three methods (in/direct drive and Z pinch) use inertial confinement to create a plasma that is warm and dense, where the combination of high densities and temperatures produce pressures in excess of 1 MBar.

This dissertation centers on high energy density plasmas created through inertial confinement. This approach is taken in the Laboratory for Laser Energetic (LLE) Omega laser system, Lawrence Livermore's National Laboratory's (LLNL) National Ignition Facility (NIF), and Sandia National Laboratory's (SNL) Z-pinch machine. The basic idea behind inertial confinement is to compress a small capsule that is made of high Z material (*e.g.* diamond/carbon) and filled with deuterium and tritium (DT) gas. Compression is achieved via a collection of high intensity lasers which heat, ionize, and vaporize the high Z shell. As the outer shell explodes radially outward, conservation of momentum causes the inner shell to implode radially inward. This process is known as ablation, and the rapid compression causes the deuterium-tritium fuel to reach extreme densities and temperatures, see Figure 1.1 and Figure 1.1. The energies and densities can get high enough that fusion events are possible, so inertial confinement is often referred to as inertial confinement fusion (ICF).

Experimental diagnostics rely on a collection of techniques to estimate material properties [18]. Since HED matter exists for a short time in a confined space at conditions that damage nearby equipment, scattered and emitted electromagnetic spectra are commonly used in diagnostics. THz waves are used to infer the dynamic conductivity of the HED plasma [19] and X-ray Thompson scattering (XRTS) is used to infer the plasma's properties, i.e., number density, temperature, and ionization [17, 20]. Further, bremsstrahlung radiation emitted from the plasma can be used to observe localized mixing [21, 22]. Each of these experimental diagnostics use an observed signal to fit a parameterized model and thus extract the relevant properties. Therefore, models of a plasma's response to electromagnetic signals enable HED instruments.

A considerable number of semi-empirical and first-principles models have been created to describe the dynamic response of a collisionally damped charged particle system. However, known challenges persist in established dynamic structure factors (DSF), dielectric functions, and conductivities. For instance, the semi-empirical Drude-Smith conductivity [23] lacks interpretability and

the first principles Mermin dielectric function [24] does not satisfy the frequency sum rule [25]. In this dissertation, we will present a new dynamic response function for multi-species plasmas as well as a new dynamic non-Drude conductivity model.

Furthermore, extensive simulations are conducted to compliment and inform HED experiment. Historically, HED scientists have relied on augmenting radiation–hydrodynamic (rad-hydro) codes. For example, the Eulerian rad-hydro code RAGE [26] was upgraded to the xRAGE code to describe ICF experiments [27]. However, Eulerian codes assume the plasma's mean free path divided by its characteristic length (*i.e.* the Knudsen number) is very small and thus the system is in local equilibrium. This assumption removes kinetic phenomena and leads to predictions that do not match experiment. ICF experiments can be parsed into four stages: the early stage, the acceleration stage, the deceleration stage, and the peak-compression/burn stage. Each stage is characterized by unique physical conditions and processes where kinetic effects play crucial roles [10]. A review of kinetic phenomena (*i.e.* non-equilibrium physics) in ICF is given by Renderknecht et al. [28]. Fully kinetic simulations would be able to describe all this behavior, but from a computational perspective such approaches are usually very expensive or simply not feasible. In this dissertation, we investigate computationally efficient methods for including kinetic effects like velocity/temperature separation and dissipative processes (*i.e.* electro-diffusion, baro-diffusion, thermo-diffusion, viscosity, thermal conduction).

The separation of velocity and temperature between species is not accounted for in current radiation-hydrodynamics codes, despite evidence of this phenomenon from experiments [29, 30, 31] and fully kinetic simulations [32]. Eulerian codes cannot account for separation between species because they rely on a single bulk momentum and temperature equation [26, 33, 34]. To use a single transport equation these codes combine species' conductivities into a single cell conductivity [35], but investigations have found that predictions of ICF capsule performance and X-ray flux from vacuum hohlraums are sensitive to how species' conductivies were combined into a cell conductivity [36, 37]. In particular, ICF capsule performance are more sensitive to how species' conductivities were combined into a cell conductivity than to the species' conductivities [36]. Haack et al. has

shown that going beyond local equilibrium (*i.e.*, Eulerian fluids), to a near equilibrium Navier-Stokes assumption, leads to separated velocities, but not temperatures [38]. In this dissertation, we present a new model hybrid model which can smoothly transition between Haack et al.'s kinetic multi-species PDE and multi-species hydrodynamic PDEs. This hybrid model provides computationally efficient kinetics, allowing for both velocity and temperature separation as well as avoiding concocting mixture conductivities, but only where such are needed.

Additionally, dissipation is needed to model inertial confinement. Electro-diffusion is known to rocket particles with a large charge to mass ratios across the interfaces [32, 39, 40]. There are experimental observations at the OMEGA laser facility that suggest electro-, baro-, and thermal-diffusive processes are more important than hydrodynamic instabilities for multi-material mixing [41]. Additionally, experimental observations suggest that viscosity plays an important role in stabilizing the plasmas laser driven shocks propagate through the capsule [42]. Further, studies have shown that viscosity is needed to resolve the discrepancy between simulation and experiment [43, 44]. To account for these dissipative processes, extended moment hydrodynamic equations are employed [45]. In this dissertation, we explore using neural networks as a tool to inform the dissipation in extended moment hydrodynamic simulations. Further, we use dimension reduction techniques and dynamic mode decomposition to quantitatively assess a neural network's ability to inform dissipation.

1.4 Thesis Organization

This thesis addresses current topics in HED physics as described in Section 1.3. Chapter 2 develops the many-body formalism necessary to describe the electromagnetic response of a plasma and non-equilibrium phenomena. Chapter 3 details the electromagnetic response of a collisional multi-species plasma. It derives a multi-species susceptibility from the multi-species Bhatnagar-Gross-Krook (BGK) kinetic equation, introduces a new dynamic non-Drude conductivity model, and presents a one-to-one correspondence between the phenomenological Drude-Smith conductivity and Mermin's number conserving conductivity. Chapter 4 introduces a multi-species kinetic-fluid coupling for high-energy density simulations, deriving a set of coupled partial differ-

ential equations (PDEs) that include both the multi-species BGK model and its limiting Euler or Navier-Stokes hydrodynamic equations. Chapter 5 explores a data-driven approach to incorporating dissipation and methods for assessing the quality of the dissipation. It describes training a neural network to forecast the pressure tensor and heat flux, and employing data compression algorithms and dynamic mode decomposition to characterize the system's invariant manifold. Finally, chapter 6 summarizes and draws major conclusions from the work.

BIBLIOGRAPHY

[1] Ronald C Davidson. *Physics of nonneutral plasmas*. World Scientific Publishing Company, 2001.

[2] Lev Davidovich Landau and Evgenii Mikhailovich Lifshitz. *Statistical Physics: Volume 5*, volume 5. Elsevier, 2013.

[3] José A Bittencourt. *Fundamentals of plasma physics*. Springer Science & Business Media, 2013.

[4] Orders of magnitude (voltage). https://en.wikipedia.org/wiki/Orders_of_magnitude_(voltage). Accessed: 2024-01-15.

[5] R Paul Drake and R Paul Drake. *Introduction to high-energy-density physics*. Springer, 2006.

[6] Jean-Pierre Hansen and Ian Ranald McDonald. *Theory of simple liquids: with applications to soft matter*. Academic press, 2013.

[7] S. Owocki. Stellar astrophysics course notes. https://www.bartol.udel.edu/~owocki/phys633/. Accessed: 2024-01-15.

[8] R.M. More. Pressure ionization, resonances, and the continuity of bound and free states. *Advances in Atomic and Molecular Physics*, 21:305–356, 1985.

[9] S. X. Hu, B. Militzer, V. N. Goncharov, and S. Skupsky. Strong coupling and degeneracy effects in inertial confinement fusion implosions. *Phys. Rev. Lett.*, 104:235003, Jun 2010.

[10] SX Hu, LA Collins, TR Boehly, YH Ding, PB Radha, VN Goncharov, VV Karasiev, GW Collins, SP Regan, and EM Campbell. A review on ab initio studies of static, transport, and optical properties of polystyrene under extreme conditions for inertial confinement fusion applications. *Physics of Plasmas*, 25(5), 2018.

[11] Martin A Uman, Richard E Orville, and Leon E Salanave. The density, pressure, and particle distribution in a lightning stroke near peak temperature. *Journal of Atmospheric Sciences*, 21(3):306–310, 1964.

[12] Dongdong Ni. Empirical models of jupiter's interior from juno data-moment of inertia and tidal love number k2. *Astronomy & Astrophysics*, 613:A32, 2018.

[13] Tobias Chant Owen. Jupiter: The interior. https://www.britannica.com/place/Jupiter-planet/The-interior, 2005. Accessed: 2024-01-15.

[14] David H. Hathaway. The solar interior. https://solarscience.msfc.nasa.gov/interior.shtml, 2022. Accessed: 2024-01-15.

[15] White dwarf. https://en.wikipedia.org/wiki/White_dwarf. Accessed: 2024-01-15.

[16] National Research Council, Plasma Science Committee, et al. *Frontiers in high energy density physics: the X-games of contemporary science*. National Academies Press, 2003.

[17] Frank Graziani, Michael P Desjarlais, Ronald Redmer, and Samuel B Trickey. *Frontiers and challenges in warm dense matter*, volume 96. Springer Science & Business, 2014.

[18] Hye-Sook Park, SJM Ali, PM Celliers, F Coppari, J Eggert, A Krygier, AE Lazicki, JM Mcnaney, M Millot, Y Ping, et al. Techniques for studying materials under extreme states of high energy density compression. *Physics of Plasmas*, 28(6), 2021.

[19] Zhijiang Chen, CB Curry, R Zhang, F Treffert, N Stojanovic, S Toleikis, R Pan, M Gauthier, E Zapolnova, LE Seipp, et al. Ultrafast multi-cycle terahertz measurements of the electrical conductivity in strongly excited solids. *Nature communications*, 12(1):1638, 2021.

[20] Siegfried H. Glenzer and Ronald Redmer. X-ray thomson scattering in high energy density plasmas. *Rev. Mod. Phys.*, 81:1625–1663, Dec 2009.

[21] L. C. Jarrott, B. Bachmann, T. Ma, L. R. Benedetti, F. E. Field, E. P. Hartouni, R. Hatarik, N. Izumi, S. F. Khan, O. L. Landen, S. R. Nagel, R. Nora, A. Pak, J. L. Peterson, M. B. Schneider, P. T. Springer, and P. K. Patel. Thermal temperature measurements of inertial fusion implosions. *Phys. Rev. Lett.*, 121:085001, Aug 2018.

[22] B. Bachmann, J. E. Ralph, A. B. Zylstra, S. A. MacLaren, T. Döppner, D. O. Gericke, G. W. Collins, O. A. Hurricane, T. Ma, J. R. Rygg, H. A. Scott, S. A. Yi, and P. K. Patel. Localized mix-induced radiative cooling in a capsule implosion at the national ignition facility. *Phys. Rev. E*, 101:033205, Mar 2020.

[23] N. V. Smith. Classical generalization of the drude formula for the optical conductivity. *Phys. Rev. B*, 64:155106, Sep 2001.

[24] N. D. Mermin. Lindhard dielectric function in the relaxation-time approximation. *Phys. Rev. B*, 1:2362–2363, Mar 1970.

[25] G. S. Atwal and N. W. Ashcroft. Relaxation of an electron system: Conserving approximation. *Phys. Rev. B*, 65:115109, Feb 2002.

[26] Michael Gittings, Robert Weaver, Michael Clover, Thomas Betlach, Nelson Byrne, Robert Coker, Edward Dendy, Robert Hueckstaedt, Kim New, W Rob Oakes, et al. The rage radiation-hydrodynamic code. *Computational Science and Discovery*, 1(1):015005, 2008.

[27] Brian M Haines, CH Aldrich, JM Campbell, RM Rauenzahn, and CA Wingate. High-resolution modeling of indirectly driven high-convergence layered inertial confinement fusion capsule implosions. *Physics of Plasmas*, 24(5), 2017.

[28] H. Rinderknecht, P. Amendt, S. Wilks, and G. Collins. Kinetic physics in icf: present understanding and future directions. *Plasma Physics and Controlled Fusion*, 60(6):099601, 2018.

[29] Hans G. Rinderknecht, M. J. Rosenberg, C. K. Li, N. M. Hoffman, G. Kagan, A. B. Zylstra, H. Sio, J. A. Frenje, M. Gatu Johnson, F. H. Séguin, R. D. Petrasso, P. Amendt, C. Bellei, S. Wilks, J. Delettrez, V. Yu. Glebov, C. Stoeckl, T. C. Sangster, D. D. Meyerhofer, and A. Nikroo. Ion thermal decoupling and species separation in shock-driven implosions. *Phys. Rev. Lett.*, 114:025001, Jan 2015.

[30] Tirtha Raj Joshi, Peter Hakel, Scott C Hsu, Erik Lehman Vold, Mark J Schmitt, Nelson M Hoffman, Rick M Rauenzahn, Grigory Kagan, X-Z Tang, RC Mancini, et al. Observation and modeling of interspecies ion separation in inertial confinement fusion implosions via imaging x-ray spectroscopy. *Physics of Plasmas*, 24(5), 2017.

[31] B.M. et al. Haines. Observation of persistent species temperature separation in inertial confinement fusion mixtures. *Nature Communications*, 11, 2020.

[32] Jeffrey R Haack, Cory D Hauck, and Michael S Murillo. Interfacial mixing in high-energy-density matter with a multiphysics kinetic model. *Physical Review E*, 96(6):063310, 2017.

[33] MM Marinak, RE Tipton, OL Landen, TJ Murphy, P Amendt, SW Haan, SP Hatchett, CJ Keane, R McEachern, and R Wallace. Three-dimensional simulations of nova high growth factor capsule implosion experiments. *Physics of Plasmas*, 3(5):2070–2076, 1996.

[34] Bruce Fryxell, Kevin Olson, Paul Ricker, FX Timmes, Michael Zingale, DQ Lamb, Peter MacNeice, Robert Rosner, JW Truran, and H Tufo. Flash: An adaptive mesh hydrodynamics code for modeling astrophysical thermonuclear flashes. *The Astrophysical Journal Supplement Series*, 131(1):273, 2000.

[35] Brian Haines. Transport coefficient challenges in high energy density plasmas. *Bulletin of the American Physical Society*, 2022.

[36] Tilak R Dhakal, Brian M Haines, and Richard E Olson. Effects of thermal conductivity of liquid layer in nif wetted foam experiments. *Physics of Plasmas*, 26(9), 2019.

[37] Brian M Haines, DE Keller, KP Long, MD McKay, ZJ Medin, H Park, RM Rauenzahn, HA Scott, KS Anderson, TJB Collins, et al. The development of a high-resolution eulerian radiation-hydrodynamics simulation capability for laser-driven hohlraums. *Physics of Plasmas*, 29(8), 2022.

[38] Jeffrey R. Haack, Cory D. Hauck, and Michael S. Murillo. A conservative, entropic multispecies bgk model. *Journal of Statistical Physics*, 168(4):826–856, Aug 2017.

[39] Grigory Kagan and Xian-Zhu Tang. Electro-diffusion in a plasma with two ion species.

Physics of Plasmas, 19(8), 2012.

[40] LG Stanton, JN Glosli, and MS Murillo. Multiscale molecular dynamics model for heterogeneous charged systems. *Physical Review X*, 8(2):021044, 2018.

[41] AB Zylstra, Nelson M Hoffman, Hans W Herrmann, MJ Schmitt, YH Kim, K Meaney, A Leatherland, S Gales, C Forrest, V Yu Glebov, et al. Diffusion-dominated mixing in moderate convergence implosions. *Physical Review E*, 97(6):061201, 2018.

[42] Hans G. Rinderknecht, H.-S. Park, J. S. Ross, P. A. Amendt, D. P. Higginson, S. C. Wilks, D. Haberberger, J. Katz, D. H. Froula, N. M. Hoffman, G. Kagan, B. D. Keenan, and E. L. Vold. Highly resolved measurements of a developing strong collisional plasma shock. *Phys. Rev. Lett.*, 120:095001, Mar 2018.

[43] Brian M Haines, TJ Murphy, RE Olson, Y Kim, BJ Albright, B Appelbe, TH Day, MA Gunderson, CE Hamilton, T Morrow, et al. The dynamics, mixing, and thermonuclear burn of compressed foams with varied gas fills. *Physics of Plasmas*, 30(7), 2023.

[44] Brett Keenan. Verification study of xrage's multi-ion viscosity model. Technical report, Los Alamos National Lab.(LANL), Los Alamos, NM (United States), 2022.

[45] Nelson M Hoffman, George B Zimmerman, Kim Molvig, Hans G Rinderknecht, Michael J Rosenberg, BJ Albright, Andrei N Simakov, Hong Sio, Alex B Zylstra, Maria Gatu Johnson, et al. Approximate models for the ion-kinetic regime in inertial-confinement-fusion capsule implosions. *Physics of Plasmas*, 22(5), 2015.

CHAPTER 2

MULTI-SCALE NATURE OF PLASMA

The dynamics of plasmas are inherently multi-scale. Many-body physics provides a framework to describe the dynamics at each scale. In this chapter, we begin by discussing classical molecular dynamics (MD) which describes the system in terms of deterministic dynamics of individual particles. This approach is entirely based on evolving Hamilton's equations of motion. Then we discuss kinetic theory, a statistical framework that describes the system in terms of distributions of particle velocities and positions. This approach is encapsulated in evolving the Boltzmann integro-differential equation or the Bhatnagar-Gross-Krook (BGK) partial differential equation. Finally, we discuss fluid dynamics, which coarse-grains away the details of individual particles and describes the system with position dependent density, velocity, and temperature fields. This approach is exemplified by the Navier-Stokes equations. Together, these frameworks provide insight into plasma: molecular dynamics describes the microscopic scale, kinetic theory describes the mesoscopic scale, and fluid dynamics describes the macroscopic scale.

Each of these theories has unknowns which must be supplied to close the governing equations; these unknowns are referred to as closure information. For fluid dynamics, the plasma's pressure tensor P, heat flux $\vec{q}$, and dielectric function $\varepsilon(k, \omega)$ are closures that can be provided by kinetic theories. However, kinetic theories themselves require closures. Two examples of kinetic closures are the collision cross sections σ needed to evolve the Boltzmann equation and the effective relaxation/collision rate ν needed to evolve the BGK kinetic equation. These closures can be provided by molecular dynamics simulations which track individual particles. However, the closure problem also affects molecular dynamics, where effective inter-atomic potentials (informed by quantum mechanics) are needed to evolve Hamilton's equations. It's turtles all the way down! At every stage a finer scale theory is needed to inform the necessary closure information. Table 2.1 organizes the hierarchy of closure information described in this paragraph.

The hierarchical structure of closures is no accident. In the early 1900s Hilbert posed 23 problems, his sixth problem called for a rigorous derivation showing how macroscopic degrees of free-

Table 2.1 Tabulation of theories from fine to coarse degrees of freedom. Each theory's relevant dynamical equations and closure information are identified.

Theory	Example Equation	Closure Information
Molecular Dynamics	Hamilton's Equations	Interaction Potential ϕ
Kinetic Theory	Boltzmann's Equation	Collision cross section σ
Kinetic Theory	BGK's Equation	Collision rate τ
Hydrodynamics	Navier-Stokes' Equations	P, $\vec{q}$, and ϵ

dom (*e.g.* density, momentum, and energy fields in a fluid) emerge from microscopic degrees of freedom (*e.g.*, Hamilton's equations). The problem proved influential, works are still being published in an endless pursuit of rigor [1].

Typical answers to Hilbert's sixth problem have the following form. Microscopic degrees of freedom (DoF) are integrated over, leaving behind only macroscopic DoF. However, the coupling between macro and micro DoF typically produces a hierarchy of equations, preventing the integration from producing a closed system. The "truncation" assumption cuts off the hierarchy producing a closed system of equations. These assumptions typically hinge on the time scale separation between the coarse and fine grain theories (n-body, kinetic, and hydrodynamic descriptions). Here the hydrodynamic description corresponds to the longest time scale [2, 3]. A diagram organizing the answer to Hilbert's sixth problem according to integration and truncation steps is provided in Figure 2.1.

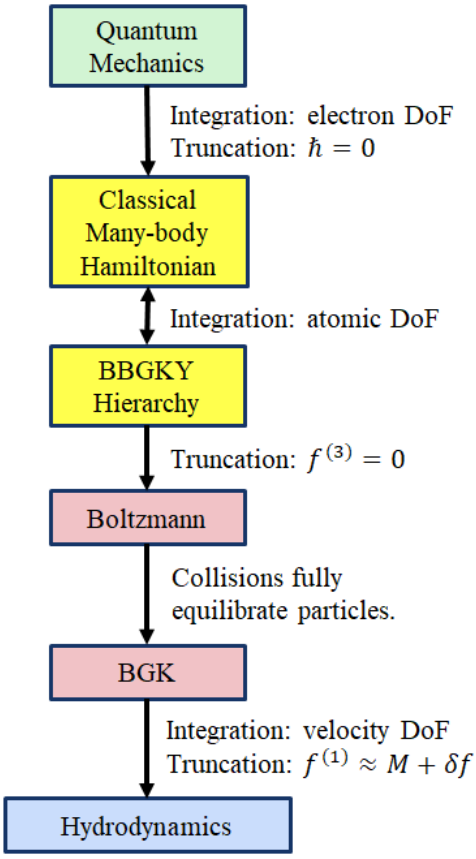

Figure 2.1 The relations between quantum, micro-, meso-, and macroscopic formalisms.

An equivalent framing of Hilbert's sixth problem uses invariant manifolds. This framework is typically used to interpret extended moment hydrodynamics mod-

els [1]. An invariant manifold is a subset of the system's phase space characterized as being invariant under the system's dynamical equations. This implies that if the system's state is on the invariant manifold at one point in time, it will remain on the manifold at all future times. The slow manifold is a subset of the invariant manifold, containing only the longest lasting modes, it forms a low-dimensional model of the system's long time behavior [4]. Muncaster frames the process of constructing coarse grained theories from fine theories as a process of constructing the slow invariant manifold of the fine grained theory [5]. This is extended by Gorban and Karlin who formulate hydrodynamics as the problem of discovering invariant manifolds in the space of distribution functions [6]. For more details, Gorban and Karlin give a thorough introduction to this framing of Hilbert's sixth problem [7].

Every major result of this thesis constitutes closure information; this chapter shows the reader a small sample of where and how closure information arises. In this chapter, we go over the essential steps laid out in Figure 2.1. First, we identify how classical molecular dynamics emerges from Schrödinger's equation. Then we distill kinetic theory from classical molecular dynamics. Finally, we derive fluid dynamics as a limiting case of kinetic theory. The many body formalism developed in each section will be applied to more substantive problems in later chapters.

2.1 Classical Molecular Dynamics

Molecular dynamics (MD) delves into the detailed interactions and trajectories of individual particles. At this level, the role of quantum mechanics becomes apparent, as it treats individual particles as probability waves. The Schrödinger equation, which describes the wave state evolution, is the typical description. The multi-scale nature of molecular dynamics is exemplified by Born-Oppenheimer MD, which uses quantum mechanics to calculate the forces on classical nuclei. In this section, we integrate out the quantum electronic DoF and truncate the system of equations to arrive at classical MD [8, Chapter 10].

Consider the partition function $\mathcal{Z}$ of a system of ions and electrons

$$\mathcal{Z} = \mathcal{N}\mathrm{Tr}\left\{e^{-\beta(H_I+H_e+U_{Ie})}\right\} \tag{2.1}$$

Here $\mathcal{N}$ is a normalization constant, H_I is the ion Hamiltonian, H_e is the electron Hamiltonian, and U_{Ie} is the ion-electron interaction energy. "For brevity, we neglect the one-body potential U_{ext} arising from the external field, but will introduce it into the final expression Eq(2.14). H_I commutes with H_e and if we assume that the ions are classical, then H_I also commutes with U_{Ie}. By the Baker-Campbell-Hausdorff identity, this produces

$$\mathcal{Z} = \mathcal{N} \int \prod_{i=s}^{N} dr_i dp_i e^{-\beta H_I} \text{Tr}\left\{e^{-\beta(H_e+U_{Ie})}\right\} \tag{2.2}$$

Integrating over electronic DoF alters the classical exponent, producing

$$\mathcal{Z} = \mathcal{N} \prod_{i=s}^{N} dr_i dp_i e^{-\beta(H_I+F_{Ie})}. \tag{2.3}$$

Here we have inserted the free energy $F_{Ie} \equiv -T \ln Z_{Ie}$, where $Z_{Ie} = \text{Tr}\left\{e^{-\beta(H_e+U_{Ie})}\right\}$. From Eq(2.3), we identify the effective Hamiltonian governing the ion equations of motion

$$H_I^{\text{eff}} = H_I + F_{Ie}. \tag{2.4}$$

Notice the coupling U_{Ie} between ion and electron DoF persists within F_{Ie}, so for this effective Hamiltonian the ion equations of motions would be coupled to the electron equations of motion.

Let us examine the functional form of H_I^{eff}. Assuming a standard coulomb interaction, the Fourier representation of the ion Hamiltonian is [8, chapter 10]

$$H_I = \sum_i \frac{p_i^2}{2m_i} + \frac{1}{2L^3} \sum_k v_{II}(k)\Big(n_I(k)n_I(-k) - N_I\Big). \tag{2.5}$$

where $v_{II}(k) = 4\pi Z_I^2 e^2/k^2$. Next, formulate F_{Ie} in terms of tractable quantities. We proceed by treating the ion-electron interaction as weak and associating a coupling constant λ with the interaction. In this approximation, the effective free energy is [9]

$$F_{Ie} = F_e + \int_0^1 d\lambda \, \langle U_{Ie} \rangle_\lambda \tag{2.6}$$

where $\langle \cdot \rangle_\lambda$ indicates an ensemble average with weight $\exp[-\beta(H_e + \lambda H_{Ie})]$. Assuming periodic boundary conditions of length L, then the Hartree interaction, in momentum space, is given as

$$U_{Ie}(k, \lambda) = \frac{1}{L^3} \sum_{k \neq 0} v_{Ie}(k) n_I(k) n_e(k), \tag{2.7}$$

up to some constant U_0. The simplest assumption is the Coulomb approximation $v_{Ie}(k) = 4\pi Z_i e^2/k^2$. In some cases, a hard-core ion-electron interaction model is used [10]. At $\lambda = 0$, the electron density is unaltered by the presence of ions $\langle n_I(k) n_e(-k)\rangle_{\lambda=0} = 0$. However, at the next order the electron positions are altered by the presence of ions. We write the Eq(2.6) as

$$F_{Ie} = F_e + \frac{1}{L^3}\sum_{k\neq 0} v_{Ie}(k) n_I(k) \int_0^1 d\lambda \, \langle \delta n_e(k)\rangle_\lambda. \tag{2.8}$$

Here $\langle \delta n_e(k)\rangle_\lambda$ captures the magnitude by which the ions alter the electron from its uniform distribution.

Next we need to evaluate the integral in Eq(2.8). Assuming that the density perturbations of electrons are time-independent and can be described by linear response theory,

$$\delta n_e(k) = C_{e,0}(k)\left(v_{ee}(k)\delta n_e(k) + \lambda v_{Ie}(k) n_I(k)\right) \tag{2.9}$$

where $C_{e,0}(k)$, sometimes denoted χ, is the static susceptibility of the ideal electron gas. Rearranging this equation yields

$$\delta n_e(k) = \lambda \left(\frac{C_{e,0}(k)}{1 - v_{ee}(k) C_{e,0}(k)}\right) v_{Ie}(k) n_I(k). \tag{2.10}$$

Inserting Eq(2.10) into Eq(2.8) yields our final result

$$F_{Ie} = F_e + \frac{1}{2L^3}\sum_k C_e(k) |v_{Ie}(k)|^2 n_I(k) n_I(-k), \tag{2.11}$$

where

$$C_e(k) \equiv \frac{C_{e,0}(k)}{1 - v_{ee}(k) C_{e,0}(k)}. \tag{2.12}$$

We have now formulated F_{Ie} in terms of ion density and electron susceptibility, cleanly separating the electron and ion DoFs.

Our ultimate goal, deriving classical equations of motion for the ions, is within reach. Inserting Eq(2.5) and Eq(2.11) into Eq(2.4) yields

$$H_I^{\text{eff}} = \sum_i \frac{p_i^2}{2m_i} + \frac{1}{2L^3}\sum_k \left(v_{II}(k) + C_e(k)|v_{Ie}(k)|^2\right)\left(n_I(k) n_I(-k) - N_I\right) + F_e', \tag{2.13}$$

where $F_e' = F_e + \frac{N_I}{2L^3}\sum_k C_e(k)|v_{Ie}(k)|^2$. In Eq(2.13), the electron and ion DoF are separated and the associated Hamilton's equations are,

$$\dot{r}_i = p_i/m, \tag{2.14a}$$

$$\dot{p}_i = -\nabla_{r_i}\left(U^{\text{ext}}(r_i) + \frac{1}{2}\sum_{i\neq j} U_{II}^{\text{eff}}(|r_i - r_j|)\right). \tag{2.14b}$$

In these equations, $\{r_i, p_i\}$ represents the phase space position of the i^{th} ion. The effective 2 body interaction potential is defined

$$U_{II}^{\text{eff}}(r) \equiv \frac{1}{2L^3}\int d^3k\, e^{ikr}\left(v_{II}(k) + C_e(k)|v_{Ie}(k)|^2\right)\Big(n_I(k)n_I(-k) - N_I\Big). \tag{2.15}$$

Thus, at linear order, an effective two-body interaction is the only required closure needed for classical molecular dynamics. Beyond linear response 3 through N body forces emerge [10].[1] This concludes our derivation of MD closure information using linear response theory. Eq(2.14) forms the foundation of kinetic models and Eq(2.15) demonstrate one of many uses for the susceptibility (which will be computed in Chapter 3).

2.2 Kinetic Theory

Kinetic theory, sometimes called non-equilibrium statistical mechanics, serves as a bridge connecting the motion and interactions of individual particles to observable properties of matter, such as density, bulk velocity, temperature, and pressure. The multi-scale nature of kinetic theory is exemplified by the classical Liouville equation, which describes the temporal evolution of the N particle system. The equation is instrumental in linking the detailed, microscopic behavior of particles with the emergent, macroscopic properties of the system because it describes the evolution in terms of a probability distribution function.

Consider a system of N charged particles, whose motion is described by the classical MD equations previously derived in Eq(2.14). The Hamiltonian is

$$H = \sum_{i=1}^{N} H_i^{(1)} + \frac{1}{2}\sum_{i\neq j} V_{II}^{\text{eff}}(|r_i - r_j|) \tag{2.16}$$

[1] In the high temperature limit, Eq(2.15) easily produces the earlier derived Yukawa interaction potential. Other closures have been computed using Eq(2.15) [11, 12, 10].

where $H^{(1)}$ is the one-body Hamiltonian

$$H_i^{(1)} \equiv \frac{p_i^2}{2m_i} + U_{\text{ext}}(r_i) \tag{2.17}$$

The mean field (MF) approximation is used to incorporate the collective behavior of our plasma system through $U_{\text{ext}}(r_i)$. In the mean field approximation, the electric potential $\Phi(r)$ produced by the system of charged particles is taken as an external field for any given particle.. In the electro-static approximation, the Poisson equation defines the electric potential as

$$\frac{k^2}{4\pi}\Phi(k) = \sum_\alpha q_\alpha n_\alpha(k)\epsilon_\alpha^{-1}(k). \tag{2.18}$$

Here α and β indexes the ion species and $\epsilon_\alpha^{-1}(k)$ is the position-dependent dielectric function defined in terms of the static susceptibility $C_{\alpha,\beta}(k)$,

$$\epsilon_\alpha^{-1}(k) \equiv 1 + \sum_\beta v_{\alpha\beta}^{\text{eff}}(k)C_\beta(k). \tag{2.19}$$

A given particle couples to this potential by its charge. If we include time dependence, then further Maxwell equations are needed.

Now let us proceed to the objective, reformulate the evolution of N particles as an evolution of a N body probability distribution. First, define the function $f^{(N)}(\{r_i\}, \{p_i\}, t)$, with $i = 1, \ldots, N$, which is the local density of particles in N body phase space. Since $f^{(N)}$ is a probability distribution it is normalized such that

$$1 = \int \left(\prod_i dr_i dp_i\right) f^{(N)}(\{r_i\}, \{p_i\}, t). \tag{2.20}$$

Given that probability is locally conserved, $f^{(N)}$ must satisfy the continuity equation,

$$\partial_t f^{(N)} + \nabla_{r,p} \cdot \mathbf{u}_{r,p} f^{(N)} = 0, \tag{2.21}$$

The phase space velocity is $\mathbf{u}_{r,p} = (\dot{r}_1, \ldots, \dot{r}_N, \dot{p}_1, \ldots, \dot{p}_N)$. Next, we simplify this equation using the product rule and Hamilton's equations Eq(2.14) to arrive at the material derivative formulation of the continuity equation

$$\partial_t f^{(N)} + \mathbf{u}_{r,p} \cdot \nabla_{r,p} f^{(N)} = 0. \tag{2.22}$$

Finally, we recognize $\mathbf{u}_{r,p} \cdot \nabla_{r,p}$ as the Poisson bracket and we arrive at the classical Liouville equation

$$\partial_t f^{(N)} + \{f^{(N)}, H\} = 0. \tag{2.23}$$

The characteristic curves of the Liouville equation Eq(2.23) are defined by Eq(2.16)'s associated Hamilton equations [3]. Thus, the Liouville equation is the crucial step between the particle description and the statistical description. From here on we can describe our system with probabilistic approaches.

We will now determine the dynamics of the 1 body distribution. The s body marginal distribution is defined by integrating the N body distribution over the phase space coordinates of $N - s$ particles

$$f^{(s)}(R_1, p_1, t) = \frac{N!}{(N-s)!} \int \left(\prod_{i=s}^{N} dr_i dp_i \right) f^{(N)}(r_i, p_i, t). \tag{2.24}$$

The dynamics of the one-body distribution, denoted f instead of $f^{(1)}$ for brevity, can be computed explicitly from Eq(2.23) by integrating over the coordinates of $N - 1$ particles. The result is [13, Chapter 2]

$$\partial_t f(r_1, p_1, t) = \left\{ f(r_1, p_1, t), H^{(1)} \right\} + Q \tag{2.25}$$

where Q, sometimes denoted as $\left.\frac{\delta f}{\delta t}\right|_c$, is the collision operator

$$Q \equiv \int dr_2 dp_2 \nabla_{r_1} V_{II}^{\text{eff}}(r_1 - r_2) \cdot \nabla_{p_1} f^{(2)}(r_1, r_2, p_1, p_2, t). \tag{2.26}$$

Eq(2.25) is the first equation in the BBGKY hierarchy. We see the evolution of the 1 body evolution depends on the evolution of the 2 body distribution. This persists in higher n body dynamics which depend on $n + 1$ body dynamics. Thus, even though Eq(2.25) is formally exact, it is not a closed equation. The unknown quantity Q arises from the interactions between DoFs which were integrated and DoFs that were not integrated. We will spend the remainder of the section reformulating Q to close the equation.

Many approaches have been developed to express the collision operator Q solely in terms of f [14], and new operators geared towards plasmas continue to be proposed [15]. However, in keeping

with Figure 2.1, we aim to compute the Boltzmann equation. To do so we would integrate Eq(2.23) to determine the dynamics of $f^{(2)}$, assume the three-body collision operator is zero (*i.e.*, $f^{(3)} = 0$) and reduce the two equations.However, this process is laborious and not relevant to subsequent chapters. Interested readers are referred to Tong's kinetic theory notes [13, Chapter 2] or Liboff's introductory textbook [3, Chapter 3].

Instead, we show how to derive the BGK collision operator from the Boltzmann collision operator. The well-known Boltzmann collision operator is given

$$Q = \int d\Omega\, d^3p_2\, g\sigma\ \left(f(r, p_1', t) f(r, p_2', t) - f(r, p_1, t) f(r, p_2, t)\right). \tag{2.27}$$

Here p_1 is the momentum of particle 1 pre-collision, p_1' is the momentum of particle 1 post-collision, $g = |\mathbf{p}_1 - \mathbf{p}_2|$ is the relative pre-collision momentum, and $\sigma(g, \Omega)$ is the differential cross section. Suppose that the velocity distribution is in equilibrium after collisions, then we represent the post-collision distribution function as a Maxwellian M,

$$Q = \int d\Omega\, d^3p_2\, g\sigma\ \left(M(r, p_1, t) M(r, p_2, t) - f(r, p_1, t) f(r, p_2, t)\right). \tag{2.28}$$

Suppose $f(r, p_2, t)$ is represented well by a Maxwellian. This approximation is not motivated by a near-equilibrium assumption. Rather, $M(r, p_2, t)$ is defined such that its $1, v, v^2$ moments produce the moments of $f(r, p_2, t)$. The final result is the BGK collision operator

$$Q = \frac{1}{\tau}\left(M(r, p, t) - f(r, p, t)\right). \tag{2.29}$$

where we have relabeled $p_1 \to p$ and the collision frequency is defined

$$\frac{1}{\tau} = \nu \equiv \int d\Omega\, d^3p_2\, g\sigma\, f(r, p_2, t). \tag{2.30}$$

Dimensionally, τ represents a rate, and from Eq(2.25) we can see that this is the rate at which the one-body distribution relaxs towards a Maxwellian.

We have detailed the closures Eq(2.30) and Eq(2.19) needed to evolve the BGK kinetic equation Eq(2.25). Insert Eq(2.18) and Eq(2.26) into Eq(2.25) and expand out the Poisson Bracket to arrive at an expression for the BGK kinetic equation

$$\partial_t f + \mathbf{v} \cdot \nabla_{\mathbf{x}} f + \mathbf{F} \cdot \nabla_{\mathbf{p}} f = \frac{1}{\tau}\left(M(r, p, t) - f(r, p, t)\right). \tag{2.31}$$

The force is defined as $m\mathbf{a} = -\nabla U_{\text{ext}} = Z_I e \epsilon(r)\mathbf{E}(r)$. This concludes our derivation of kinetic equations from N-body MD. We have completed the step from microscopic DoF to intermediate mesoscopic DoF. We see that the effective ion-ion interaction, the dielectric function ϵ (related to susceptibility via Eq(2.19)), and the collision rate ν are necessary closures for the BGK kinetic equation.

2.3 Hydrodynamics

As the coarsest theory, fluid dynamics formulates the system entirely in terms of observable thermodynamic quantities, it describes the bulk motion of momentum, mass, and energy in a fluid. Each equation (momentum, mass, and energy) corresponds to the dynamics of a moment of the one-body distribution function derived in the previous section. In effect, Navier-Stokes' equations only track the evolution of the lowest moments (*i.e.* $1, \mathbf{v}, v^2$). Certain models, known as extended moment hydrodynamics, track the evolution of more than 3 moments. For example, one approach preserves 6000+ moments [16].

In this section, we derive fluid dynamics from the BGK kinetic equation. We will begin by macroscopic averaging, *i.e.*, taking M moments of the 1 body kinetic equation. A hierarchy of moments will emerge, where the M-th moment depends on the $M + 1$ moment. To form a closed system, the $M + 1$ moment must be expressed in terms of the previous M moments. Many approaches to close this hierarchy have emerged, typically truncating it by expanding about equilibrium. Including deviations from equilibrium in the expansion manifests non-local transport phenomena, *e.g.*, viscosity.

We conduct macroscopic averaging on our kinetic equation to arrive at fluid transport equations. Consider the BGK equation Eq(2.31) derived in the previous section. The BGK collision operator Eq(2.29) satisfies local mass, momentum, and energy conservation [17]

$$\int d^3v \begin{bmatrix} 1 \\ \mathbf{v} \\ v^2 \end{bmatrix} Q = \begin{bmatrix} 0 \\ 0 \\ 0 \end{bmatrix}. \tag{2.32}$$

Now, take the moment with respect to one of these collisional invariants, denoted by $A(v)$,

$$\int d^3v A(v) \left(\partial_t f + \mathbf{v} \cdot \nabla_{\mathbf{x}} f + \mathbf{a} \cdot \nabla_{\mathbf{v}} f\right) = 0. \tag{2.33}$$

This equation can be simplified with calculus identities to

$$\partial_t n\langle A\rangle + \nabla_{\mathbf{x}} \cdot n\langle vA\rangle - n\langle \nabla_{\mathbf{x}} Av\rangle - n\langle \mathbf{a} \cdot \nabla_{\mathbf{v}} A\rangle = 0. \tag{2.34}$$

where

$$n(x,t) \equiv \int d^3v f, \tag{2.35}$$

From Eq(2.34) we can generate equations for mass, momentum, and energy transport, $A = m, m\mathbf{v}, \frac{m}{2}(v-u)^2$ respectively. These transport equations, in their conservative form, are

$$\partial_t \rho = -\nabla_{\mathbf{x}} \cdot (\rho \mathbf{u}), \tag{2.36a}$$

$$\partial_t \rho \mathbf{u} = -\nabla_{\mathbf{x}} \cdot \left(P + \rho \mathbf{u} \otimes \mathbf{u} - \rho \mathbf{a}\right), \tag{2.36b}$$

$$\partial_t \frac{3p}{2} = -\nabla_{\mathbf{x}} \cdot (\mathbf{q} + p\mathbf{u}) + \nabla_{\mathbf{x}} \mathbf{u} : \mathrm{P}. \tag{2.36c}$$

where

$$\tag{2.37a}$$

$$\rho(x,t) \equiv m \int d^3v f, \tag{2.37b}$$

$$\mathbf{u}(x,t) \equiv \int d^3v\, \mathbf{v} f, \tag{2.37c}$$

$$P(x,t) \equiv \int d^3v\, (\mathbf{v} - \mathbf{u})(\mathbf{v} - \mathbf{u}) f, \tag{2.37d}$$

$$p(x,t) \equiv \frac{1}{3}\mathrm{Tr}\{P\} = \frac{1}{3}\int d^3v\, (v-u)^2 f, \tag{2.37e}$$

$$\mathbf{q}(x,t) \equiv \int d^3v\, (\mathbf{v} - \mathbf{u})(v-u)^2 f. \tag{2.37f}$$

While exact, these equations do not form a closed set. The four variables $\rho, \mathbf{u}, P, \mathbf{q}$ are the 0^{th}, 1^{st}, 2^{nd}, 3^{rd} moments respectively. However, there are only three equations; the q is connecting the higher moments to the lower moments.

Based on Eq(2.36), the heat flux $\mathbf{q}$ and the off-diagonal components of the pressure tensor P constitute the closure information needed for these three macroscopic equations. There are many known approaches to derive $\mathbf{q}$ and P [18]. In fact, new methods are still being suggested [19, 20]! We will follow the Chapman-Enskog expansion procedure to inform q and P.

Based on the definitions of P and $\mathbf{q}$ from Eq(2.37), fixing $f(x, v, t)$ determines the closure. To determine $f(x, v, t)$, expand the BGK kinetic equation Eq(2.31) about local Maxwellian as $f(x, v, t) \approx M(x, v, t) + \delta f(x, v, t)$. At first order, the equation yields

$$\partial_t M + \mathbf{v} \cdot \nabla_{\mathbf{x}} M + \mathbf{a} \cdot \nabla_{\mathbf{v}} M = \epsilon \nu \delta f. \tag{2.38}$$

We can solve this equation for δf and then insert $f = M + \delta f$ into Eq(2.37d) to compute the pressure

$$\mathrm{P} = nT \left(I - \frac{1}{\nu} (\nabla_{\mathbf{x}} \mathbf{u} + (\nabla_{\mathbf{x}} \mathbf{u})^T) \right) \tag{2.39}$$

and Eq(2.37f) to compute the heat flux

$$\mathbf{q} = -\frac{5}{2} \frac{nT}{m\nu} \nabla_{\mathbf{x}} T. \tag{2.40}$$

The external force $m\mathbf{a}$ has dropped out, but collision frequency ν has been carried into the hydrodynamic closures. In the equilibrium case (*i.e.*, $f(x, v, t) \approx M(x, v, t)$), Eq(2.39) reduces to $\mathrm{P} = nT\mathrm{I}$ where I is the identity matrix and $\mathbf{q} = \mathbf{0}$ [2].

We have completed our task, Eq(2.39) and Eq(2.40) provide closure for Eq(2.36). This concludes the final step from mesoscopic DoF to macroscopic DoF. We have truncated the hydrodynamic hierarchy by expressing the two-body distribution function f in terms of the lowest moments n, $\mathbf{u}$, and p and showed what constitutes closure information for hydrodynamic equations.

2.4 Time and length scales associated to the various frameworks

In applications ranging from controlled nuclear fusion to stellar evolution, physicists wish to predict how plasmas will evolve. Accurately modeling the dynamics of a large number of interacting particles in three dimensions via Born-Oppenheimer MD requires immense computational

[2] We note that using high order expansions $f = M + \epsilon \delta f + \epsilon^2 \delta f'$ yields higher order gradients, *i.e.*, ∇^3 [21]. In effect fluid dynamics is "rectangular", in the sense that the equation's "width" is determined by the highest order spatial derivative and the height is determined by the number of moments you evolve.

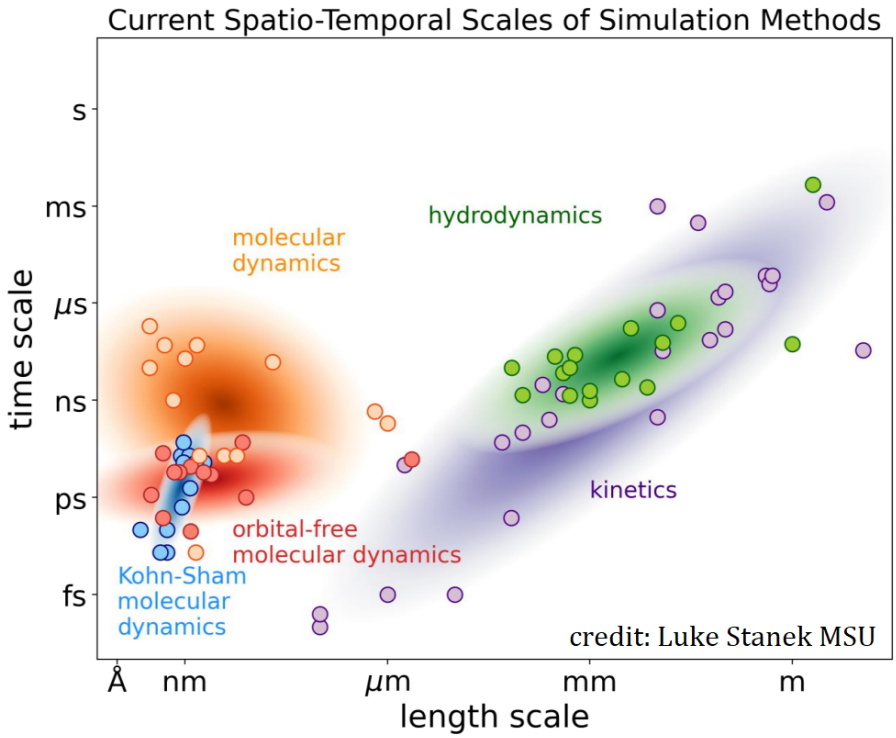

Figure 2.2 Plot indicating the total time elapsed and total spatial extent of various published simulations. Compared to molecular dynamics calculation which compute the inter atomic forces with quantum methods (*i.e.*, orbital-free and Kohn-Sham) the classical molecular dynamics simulations can reach larger and longer time scales. There is strong overlap between hydrodynamics and kinetics simulations, but generally these methods simulate larger and longer time scales. Plot reprinted from Luke Stanek's PhD dissertation with author permission.

resources, often beyond the capacity of modern clusters. Thus all three frameworks presented in this chapter, molecular dynamics, kinetic equations, and fluid dynamics, are used in practice. Due to the current state of computation resources each framework has a limited domain of temporal and spatial extents in physical three-dimensional systems. A sampling of real word simulations illustrates the time and length scales of actual simulations.

BIBLIOGRAPHY

[1] Alexander N Gorban. Hilbert's sixth problem: the endless road to rigour, 2018.

[2] Richard L Liboff. Generalized bogoliubov hypothesis for dense fluids. *Physical Review A*, 31(3):1883, 1985.

[3] Richard L Liboff. *Kinetic theory: classical, quantum, and relativistic descriptions*. Springer Science & Business Media, 2003.

[4] A. J. Roberts. The utility of an invariant manifold description of the evolution of a dynamical system. *SIAM Journal on Mathematical Analysis*, 20(6):1447–1458, 1989.

[5] RG Muncaster. Invariant manifolds in mechanics i: The general construction of coarse theories from fine theories. *Archive for Rational Mechanics and Analysis*, 84(4):353–373, 1983.

[6] Alexander Gorban and Ilya Karlin. Hilbert's 6th problem: exact and approximate hydrodynamic manifolds for kinetic equations. *Bulletin of the American Mathematical Society*, 51(2):187–246, 2014.

[7] Aleksandr Nikolaevich Gorban and Ilya V Karlin. *Invariant manifolds for physical and chemical kinetics*, volume 660. Springer, 2005.

[8] Jean-Pierre Hansen and Ian Ranald McDonald. *Theory of simple liquids: with applications to soft matter*. Academic press, 2013.

[9] Francois Englert and R Brout. Dielectric formulation of quantum statistics of interacting particles. *Physical Review*, 120(4):1085, 1960.

[10] JA Porter, NW Ashcroft, and GV Chester. Pair potentials for simple metallic systems: Beyond linear response. *Physical Review B*, 81(22):224113, 2010.

[11] DG Pettifor and MA Ward. An analytic pair potential for simple metals. *Solid state communications*, 49(3):291–294, 1984.

[12] Tobias Dornheim, Panagiotis Tolias, Zhandos A Moldabekov, Attila Cangi, and Jan Vorberger. Effective electronic forces and potentials from ab initio path integral monte carlo simulations. *The Journal of Chemical Physics*, 156(24), 2022.

[13] David Tong. Kinetic theory. `https://www.damtp.cam.ac.uk/user/tong/kintheory/`, 2012. Accessed: 2024-01-24.

[14] Setsuo Ichimaru. *Statistical Plasma Physics, Vol1: Basic Principles*. CRC Press, 1991.

[15] Scott D Baalrud and Jérôme Daligault. Mean force kinetic theory: A convergent kinetic

theory for weakly and strongly coupled plasmas. *Physics of Plasmas*, 26(8), 2019.

[16] Jeong-Young Ji, Gunsu S Yun, Yong-Su Na, and Eric D Held. Electron parallel transport for arbitrary collisionality. *Physics of Plasmas*, 24(11), 2017.

[17] P. L. Bhatnagar, E. P. Gross, and K. Krook. Uniformly stable numerical schemes for the Boltzmann equation preserving the compressible Navier-Stokes asymptotics. *Phys. Rev.*, 94:511–524, 1954.

[18] Sydney Chapman and Thomas George Cowling. *The mathematical theory of non-uniform gases: an account of the kinetic theory of viscosity, thermal conduction and diffusion in gases*. Cambridge university press, 1990.

[19] Zhenning Cai, Yuwei Fan, and Ruo Li. Globally hyperbolic regularization of grad's moment system. *Communications on pure and applied mathematics*, 67(3):464–518, 2014.

[20] Ilya Karlin. Derivation of regularized grad's moment system from kinetic equations: modes, ghosts and non-markov fluxes. *Philosophical Transactions of the Royal Society A: Mathematical, Physical and Engineering Sciences*, 376(2118):20170230, 2018.

[21] Amit Agrawal, Hari Mohan Kushwaha, Ravi Sudam Jadhav, Amit Agrawal, Hari Mohan Kushwaha, and Ravi Sudam Jadhav. Burnett equations: derivation and analysis. *Microscale Flow and Heat Transfer: Mathematical Modelling and Flow Physics*, pages 125–188, 2020.

CHAPTER 3

CONSERVATIVE DIELECTRIC RESPONSE AND ELECTRICAL CONDUCTIVITY FROM MULTI-SPECIES BHATNAGAR-GROSS-KROOK

3.1 Introduction

Many scientific investigations require dynamic response models such as the dynamic structure factor (DSF), dielectric function, and conductivity, though only a small subset are mentioned here. One source of demand is X-ray Thomson scattering (XRTS) diagnostics, which use a DSF model to infer the plasma's properties, i.e., number density, temperature, and ionization [1, 2]. Another source of demand arises in optical conductivity experiments, which use a conductivity model to extrapolate the material's DC conductivity from optical regime measurements [3]. Similarly, for density functional theory (DFT) calculations to estimate the electrical conductivity, a conductivity model is needed to extrapolate the material's DC conductivity from Kubo-Greenwood estimates [4]. The final source of demand we list is radiation hydrodynamics (rad-hydro) simulations, which use dielectric functions to estimate the plasma's stopping power (*e.g.*, SRIM [5]) and DSFs to compute Bremsstrahlung emissions rates [6]. This chapter provides a conservative model of the dielectric function, dynamic structure factor (DSF), and conductivity.

These demands are met by many different models. We call one grouping of models "semi-empirical", which have free parameters tuned to match data. Semi-empirical models can lack clear interpretations. The lack of clear interpretations is exemplified by non-Drude conductivity models, which are used by both high energy density (HED) and nanomaterials scientists to extrapolate the DC conductivity from THz conductivity measurements [7, 8, 9]. When non-Drude behavior is observed, the primary alternative is the Drude-Smith conductivity model [10]. But Smith's model has a phenomenological parameter of unknown meaning [11, 12]. Smith asserts that his modification to the Drude model accounts for charge carrier backscattering [13], while Cocker et al. challenge this claim, having derived a similar modification under the assumption of localized charge carriers [14]. Thus, interpretable semi-empirical models are needed.

We call the alternative to semi-empirical models "first-principles" models. These models have

calculated inputs rather than tuned parameters and, as a result, have clearer interpretations. We will consider, Mermin's collision corrected dielectric function [15], which requires a calculated dynamical collision frequency. To improve the Mermin model's predictions, research has improved the collision frequencies estimates [16, 17, 18, 19]. Yet, regardless of collision frequency choice, the Mermin model predicts nonphysical behavior. Atwal and Ashcroft showed that Mermin's dielectric function does not have an infinitesimal plasmon width and thus does not satisfy the frequency sum rule [20]. Further, they show that a dielectric function which includes momentum and energy conservation has an infitesimal plasmon width and thus does satisfy the frequency sum rule. Morawetz and Fuhrmann established that Mermin's dielectric function has the wrong scaling in the high frequency limit, but the inclusion of momentum conservation corrects this scaling [21]. However, both works also demonstrate that if a *single species* dielectric function conserves momentum then it also predicts an infinite conductivity. This implies that only multi-species dielectric functions can conserve momentum without predicting infinite conductivity. Thus, a momentum conserving multi-species first-principles model is well motivated.

In this chapter, we derive our momentum conserving multi-species susceptibility from a kinetic equation in the relaxation-time approximation. In this approach, the distribution function exponentially decays toward a target function, which is characterized by local perturbations in the chemical potential, velocity, and temperature. These perturbations are constrained to enforce number, momentum, and energy conservation and substituted into the linearized kinetic equation to produce dynamical response functions. In this way, Selchow and Morawetz [22] derive the Mermin's single species dielectric function from both the classical Bhatnagar, Gross, and Krook (BGK) kinetic equation [23] and the classical Fokker-Plank kinetic equation [24, 25]. Additionally, Atwal and Ashcroft derive a number, momentum, and energy conserving single-species dielectric function from the BGK kinetic equation [20]. Currently, a multi-species Mermin dielectric function exists [26], but it has not been extended to include momentum conservation. We produce the first number and momentum conserving multi-species susceptibility from Haack et al.'s multi-species BGK kinetic equation [27] and recover, as a limit, the known multi-species Mermin susceptibility. We call

our result the completed Mermin dielectric function because including momentum conservation does not alter Mermin's correction, but does enforce the frequency sum rule.

Both XRTS and Bremsstrahlung emission models require estimates of the ions' DSFs [2, 6]. In inertial confinement fusion (ICF) experiments, hydrodynamic instabilities inject the ICF capsule's ablator material, such as carbon into the deuterium-tritium hot spot [28]. The carbon contaminants create a multi-species plasma, which is tractable with our multi-species susceptibility. We apply the completed Mermin model to understand how conservation laws impact carbon contaminated DSFs and find that momentum conservation has a qualitative impact on the behavior of the contaminated DSF.

In estimates of dynamical conductivity, the measured DC conductivity can be suppressed, while the measured optical conductivity is enhanced relative to the Drude model. Thus, Chen et al. recommend the use of non-Drude conductivities, *e.g.*, Drude-Smith when fitting optical conductivity measurements [7]. The single-species limit of our completed Mermin model offers a new non-Drude dynamical conductivity model, which quantifies how conservation laws impact the conductivity. We show that partial number and momentum conservation can also suppress the DC conductivity and enhance the optical conductivity. We compare our completed Mermin model to the established Drude-Smith model and find that Smith's parameter violates number conservation.

The structure of the chapter is as follows. In Sec. 3.2, we introduce the multi-species BGK kinetic equation and show how to conserve local number, momentum, and energy using local variations of the chemical potential, drift velocity, and temperature. In Sec. 3.3, we develop applications of the expanded multi-species kinetic equation. First, we derive the multi-species completed Mermin susceptibility and show that it satisfies sum rules not met by the original multi-species Mermin model.. Next, we investigate the DSF of mixtures at NIF direct drive nT conditions. We quantify the impact of the light species approximation and demonstrate that momentum conservation has a qualitative impact on the shape of the DSF. Then we observe the impact of carbon contaminants on the light species DSF. Finally, we derive a dynamical conductivity from our single-species completed Mermin and demonstrate how number and momentum conservation parameters impact the

conductivity. We compare this new conductivity to both the Drude and Drude-Smith conductivity models to demonstrate that Smith's phenomenological parameter violates number conservation. The details for implementing our new model can be found in the appendices.

3.2 Kinetics

3.2.1 Describing the System

We consider a classical system containing N different charged particle species. Many-body particle interactions and externally applied fields both govern the dynamics of this system. We account for the many-body interactions with an effective one-body description for each of the N species. To this end, two terms govern the dynamics of a single particle: an effective single particle Hamiltonian (*i.e.*, a mean field interaction) and an effective single body inter- and intra-species collisional operator.

3.2.2 Formulating the system

The dynamics of the single particle distribution function are governed by

$$\left(\partial_t + \mathbf{v}\cdot\nabla_{\mathbf{r}} + \mathbf{a}_i^{\text{tot}}\cdot\nabla_{\mathbf{v}}\right) f_i(\mathbf{r},\mathbf{v},t) = \sum_j Q_{ij}. \tag{3.1}$$

$^{\text{tot}}_{i}$ denotes the total acceleration for the i^{th} species and is defined as follows

$$m_i\mathbf{a}_i^{\text{tot}} = -\nabla_{\mathbf{r}}\Phi^{\text{ext}} - \nabla_{\mathbf{r}}\Phi_i^{\text{ind}}, \tag{3.2}$$

where the external potential Φ^{ext} is inherently a one-body potential and the induced potential Φ_i^{ind} is an effective one-body potential that describes the electrostatic energy. We assume both Φ^{ext} and Φ_i^{ind} are of the order δ. In Fourier space, the induced potential is represented by the Hartree potential

$$\Phi_i^{\text{ind}} \equiv \sum_j v_{ij}(k)\delta n_j(\mathbf{k},\omega). \tag{3.3}$$

This expresses how the interaction $vij(k)$ between species i and j causes density fluctuations $\delta n_j(\mathbf{k},\omega)$ in species j, thereby affecting the electrostatic potential Φ_i^{ind} experienced by species i. This formulation gives the flexibility for different species to contribute differently to the induced potential. In the case where the species interact via the Coulomb potential, $v_{ij}(k) = 4\pi e^2 Z_i Z_j/k^2$.

In Eq(3.1), Q_{ij} denotes the effective one-body description of the inter-species $i = j$ collisions and intra-species $i \neq j$ collisions. We adopt Haack et al.'s multi-species relaxation to equilibrium as our collisional operator [27]

$$Q_{ij} \equiv \frac{1}{\tau_{ij}} \left(M_{ij}(\mathbf{r}, \mathbf{v}, t) - f_i(\mathbf{r}, \mathbf{v}, t) \right). \tag{3.4}$$

The Maxwellian target distribution M_{ij} is defined by

$$M_{ij} \equiv \frac{g_i}{\lambda_{i,th}^3} \left(\frac{m_i}{2\pi T_{ij}(\mathbf{r}, t)} \right)^{3/2} e^{-\frac{(\varepsilon_{ij}(\mathbf{r},t) - \mu_i(\mathbf{r},t))}{T_{ij}(\mathbf{r},t)}}, \tag{3.5}$$

$$E_{ij} \equiv \frac{m_i}{2}(v - u_{ij}(\mathbf{r}, t))^2, \tag{3.6}$$

$$\frac{1}{\tau_i} \equiv \sum_j \frac{1}{\tau_{ij}}. \tag{3.7}$$

In this context, $\lambda_i(\mathbf{r}, t) \equiv \frac{g_i}{\lambda_{i,th}^3} e^{\mu_i(\mathbf{r},t)/T_{ij}(\mathbf{r},t)}$ is the local fugacity. The target velocity u_{ij} and target temperature T_{ij} are defined so that the collision operator satisfies the H-theorem and the number, momentum, and energy conservation laws. However, in this chapter, we will only use them as expansion parameters. We have suppressed the frequency dependence in the relaxation time τ_{ij}, but this needs to be accounted for if the energy levels involved in the collision process lie above the Fermi energy [20]. The standard interpretation of the relaxation approximation is that Vlasov dynamics govern the particle's phase space dynamics. Additionally, every infinitesimal time interval dt, a fraction dt/τ_{ij} of the particles experience a collision event that sets their velocity distribution to target M_{ij}.

3.2.3 Linearizing the Multi-species BGK Equation

To linearize the kinetic equation, Eq(3.1), we assume that the i^{th} species' distribution function $f_i(\mathbf{r}, \mathbf{v}, t)$ and the target Maxwellian $M_{ij}(\mathbf{r}, \mathbf{v}, t)$ have small deviations of order δ from the global equilibrium distribution

$$f_i(\mathbf{r}, \mathbf{v}, t) = \lambda_i \, f_{iG}(v) + \lambda_i \, \delta f_{iG}(\mathbf{r}, \mathbf{v}, t), \tag{3.8}$$

$$M_{ij}(\mathbf{r}, \mathbf{v}, t) = \lambda_i \, f_{iG}(v) + \lambda_i \, \delta M_{ij}(\mathbf{r}, \mathbf{v}, t). \tag{3.9}$$

The global fugacity $\lambda_i \equiv \frac{g_i}{\lambda_{i,th}^3} e^{\mu_i/T}$ has been factored out from each term and $f_{iG}(v)$ is the global (G) mixture equilibrium distribution, defined

$$f_{iG}(v) \equiv \left(\frac{m_i}{2\pi T}\right)^{3/2} \exp\left(-\frac{m_i}{2T}(v-u)^2\right), \tag{3.10}$$

$$\mathbf{u} \equiv \left(\sum m_i n_i \mathbf{u}_i\right) / \sum_i m_i n_i, \tag{3.11}$$

$$T \equiv \left(\sum n_i T_i\right) / \sum_i n_i. \tag{3.12}$$

Lastly, the deviations from global equilibrium define the density fluctuations as

$$\delta n_i(\mathbf{r}, t) \equiv \int d\mathbf{v}\, \delta f_{iG}(\mathbf{r}, \mathbf{v}, t). \tag{3.13}$$

We insert expansions Eq(3.8) and Eq(3.9) into Eq(3.1), cancel the fugacity factors, and then Fourier transform to arrive at

$$\left(\mathbf{v}\cdot\mathbf{k} - \omega_{\tau_i}\right) \delta f_{iG}(\mathbf{k}, \mathbf{v}, \omega) + \sum_j \frac{i}{\tau_{ij}} \delta M_{ij}(\mathbf{r}, \mathbf{v}, t) = m_i^{-1} \mathbf{k}\cdot\nabla_{\mathbf{v}} f_{iG}\, \Phi^{tot}. \tag{3.14}$$

The Fourier conventions and relevant steps are described in Appendix 3A. We have grouped δf_{iG} terms and thus the frequency has been shifted $\omega_{\tau_j} \equiv \omega + i/\tau_j$.

In Eq(3.14), $\delta M_{ij}(\mathbf{r}, \mathbf{v}, t)$ is an unknown term. The target Maxwellian M_{ij}, from Eq(3.5), recovers the global mixture equilibrium distribution f_{iG}, from Eq(3.10), when the target velocity $\mathbf{u}_{ij}(\mathbf{r}, t)$ reduces to the bulk velocity $\mathbf{u}$ and the target temperature $T_{ij}(\mathbf{r}, t)$ reduces to the bulk temperature T. This implies that at zeroth order $\mathbf{u}_{ij}(\mathbf{r}, t) \approx \mathbf{u}$ and $T_{ij}(\mathbf{r}, t) \approx T$. Therefore, $\delta M_{ij}(\mathbf{r}, \mathbf{v}, t)$ contains the target Maxwellian's local deviations in chemical potential, velocity, and temperature. We expand $\delta M_{ij}(\mathbf{r}, \mathbf{v}, t)$ to linear order as

$$\delta M_{ij} = \left(\frac{\partial M_{ij}}{\partial \mu_i}\Big|_{M_{ij}=f_{iG}}\right) \delta\mu_i + \left(\frac{\partial M_{ij}}{\partial \mathbf{u}_{ij}}\Big|_{M_{ij}=f_{iG}}\right) \delta\mathbf{u}_{ij} + \left(\frac{\partial M_{ij}}{\partial T_{ij}}\Big|_{M_{ij}=f_{iG}}\right) \delta T_{ij}. \tag{3.15}$$

We factor out $-\dfrac{\partial f_{iG}}{\partial E_i}$ from every term, where $E_i = \frac{1}{2} m_i v^2$. By applying the chain rule, we

reformulate $\dfrac{\partial f_{iG}}{\partial E_i}$ as

$$\frac{\partial f_{i,0}^{GC}}{\partial E_i} = \left(\mathbf{k}\cdot\frac{\partial f_{i,0}^{GC}}{\partial \mathbf{v}}\right)\left(\mathbf{k}\cdot\frac{\partial E_i}{\partial \mathbf{v}}\right)^{-1}. \tag{3.16}$$

Inserting Eq(3.16) into Eq(3.15) yields our final expression for δM_{ij}

$$\delta M_{ij} = -\frac{m_i^{-1}\mathbf{k}\cdot\nabla_{\mathbf{v}} f_{iG}}{\mathbf{k}\cdot\mathbf{v}}\left(\delta\mu_i + \mathbf{p}_i\cdot\delta\mathbf{u}_{ij} + \left(\frac{p_i^2}{2m_i} - \mu_i\right)\frac{\delta T_{ij}}{T_{ij}}\right). \tag{3.17}$$

Inserting Eq(3.17) into Eq(3.14) yields

$$\begin{aligned}\delta f_{iG}(\mathbf{k},\mathbf{v},\omega) = {} & \frac{m_i^{-1}\,\mathbf{k}\cdot\nabla_{\mathbf{v}} f_{iG}(v)}{\mathbf{v}\cdot\mathbf{k} - \omega_{\tau_i}} \\ & \times\left(U_{tot} + \frac{i}{\mathbf{v}\cdot\mathbf{k}}\sum_j \frac{1}{\tau_{ij}}\left(\delta\mu_i + \mathbf{p}_i\cdot\delta\mathbf{u}_{ij} + \left(\frac{p_i^2}{2m_i} - \mu_i\right)\frac{\delta T_{ij}}{T}\right)\right),\end{aligned} \tag{3.18}$$

which indicates that external potential, induced potential, as well as local deviations in chemical potential, velocity, and temperature can all create perturbations from global equilibrium.

3.2.4 Incorporating Conservation Laws using Linear Perturbations

Previous single species models violated the momentum conservation law to account for scattering events. This violation is necessary to predict that a gas of electrons, implicitly contained in a metal, has finite conductivity. Since we are accounting for all N species in the system, it is physical to include momentum conservation.

In Eq(3.18), $\delta\mu_i$, $\delta\mathbf{u}_{ij}$, and δT_{ij} are unknowns. The expressions for these three unknowns are constrained with number, momentum, and energy collisional invariants to enforce conservation laws. Our collisional invariants are formulated as

$$\int d\mathbf{v}\, Q_{ij} = 0, \tag{3.19a}$$

$$\int d\mathbf{v}\, m_i\mathbf{v}Q_{ij} + \int d\mathbf{v}\, m_j\mathbf{v}Q_{ji} = 0, \tag{3.19b}$$

$$\int d\mathbf{v}\,\frac{m_i}{2}v^2 Q_{ij} + \int d\mathbf{v}\,\frac{m_j}{2}v^2 Q_{ji} = 0. \tag{3.19c}$$

For example, satisfying Eq(3.19a) ensures the number of species i remains constant before and after collisions with species j.

It may erroneously appear that our collisional invariants uniquely determine the value of the local perturbations ($\delta\mu_i$, $\delta\mathbf{u}_{ij}$, and δT_{ij}), but notice that $\delta\mu_i$ and δT_{ij} are accompanied by even moments of momentum in Eq(3.17). Thus, the mass collisional invariant Eq(3.19a) and energy collisional invariant Eq(3.19c) will both preserve terms with $\delta\mu_i$ and δT_{ij}, coupling these two constraints together. Since $\delta\mu_i$ depends on a single index and δT_{ij} depends on two indices, there remains an ambiguity about how to select j for the number density constraint Eq(3.19a). This issue could be resolved by changing $\delta\mu_i$ to $\delta\mu_{ij}$ and Eq(3.19a) to

$$\int d\mathbf{v}\, m_i Q_{ij} + \int d\mathbf{v}\, m_j Q_{ji} = 0. \tag{3.20}$$

However, this mass conservation constraint would allow the system to convert species i into species j to reach chemical equilibrium, which is unphysical. Therefore, no attempt is made to conserve number, momentum and energy simultaneously. Instead, we limit ourselves to the isothermal $\delta T_{ij} = 0$ case, conserving only number and momentum. We explore the error introduced by the isothermal approximation for a single-species dielectric in section 3.3.4. In short, we find that energy conservation corrections enter at order k^2 in the single species limit.

We can conserve momentum even though $\delta\mathbf{u}_{ij}$ also depends on i, j because $\delta\mu_i$ and $\delta\mathbf{u}_{ij}$ are accompanied by even and odd powers of momentum, respectively, in Eq(3.17). Therefore $\delta\mathbf{u}_{ij}$ does not appear in the mass collisional invariant Eq(3.19a) and $\delta\mu_i$ does not appear in the momentum collisional invariant Eq(3.19b). Hence, these equations are decoupled. Evaluating constraints Eq(3.19a) and Eq(3.19b) produces

$$\delta\mu_i = -\delta n_i / B^M_{i,0}, \tag{3.21a}$$

$$\mathbf{k}\cdot\delta\mathbf{u}_{ij} = \omega\left(\frac{m_i\delta n_i\tau_{ji} + m_j\delta n_j\tau_{ij}}{m_i n_{0,i}\tau_{ji} + m_j n_{0,j}\tau_{ij}}\right). \tag{3.21b}$$

where

$$C^M_{i,n}(\mathbf{k},\omega) \equiv \int d\mathbf{v}|\mathbf{p}|^n \frac{m_i^{-1}\mathbf{k}\cdot\nabla_{\mathbf{v}} f_{iG}}{\mathbf{v}\cdot\mathbf{k}-\omega}, \tag{3.22a}$$

$$B^M_{i,n} \equiv C^M_{i,n}(\mathbf{k},0). \tag{3.22b}$$

The momentum integration is conducted in Appendix 3B. Together Eq(3.21a), Eq(3.21b), and $\delta T_{ij} = 0$ constrain the unknowns in our system's dynamic response.

3.3 Results

3.3.1 Susceptibilities

We begin our results section with the susceptibility, from which other quantities will be produced. The susceptibility quantifies how an external potential causes density fluctuations, δn, from global equilibrium.

$$\delta n_i(k,\omega) = \chi_i(k,\omega)\Phi^{\text{ext}}(k,\omega). \tag{3.23}$$

The index i (or j) runs over all species, from 1 to N. We formulate the system's dynamical response by integrating Eq(3.18) over velocity; the steps are shown in Appendix 3C. Our final result is

$$\begin{aligned}\delta n_i = C^M_{i,0}(\Phi^{\text{ext}} + \sum_j v_{ij}\delta n_j) + \frac{i}{\omega_{\tau_i}\tau_i}\left(C^M_{i,0} - B^M_{i,0}\right)\delta\mu_i(\mathbf{k}) \\ + C^M_{i,0}\frac{m_i}{k^2}\sum_j \frac{i}{\tau_{ij}}\mathbf{k}\cdot\delta\mathbf{u}_{ij} + \sum_j \frac{i}{\tau_{ij}}\left(\left(\frac{C_{i,2}-B_{i,2}}{2m_i}\right) - \mu_i(C_{i,0}-B_{i,0})\right)\frac{\delta T_{ij}}{T_{ij}}.\end{aligned} \tag{3.24}$$

The j index runs over all species ($j = 1,\ldots,N$). Substituting the expressions for $\delta\mu_i$ from Eq(3.21a), $\delta\mathbf{u}_{ij}$ from Eq(3.21b), and $\delta T_{ij} = 0$ yields

$$\begin{aligned}\delta n_i = C^M_{i,0}(\Phi^{\text{ext}} + \sum_j v_{ij}(k)\delta n_j) - \frac{i}{\omega_{\tau_i}\tau_i}\left(C^M_{i,0} - B^M_{i,0}\right)\delta n_i/B^M_{i,0} \\ + iC^M_{i,0}\frac{m_i\omega}{k^2}\sum_j \frac{1}{\tau_{ij}}\left(\frac{m_i\delta n_i\tau_{ji} + m_j\delta n_j\tau_{ij}}{m_i n_{0,i}\tau_{ji} + m_j n_{0,j}\tau_{ij}}\right).\end{aligned} \tag{3.25}$$

To match the functional form in Eq(3.23), we group the δn_i terms

$$\begin{aligned}C^M_{i,0}\Phi^{\text{ext}} =& \delta n_i - v_{ii}(k)C^M_{i,0}\delta n_i - \frac{i}{\omega_{\tau_i}\tau_i}\left(1 - \frac{C^M_{i,0}}{B^M_{i,0}}\right)\delta n_i - \frac{i\omega m_i}{k^2 n_{i,0}\tau_{ii}}C^M_{i,0}\delta n_i \\ &- C^M_{i,0}\sum_{j\neq i} v_{ij}(k)\delta n_j - \frac{i\omega m_i}{k^2}C^M_{i,0}\sum_{j\neq i}\frac{1}{\tau_{ij}}\left(\frac{m_i\delta n_i\tau_{ji} + m_j\delta n_j\tau_{ij}}{m_i n_{0,i}\tau_{ji} + m_j n_{0,j}\tau_{ij}}\right).\end{aligned} \tag{3.26}$$

As an illustrative example and for future applications, we limit ourselves to two species. The susceptibility can be determined using the 2x2 matrix inversion formula. The result is

$$\chi_{1,CM} = \frac{C_{1,0}^M \left(\varepsilon_2^* + \left(v_{12}(k) + i\frac{\omega}{k^2}\,\frac{m_1 m_2}{m_1 n_{0,1}\tau_{21} + m_2 n_{0,2}\tau_{12}}\right) C_{2,0}^M\right)}{\varepsilon_1^*\varepsilon_2^* - C_{1,0}C_{2,0}\left(v_{12}(k) + i\frac{\omega}{k^2}\,\frac{m_1 m_2}{m_1 n_{0,1}\tau_{21} + m_2 n_{0,2}\tau_{12}}\right)\left(v_{21}(k) + i\frac{\omega}{k^2}\,\frac{m_1 m_2}{m_1 n_{0,1}\tau_{21} + m_2 n_{0,2}\tau_{12}}\right)}, \tag{3.27a}$$

$$\chi_{2,CM} = \frac{C_{2,0}^M \left(\varepsilon_1^* + \left(v_{21}(k) + i\frac{\omega}{k^2}\,\frac{m_1 m_2}{m_1 n_1\tau_{21} + m_2 n_2\tau_{12}}\right) C_{1,0}^M\right)}{\varepsilon_1^*\varepsilon_2^* - C_{1,0}C_{2,0}\left(v_{12}(k) + i\frac{\omega}{k^2}\,\frac{m_1 m_2}{m_1 n_{0,1}\tau_{21} + m_2 n_{0,2}\tau_{12}}\right)\left(v_{21}(k) + i\frac{\omega}{k^2}\,\frac{m_1 m_2}{m_1 n_{0,1}\tau_{21} + m_2 n_{0,2}\tau_{12}}\right)}, \tag{3.27b}$$

$$\varepsilon_1^* = \varepsilon_1 - \frac{i}{\omega_{\tau_1}\tau_1}\left(1 - \frac{C_{1,0}^M}{B_{1,0}^M}\right) - i\frac{\omega}{k^2}\left(\frac{m_1}{n_{1,0}\tau_{11}} + \frac{\tau_{21}}{\tau_{12}}\frac{m_1^2}{m_1 n_{0,1}\tau_{21} + m_2 n_{0,2}\tau_{12}}\right) C_{1,0}^M, \tag{3.27c}$$

$$\varepsilon_2^* = \varepsilon_2 - \frac{i}{\omega_{\tau_2}\tau_2}\left(1 - \frac{C_{2,0}^M}{B_{2,0}^M}\right) - i\frac{\omega}{k^2}\left(\frac{m_2}{n_{2,0}\tau_{22}} + \frac{\tau_{12}}{\tau_{21}}\frac{m_2^2}{m_1 n_{0,1}\tau_{21} + m_2 n_{0,2}\tau_{12}}\right) C_{2,0}^M. \tag{3.27d}$$

This expression is the primary result of this chapter. We refer to it as the multi-species completed Mermin susceptibility. For numerical implementation, this result is broken down into dimensionless parameters and common special functions in Appendix 3D.

We recover the multi-species Mermin-like susceptibility [29, 30] from Eq(3.27) by neglecting the terms with a factor of ω/k^2. The result is

$$\chi_{1,M} \equiv C_{1,0}^M\,\frac{\varepsilon_2^* + v_{12}(k)C_{2,0}^M}{\varepsilon_1^*\varepsilon_2^* - C_{1,0}C_{2,0}v_{12}^2(k)}, \tag{3.28a}$$

$$\chi_{2,M} \equiv C_{2,0}^M\,\frac{\varepsilon_1^* + v_{12}(k)C_{1,0}^M}{\varepsilon_1^*\varepsilon_2^* - C_{1,0}C_{2,0}v_{12}^2(k)}, \tag{3.28b}$$

$$\varepsilon_j^* = \varepsilon_j - \frac{i}{\omega_{\tau_j}\tau_j}\left(1 - \frac{C_{j,0}^M}{B_{j,0}^M}\right). \tag{3.28c}$$

If we also let the relaxation time τ go to infinity, we recover the random phase approximation (RPA). Notice in both the Mermin and the RPA susceptibilities that the interaction potential $v_{12}(k)$ in Eq(3.28) is the only term coupling species 1's susceptibility to species 2's susceptibility. Whereas, for the completed Mermin Eq(3.27) the conservation of momentum also couples the susceptibilties.

We recover the single species limit of the completed Mermin model by neglecting the coupling

terms in Eq(3.27),

$$\chi^{CM} \equiv \frac{C_0}{\varepsilon - \dfrac{i}{\omega_\tau \tau}\left(1 - \dfrac{C_0}{B_0}\right) - \frac{im\omega}{k^2 n_0 \tau} C_0}. \tag{3.29}$$

Whereas, the single species Mermin is given

$$\chi^{M} \equiv \frac{C_0}{\varepsilon - \dfrac{i}{\omega_\tau \tau}\left(1 - \dfrac{C_0}{B_0}\right)}. \tag{3.30}$$

Comparing Eq(3.30) to Eq(3.29), the completed Mermin susceptibility includes the momentum conservation correction

$$\frac{im\omega}{k^2 n_{i,0} \tau}\, C_{i,0}. \tag{3.31}$$

The form of this momentum conservation correction Eq(3.31) matches Morawetz and Fuhrmann's single species local field correction [21]. Eq(3.31) arises from the single species version of the momentum constraint, Eq(3.21b),

$$\mathbf{k} \cdot n_0 \delta\mathbf{u} = \omega \delta n. \tag{3.32}$$

Comparatively, Mermin produced his number conservation constraint by enforcing $\mathbf{k} \cdot \mathbf{j} = \omega \delta n$ [15]. Our momentum constraint, Eq(3.32), differs only in that $\mathbf{j} = n_0\, \delta\mathbf{u}$. This suggests that enforcing $\mathbf{j} = n_0\, \delta\mathbf{u}$ in the Mermin's continuity equation and varying local equilibrium with respect to velocity leads to momentum conservation. Hence why we refer to our susceptibility with the moniker "completed Mermin".

3.3.2 Dielectric functions

The dielectric function is defined as

$$\Phi_i^{\text{ind}}(k, \omega) \equiv \left(\frac{1}{\varepsilon_i(k, \omega)} - 1\right) \Phi^{\text{ext}}(k, \omega). \tag{3.33}$$

Inserting the multi-species Hartree potential Eq(3.3) and comparing to the definition of the susceptibility Eq(3.23) yields an expression for the dielectric function in terms of the susceptibility

$$\frac{1}{\varepsilon_i(k,\omega)} = 1 + \sum_j v_{ij}(k)\chi_j(k,\omega). \tag{3.34}$$

For single species mean field corrected susceptibility $\chi = C_0/(1-v(k)C_0)$ this expression produces the common expression $\varepsilon(k,\omega) = 1 - v(k)C_0(k,\omega)$.

The fulfillment of sum rules, which assesses the quality of a dielectric function moment by moment, is an essential property of every dielectric function [31]. The frequency sum (f-sum) rule, which assesses the satisfaction of the local continuity equation, is given by

$$\int_{-\infty}^{\infty} d\omega\, \omega \mathrm{Im}\{\varepsilon_i^{-1}\} = -\pi \sum_j \frac{\omega_{p,e}^2}{k_{D,e}^2}\frac{m_e}{m_j}\frac{n_j}{T} v_{ij}(k)k^2. \tag{3.35}$$

For an isolated species of electrons in the unscreened limit, the RHS of Eq(3.35) reduces to the familiar $-\pi\omega_p^2$. Another significant sum rule is the perfect screening sum rule, valid when there's negligible k dependence—indicating a purely local relationship between the induced density and the external potential [32]. It is given by

$$\lim_{k\to 0}\lim_{\tilde{\kappa}\to 0}\int_{-\infty}^{\infty}\frac{d\omega}{\omega}\mathrm{Im}\{\varepsilon^{-1}\} = -\pi. \tag{3.36}$$

For the screening sum rule, the no screening limit (*i.e.*, $\tilde{\kappa}\to 0$) is taken first and the long wavelength limit (*i.e.*, $k\to 0$) is taken second.

We produce analytic expressions of $\lim_{\mathbf{k}\to 0}\mathrm{Im}\{\varepsilon^{-1}\}$ from each known collisional single species case: Mermin (M) Eq(3.30), our completed Mermin (CM) Eq(3.29), as well as Atwal-Ashcroft (AA) which locally conserves number, momentum, and energy [20]. In terms of dimensionless parameters, the functional forms are:

$$\lim_{\mathbf{k}\to 0}\mathrm{Im}\left\{\frac{1}{\varepsilon^{\mathrm{M}}}\right\} = -\frac{\zeta^2(\tilde{\omega}/\tilde{\tau})}{\zeta^4(\tilde{\omega}/\tilde{\tau})^2 + (\zeta^2\tilde{\omega}^2-1)^2}, \tag{3.37a}$$

$$\lim_{\mathbf{k}\to 0}\mathrm{Im}\left\{\frac{1}{\varepsilon^{\mathrm{CM}}}\right\} = -\frac{\tilde{k}^2\tilde{\tau}\tilde{\omega}}{-2\tilde{k}^2(\zeta^2\tilde{\omega}^2-1) + (1+\tilde{\tau}^2\tilde{\omega}^2)(\zeta^2\tilde{\omega}^2-1)^2}, \tag{3.37b}$$

$$\lim_{\mathbf{k}\to 0}\mathrm{Im}\left\{\frac{1}{\varepsilon^{\mathrm{AA}}}\right\} = -\frac{\tilde{k}^2\tilde{\tau}\tilde{\omega}}{-2\tilde{k}^2\left(\frac{1+3\tilde{\tau}^2\tilde{\omega}^2-2\zeta^{-2}\tilde{\tau}^2}{1+\tilde{\tau}^2\tilde{\omega}^2}\right)(\zeta^2\tilde{\omega}^2-1) + \frac{1}{3}(1+\tilde{\tau}^2\tilde{\omega}^2)(\zeta^2\tilde{\omega}^2-1)^2}. \tag{3.37c}$$

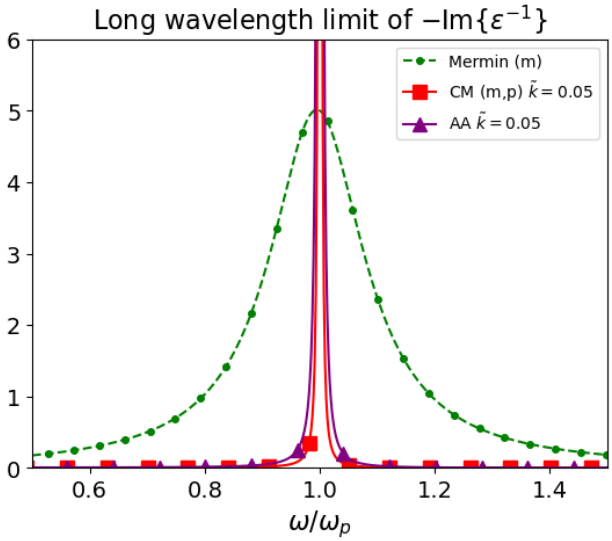

Figure 3.1 Plots of the long wavelength expansion of $\mathrm{Im}\{\varepsilon^{-1}\}$ for the Mermin (green), completed Mermin (CM, red), and Atwal-Ashcroft (AA, purple) from Eq(3.37). We evaluate the function at $\tilde{k} \approx 0.05$, $(\omega_p\tau)^{-1} = .2$, $\zeta^2 = 1$. The completed Mermin and Atwal-Ashcroft have narrower widths than Mermin because Mermin's width parameter $1/\tilde{\tau}$ remains finite in the long wavelength limit.

We have used electronic quantities to render these equations dimensionless: $\tilde{\tau} = \tau\omega_{p,e}$, $\tilde{\omega} = \omega/\omega_{p,e}$, $\tilde{k} = k/k_{D,e}$, and $\zeta_i \equiv \sqrt{m_i/m_e}$. The steps to compute these dimensionless expressions are shown in Appendix 3E.

All three functional forms in Eq(3.37) are Lorentzian. Mermin's width parameter is $1/\tilde{\tau}$, while both completed Mermin and Atwal-Ashcroft width parameters are $\tilde{k}$. As $k \to 0$ the completed Mermin and Atwal-Ashcroft dielectric functions become Dirac deltas. Figure 3.1 plots the long-wavelength expansions from Eq(3.37) at a wave number of $\tilde{k} \approx 0.05$.

When the width becomes infinitesimal, we recover a Dirac delta function

$$\mathrm{Im}\{\varepsilon^{-1}\} = -\pi\omega\,\delta(\omega - \omega_p), \tag{3.38}$$

By direct substitution, we see that the Dirac delta satisfies both sum rules, Eq(3.35) and Eq(3.36). All of the above dielectric functions becomes a Dirac delta function in the RPA limit (*i.e.*, $\tau \to \infty$). Whereas, in the long wavelength limit (*i.e.*, $k \to 0$) only the completed Mermin and the Atwal-Ashcroft dielectric functions reduce to the Dirac delta function. While the Mermin dielectric function does not converge to a Dirac delta, it still has no k dependence. Therefore, in the long wavelength limit, it only satisfies the screening sum rule.

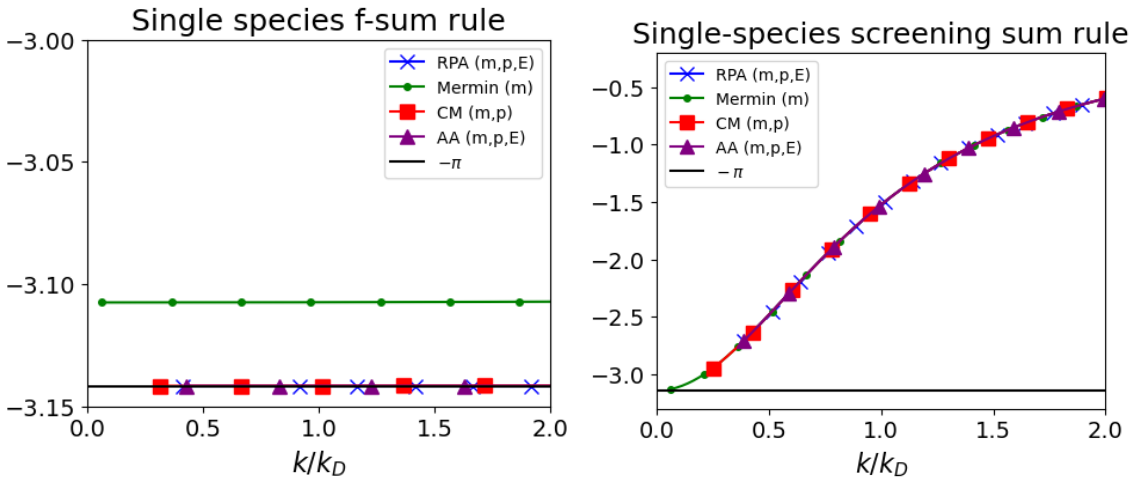

Figure 3.2 Left: A plot of the frequency sum (f-sum) rule, Eq(3.35), for single-species random phase approximation (RPA, blue), Mermin (green), completed Mermin (CM, red), and Atwal-Ashcroft (AA, purple). Right: A plot of the screening sum rule, Eq(3.36), for single-species RPA (blue), Mermin (green), and completed Mermin (red). In both plots wiggles arise in the long wavelength limit because the susceptibilities become Dirac deltas and numerical integration becomes impossible, we have truncated our plots before that happens.

We can also assess whether the sum rules hold outside the long wavelength limit. The sum rules are computed numerically at a finite k and the results are shown in Figure 3.2. For the f-sum rule, only the Mermin dielectric function does not integrate to $-\pi$. Thus, the behavior at finite k matches the behavior in the long wavelength limit. For the screening sum rule, all results converge to $-\pi$ in the long wavelength limit. Additionally, Figure 3.3 shows that the multi-species sum rules exhibit the same sum rule behavior as their single species counterparts.

3.3.3 Dynamic Structure Factors

The classical Fluctuation Dissipation Theorem (FDT) defines the DSF as

$$S(k,\omega) = \frac{-2T}{n_i(\omega/\omega_{p,e})}\left(Z_i\sqrt{\frac{n_i}{n_e}\frac{m_e}{m_i}}\right)\chi''(k,\omega). \tag{3.39}$$

χ_i'' is the imaginary part of the susceptibility and Z_i is the effective charge of the i^{th} species. The DSF is an essential input into HED experimental diagnostics. In this section, we examine contaminants with high atomic numbers affect deuterium's (D) and tritium's (T) DSFs in an ICF hot spot. We consider 2 cases. In the first case, we neglect carbon (C) contaminants and consider an uncontaminated D and T plasma; we explore the impact of the light species approximation, whereby

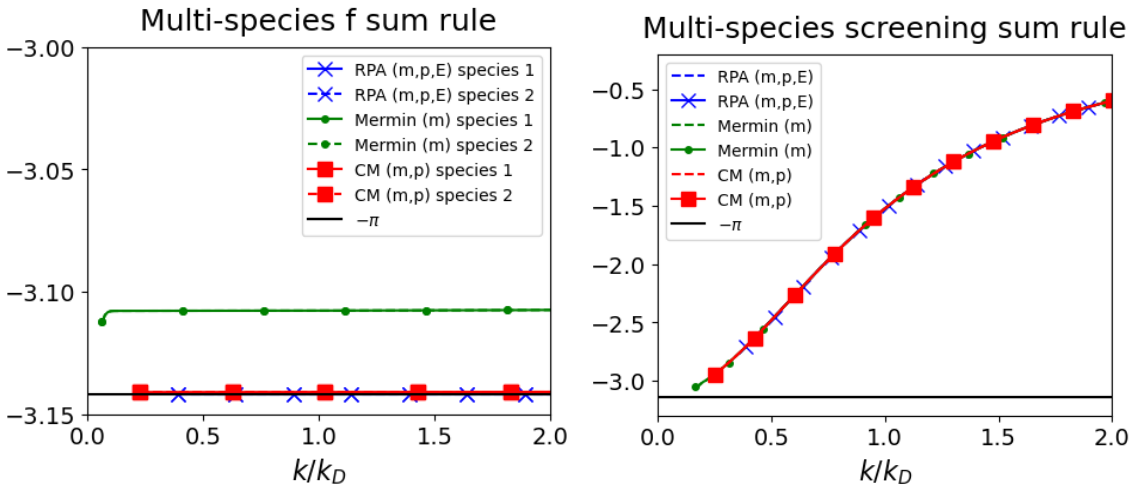

Figure 3.3 Left: A plot of the frequency sum rule, Eq(3.35), for multi-species RPA (blue), Mermin (green), and completed Mermin (red). Only the Mermin dielectric function does not integrate to $-\pi$ (black). Right: A plot of the screening sum rule, Eq(3.36), for multi-species RPA (blue), Mermin (green), and completed Mermin (red). All results converge to $-\pi$ (black) in the long wavelength limit. In both plots the susceptibilities become Dirac deltas in the long wavelength limit, making numerical integration impossible. We truncated our plots before that happens.

the D and T are treated as a single species. In the second case, we include C contaminants in the hot spot and use the light species approximation to reduce the contaminated D, T, and C plasma to a mixture of only light species and C. Based on Hu et al.'s work, we assume that the National Ignition Facility (NIF) direct drive hotspot is at a mass density of 1002 g/cc and temperature of 928 eV [33].

In the first case, we neglect C contaminants. Given mass density ρ, the number density of the individual components is determined by

$$\rho = m_D n_D + m_T n_T. \tag{3.40}$$

We consider three different scenarios: pure D (*i.e.*, $n_T = 0$), pure T (*i.e.*, $n_D = 0$), and equal parts D and T (*i.e.*, $n_D = n_T$) Additionally, we consider the light species approximation and treat D and T as indistinguishable components of a single species plasma. The relative number density of the tritium and deuterium determines the average mass of this light (L) species. We formulate this as

$$m_L = \frac{n_D m_D + n_T m_T}{n_D + n_T}, \tag{3.41a}$$

$$n_L = n_D + n_T, \tag{3.41b}$$

Table 3.1 Tabulated plasma parameters for a pure deuterium (D) plasma, a pure tritium (T) plasma, a pure L plasma, and a mixed D and T plasma; all plasmas are at a mass density of 1002 g/cc and temperature of 928 eV [33]. The effective charge of the ion Z is computed using More's Thomas-Fermi ionization estimate [34]. The coupling parameter is defined $\Gamma_i \equiv (Z_i)^2 / a_i T$ where $a_i = (3Z_i/4\pi n_e)^{1/3}$ and $n_e = \sum_i Z_i n_i$. The screening parameter is defined $\tilde{\kappa} \equiv (\lambda_s k_{D,e})^{-1}$, where the screening length is given in Stanton and Murillo's work [35]. Lastly, for ν we use the temperature relaxation collision rates defined in Haack et al. [27].

Uncontaminated deuterium-tritium plasmas

	species	n (1/cc)	Z	Γ	$\tilde{\kappa}$	$\nu_{i=j}$ (1/s)	$\nu_{i\neq j}$ (1/s)
No mix	pure L	2.40e26	0.966	0.147	1.176	6.30e-03	N/A
No mix	pure D	2.00e26	0.966	0.138	1.198	5.42e-03	N/A
No mix	pure T	3.00e26	0.966	0.158	1.146	7.56e-03	N/A
$n_T = n_D$	mixed D	1.19e+26	0.965	0.116	1.196	3.47e-03	3.04e-03
	mixed T	1.19e+26	0.965	0.116	1.196	2.84e-03	3.04e-03

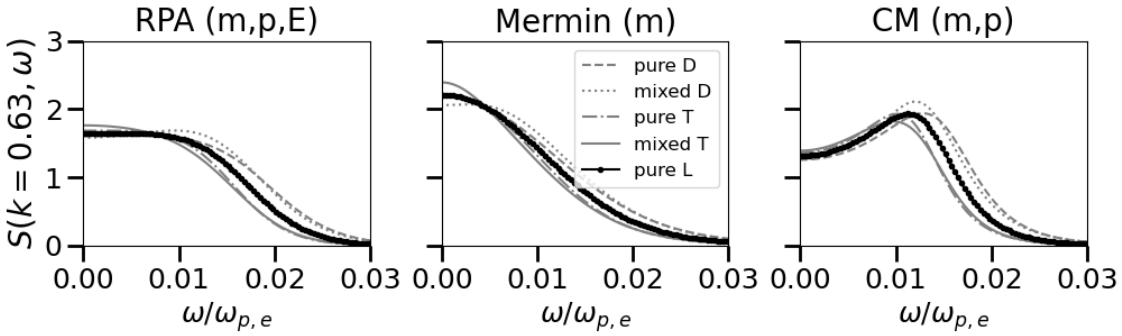

Figure 3.4 All plots compare $S(k, \omega)$ at fixed $k/k_{D,e} = .63$ across different DSF models. Each panel contains a pure deuterium (pure D), deuterium mixed with tritium (mixed D), a pure tritium (pure T) and tritium mixed with deuterium (mixed T) plotted in gray. Each panel also contains a pure light species [defined Eq(3.41)] plotted in solid line. The plots show that all five cases have qualitative agreement across a given set of conservation laws. However, the completed Mermin model has a stronger plasmon peak than the RPA.

From these equations, we can deduce that $\rho = n_L m_L$. From Eq(3.40) and Eq(3.41), we compute the number density and the other relevant plasma parameters, which we list in Table 3.1. For the various plasmas, we plot the DSF at a fixed k in Figure 3.4. The single light species DSF is in qualitative agreement with all pure and mixed cases. This suggests that the light species approximation is reasonable for the DSF of a D and T plasma at 1002 g/cc and temperature of 928 eV. While the light species approximation does not qualitatively change the DSF, new conservation laws do affect the DSF. By including momentum conservation into the collisions a peak emerges near the ion plasmon frequency.

Table 3.2 Tabulated plasma parameters for contaminated light species plasmas at three different levels of contamination: 1 carbon atom per $10^5, 10^4, 10^3$ light species atoms. Tabulated plasma parameters are computed in the same way as in Table. 3.1

Carbon contaminated light species plasma

η	species	n (1/cc)	Z	Γ	$\tilde{\kappa}$	$\nu_{i=j}$ (1/s)	$\nu_{i\neq j}$ (1/s)
10^5	L	4.08e+25	0.941	0.223	1.151	8.48e-03	3.20e-07
	C	4.08e+20	4.880	0.075	1.151	3.20e-02	1.71e-06
10^4	L	4.08e+25	0.941	0.223	1.152	8.48e-03	3.20e-06
	C	4.08e+21	4.880	0.161	1.152	3.20e-02	1.71e-05
10^3	L	4.06e+25	0.941	0.222	1.155	8.43e-03	3.18e-05
	C	4.06e+22	4.880	0.345	1.155	3.18e-02	1.69e-04

In the second case, we use the light species approximation for D and T and introduce C; this is formulated as

$$\rho = m_L n_L + m_C n_C. \tag{3.42}$$

We assume equal amounts of deuterium and tritium and consider a 1 part carbon per η parts light (*i.e.*, $n_C = n_L/\eta$) this determines the density

$$\rho = (m_L + m_C/\eta) n_L. \tag{3.43}$$

From this expression, we compute the number density and the other relevant contaminated plasma parameters, which we list in Table 3.2.

In Figure 3.5, the contaminated DT DSF are plotted. The pure light species, indicated by a black line, matches the pure light species from Figure 3.4. The colored lines represent increasing ratios of carbon to light species atoms. Notice, for the Mermin-like model that the carbon impurities drive the DSF to zero at $\omega = 0$. This is qualitatively different from the RPA and the completed Mermin models.

3.3.4 Conductivities

Both optical conductivity experiments and Kubo-Greenwood conductivity estimates need a dynamical model to estimate the DC conductivity. When the Drude conductivity model fails to fit the dynamic conductivity estimates, there are few alternatives. The dynamical conductivity is

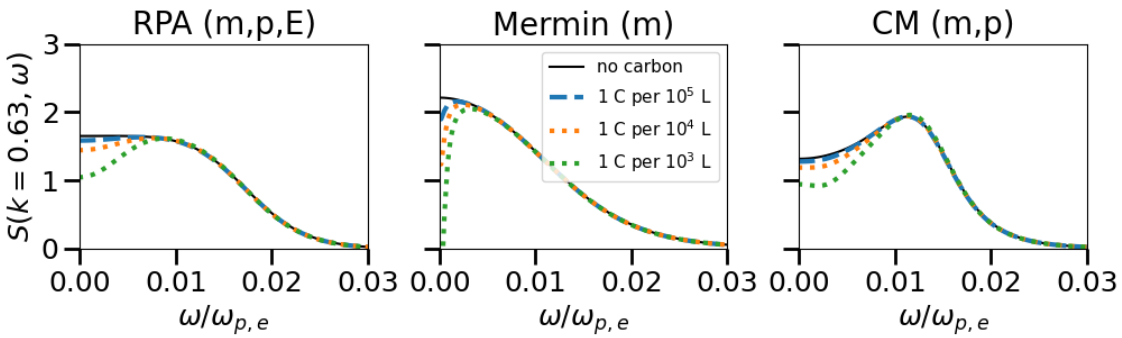

Figure 3.5 All plots compare $S(k, \omega)$ at fixed $k/k_{D,e} = .63$ across different DSF models. Each panel contains different carbon purity levels for a given multi-species DSF. The black line indicates a pure light species. The blue dashed line indicates 1 carbon particle per 10^5 light species particles. The orange dotted line indicates 1 carbon particle per 10^4 light species particles. The green dotted line indicates 1 carbon particle per 10^3 light species particles.

formally related to the dielectric function models via

$$\sigma(k, \omega) = \frac{i\omega}{4\pi} (1 - \varepsilon(k, \omega)) . \tag{3.44}$$

In this section, we will develop dielectric functions $\varepsilon(k, \omega)$ which uniquely determine a conductivity.

Using a Coulomb interaction for $v(k)$ and taking the long wavelength expansions of the completed Mermin dielectric function yields

$$\varepsilon_{\text{CM}}(\omega|a, b) = 1 - \frac{\omega_p^2}{\omega_\tau^2} \left(1 - ia\frac{1}{\omega_\tau \tau} + ib\frac{\omega\tau^{-1}}{\omega_\tau^2}\right)^{-1} . \tag{3.45}$$

We arrive at this expression using Eq(3.29) and Eq(3.34). Mermin's number conservation correction has been modified by $a \in [0, 1]$ to smoothly turn off ($a = 0$) and on ($a = 1$) the correction. Meanwhile, the momentum conservation correction, modified by $b \in [-1, 1]$, controls the degree of momentum reversal ($b = -1$) or conservation ($b = 1$) during a collision. The energy conservation corrections enter at order k^2, thus our completed Mermin and the Atwal-Ashcroft model predict the same expansion. It is reasonable to vary these conservation laws for a single species. This accounts for electron recombination events, which violate number conservation, and phonon scattering events, which violate momentum and energy conservation.

Using Eq(3.45) and Eq(3.44) we produce a new first-principles conductivity model. In Figure 3.6, we revisit Chen et al.'s Drude fit ($a = 1$, $b = 0$) to 300K gold data [7] and study the effects

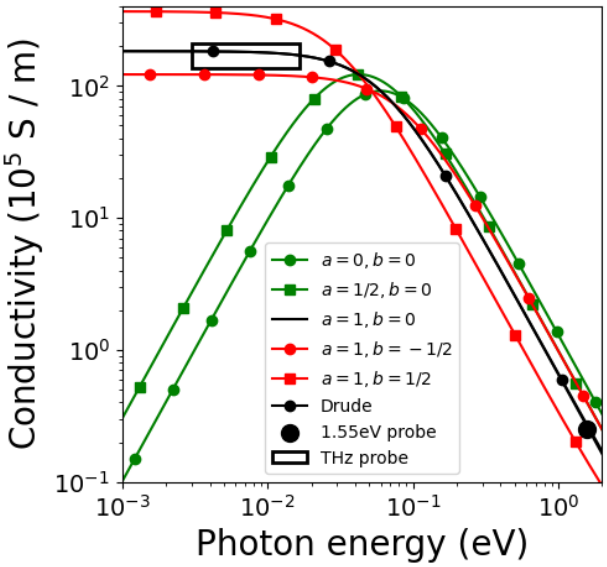

Figure 3.6 We have plotted the real part of the conductivity σ_r to demonstrate how number conservation violation ($a < 1$, plotted as green lines) and momentum preservation ($b \neq 0$, plotted as red lines) affect Chen et al.'s Drude conductivity fit (plotted as a solid black line) [7].

of parameters a and b on the shape of the conductivity model. The central black line expresses their Drude fit. If particle number is not conserved ($a < 1$), then relative to the Drude model, the DC conductivity is suppressed and the optical conductivity is enhanced. Thus, the number conservation term primarily affects the model's slope at lower frequencies. Whereas, if particle momentum is partially conserved ($b = 1/2$), then, relative to the Drude model, the DC conductivity is enhanced and the optical conductivity is suppressed. Oppositely, if the collision reverses the momentum of a particle ($b = -1/2$), then the DC conductivity is suppressed and the optical conductivity is enhanced. In total, the momentum conservation term primarily enhances or suppresses the DC conductivity, but does not change the slope in the low frequency region.

Lastly, our first-principles model can be compared to the primary alternative to the Drude model. The Drude-Smith (DS) conductivity model is defined as

$$\sigma(\omega) = \frac{\sigma_0}{1 - i\omega\tau}\left(1 + \frac{\beta_1}{1 - i\omega\tau}\right). \tag{3.46}$$

Using Eq(3.44), the Drude-Smith (DS) dielectric function is given by

$$\varepsilon_{\mathrm{DS}}(\omega|\beta_1) = 1 - \frac{\omega_p^2}{\omega_\tau^2}\left(\frac{\omega_\tau + i\beta_1/\tau}{\omega}\right). \tag{3.47}$$

Comparing Smith's model Eq(3.47) to our model Eq(3.45), we see that for $b = 0$ (*i.e.*, momentum conservation is turned off), there is a direct relationship between our number conservation, a, and Smith's β_1. This relation is expressed as,

$$\left(\frac{\omega_\tau - ia/\tau}{\omega_\tau}\right)^{-1} = \left(\frac{\omega_\tau + i\beta_1/\tau}{\omega}\right). \tag{3.48}$$

Notice Mermin's model and Smith model are equivalent when number is conserved (*i.e.*, $a = 1$) and Smith's parameter is fully off (*i.e.*, $\beta_1 = 0$). Further, Mermin's model and Smith's model are equivalent when number is not conserved (*i.e.*, $a = 0$) and Smith's parameter is fully on (*i.e.*, $\beta_1 = -1$). This suggests Smith's model breaks local number conservation to achieve DC conductivity suppression.

3.4 Summary and Outlook

In this chapter, we introduce a new first-principles dynamical response model to address demands in XRTS diagnostics, conductivity estimates, and radiation hydrodynamics codes. This model, named the completed Mermin susceptibility, is the first to conserve both number and momentum locally across multiple species. This extends the work of Selchow et al. [22] and Atwal and Ashcroft [20], expanding their single-species BGK approach to encompass multi-species systems. Moreover, as a validation of our approach, we recover the multi-species Mermin susceptibility [26] in a specific limiting case.

We showed numerical and analytic calculations of the f-sum rule and screening sum rule, which emphasize our completed Mermin satisfies both sum rules. The momentum conservation correction results in an infinitesimal plasmon peak at the long wavelength limit, indicating plasmons as the sole energy loss mechanism. We argue that the violation of Mermin's f-sum rule stems from his continuity equation not assuming $\delta\mathbf{j} = n_0\delta\mathbf{u}$. Comparatively, the momentum collisional invariant enforces this assumption. In the single species limit, our momentum conservation correction matches the local field correction derived in Morawetz and Fuhrmann [21].

We produced the two-component completed Mermin ion-ion DSF and applied the model to a plasma of deuterium and tritium at ICF hot spot conditions. Comparing the completed Mermin

DSF to the Mermin and RPA DSFs, we showed that conservation of momentum produces a peak near the ion plasma frequency not present in the Mermin and RPA models. This suggests that ion-phonon scattering is an important energy loss mechanism in the warm dense matter regime. We also demonstrate that the light species approximation qualitatively agrees with both mixed and unmixed deuterium and tritium plasmas. Using the light species approximation, we discovered that carbon contamination affects the Mermin DT DSF in a qualitatively different way than either the RPA and the completed Mermin DSF. To make direct comparisons to experiments, we must next develop appropriate dynamical inter-species collision frequencies $\tau_{ij}(\omega)$ and effective ion-ion interaction potentials $v_{ij}(k)$.

Finally, we applied our completed Mermin conductivity model to dynamical gold conductivity measurements. We show that both number and momentum conservation suppress DC conductivity, albeit through distinct mechanisms. Therefore, our completed Mermin conductivity model provides a first-principles alternative to the semi-empirical Drude-Smith conductivity model. By comparing the two models, we showed that the Drude-Smith model violates local number conservation to suppress DC conductivity. We interpret the violation of local number conservation as the removal of free charge carriers. IIn this regard, our results support Cocker et al. [14], who demonstrated that charge carrier confinement can account for Smith's phenomenological correction. Our new interpretation of Smith's phenomenological parameter β_1 contradicts Smith's own claim that β_1 accounts for back scattering. Considering the relevant conservation laws, we conclude that the completed Mermin conductivity model [Eq(3.45)] can incorporate back scattering by setting parameters $a = 1$ (activating number conservation) and $b \in [-1, 0]$ (indicating momentum reversal during collisions).

APPENDIX 3A

FOURIER TRANSFORMING OUR KINETIC EQUATION

In this appendix, we expand, linearize, and Fourier transform our multi-species BGK kinetic equation. First, we list our chosen Fourier conventions. We choose

$$\delta f_{iG}(\mathbf{r}, \mathbf{v}, \omega) = \int dt\ e^{i\omega t} \delta f_{iG}(\mathbf{r}, \mathbf{v}, t)$$

as the temporal convention, so that

$$\int dt\ e^{i\omega t}\ \partial_t\ \delta f_{iG}(\mathbf{r}, \mathbf{v}, t) = -i\omega\ \delta f(\mathbf{r}, \mathbf{v}, \omega) \tag{3A.1}$$

and

$$\delta f(\mathbf{k}, \mathbf{v}, t) = \int d\mathbf{r}\ e^{-i\mathbf{k}\cdot\mathbf{r}} \delta f_{iG}(\mathbf{r}, \mathbf{v}, t) \tag{3A.2}$$

as our spatial convention, so that

$$\int d\mathbf{r}\ e^{-i\mathbf{k}\cdot\mathbf{r}}\ \nabla_{\mathbf{r}} \delta f_{iG}(\mathbf{r}, \mathbf{v}, t) = i\mathbf{k}\ \delta f_{iG}(\mathbf{k}, \mathbf{v}, t). \tag{3A.3}$$

This means that the usual expression for force

$$m_i \mathbf{a}_i^{\text{tot}}(\mathbf{r}, t) = -\nabla_{\mathbf{r}} U_i^{\text{tot}}(\mathbf{r}, t) \tag{3A.4}$$

results in

$$\mathbf{a}_i^{\text{tot}}(\mathbf{k}, \omega) = -m_i^{-1} i\mathbf{k} U_i^{\text{tot}}(\mathbf{k}, \omega). \tag{3A.5}$$

We now proceed to derive Eq(3.14) from Eq(3.1). For convenience, we reproduce Eq(3.1)

$$\left(\partial_t + \mathbf{v} \cdot \nabla_{\mathbf{r}} + \mathbf{a}_i^{\text{tot}} \cdot \nabla_{\mathbf{v}}\right) f_i(\mathbf{r}, \mathbf{v}, t) = \sum_j Q_{ij}. \tag{3.1'}$$

We insert expansions Eq(3.8) and Eq(3.9), and then Fourier transform using the specified conventions. The result is

$$\begin{aligned}
&(\mathbf{v} \cdot k - \omega)\ \lambda \delta f_{iG}(\mathbf{k}, \mathbf{v}, \omega) \\
&- \lambda \int d\mathbf{k}' d\omega'\ m_i^{-1}(\mathbf{k} - \mathbf{k}') \cdot \nabla_{\mathbf{v}}\ (f_{iG}(\mathbf{v}) \delta(k') \delta(\omega') + \delta f_{iG}(\mathbf{k}, \mathbf{v}, \omega))\ U_i^{\text{tot}}(\mathbf{k}, \omega) \\
&= \sum_j \frac{i\lambda}{\tau_{ij}} \delta f_{iG}(\mathbf{k}, \mathbf{v}, \omega) - \sum_j \frac{i\lambda}{\tau_{ij}} \delta M_{ij}(\mathbf{r}, \mathbf{v}, t).
\end{aligned} \tag{3A.6}$$

Note the second term on the LHS of Eq(3A.6) is a convolution, this term arises from $\mathbf{a}_i^{\text{tot}} \cdot \nabla_{\mathbf{v}} f_i(\mathbf{r}, \mathbf{v}, t)$ since both terms are position and time dependent. As part of the linearization process, we replaced $f_i(\mathbf{r}, \mathbf{v}, t)$ with its expansion about global equilibrium $f_{iG}(v)$. Since $f_{iG}(v)$ does not have position and time dependence, it is treated as a constant and its Fourier transform acquires Dirac delta functions. From Eq(3A.6), we drop $\delta f_{iF}^M \, U_i^{\text{tot}}$ since it is second order and evaluate the convolution. The simplified expression is

$$\begin{aligned}
&(\mathbf{v} \cdot k - \omega) \, \lambda_i \delta f_{iG}(\mathbf{k}, \mathbf{v}, \omega) - \lambda_i \, m_i^{-1} \mathbf{k} \cdot \nabla_{\mathbf{v}} f_{iG}(\mathbf{v}) \, U_i^{\text{tot}}(\mathbf{k}, \omega) \\
&= \sum_j \frac{i\lambda_i}{\tau_{ij}} \delta f_{iG}(\mathbf{k}, \mathbf{v}, \omega) - \sum_j \frac{i\lambda_i}{\tau_{ij}} \delta M_{ij}(\mathbf{r}, \mathbf{v}, t).
\end{aligned} \tag{3A.7}$$

Canceling the fugacity factors and grouping the $\delta f_{iG}(\mathbf{k}, \mathbf{v}, \omega)$ terms, we arrive at our desired result Eq(3.14).

APPENDIX 3B

EVALUATING THE MOMENTUM CONSERVATION CONSTRAINT

In this appendix, we show how to produce the momentum constraint, Eq(3.21b), from the first moment of the collision operator, Eq(3.19b). For convenience we reproduce Eq(3.19b)

$$\int d\mathbf{v}\, m_i \mathbf{v} Q_{ij} + \int d\mathbf{v}\, m_j \mathbf{v} Q_{ji} = 0. \tag{3.19b'}$$

Using the definition of Q_{ij} from Eq(3.4) and the expansions from Eq(3.8) and Eq(3.9), we obtain the expanded form of the collision operator as

$$Q_{ij} \approx \frac{\lambda_i}{\tau_{ij}} \left(\delta M_{ij} - \delta f_{iG} \right). \tag{3B.1}$$

After inserting Eq(3B.1) into the momentum constraint, canceling the fugacities, and grouping terms, we produce

$$\int d\mathbf{v}\, \mathbf{v} \left(m_i \frac{\delta M_{ij}}{\tau_{ij}} + m_j \frac{\delta M_{ji}}{\tau_{ji}} \right) = \int d\mathbf{v}\, \mathbf{v} \left(m_i \frac{\delta f_{iG}}{\tau_{ij}} + m_j \frac{\delta f_{jG}}{\tau_{ji}} \right). \tag{3B.2}$$

We insert the linear expansion for δM_{ij}, Eq(3.17), on the LHS and omit terms that are odd powers of $\mathbf{v}$ (Gaussian integrals evaluate to zero). The momentum constraint becomes

$$\frac{m_i}{\tau_{ij}} \int d\mathbf{v}\, \mathbf{v} \frac{m_i^{-1} \mathbf{k} \cdot \nabla_{\mathbf{v}} f_{iG}}{\mathbf{v} \cdot \mathbf{k}} \mathbf{p}_i \cdot \delta \mathbf{u} + \frac{m_j}{\tau_{ji}} \int d\mathbf{v}\, \mathbf{v} \frac{m_j^{-1} \mathbf{k} \cdot \nabla_{\mathbf{v}} f_{jG}}{\mathbf{v} \cdot \mathbf{k}} \mathbf{p}_j \cdot \delta \mathbf{u} = \frac{m_i \delta \mathbf{j}_i}{\tau_{ij}} + \frac{m_j \delta \mathbf{j}_j}{\tau_{ji}}. \tag{3B.3}$$

To simplify the RHS, we used $\delta \mathbf{j}_i \equiv \int d\mathbf{v}\, \mathbf{v} \delta f_{iG}$. Evaluating the LHS integrals yields Eq(3.21b).

APPENDIX 3C

EXPANDING PARTIAL FRACTIONS

In this appendix, we integrate over velocity to produce the system's linearized dynamical response. We reproduce Eq(3.18) for the reader's convenience,

$$\delta f_{iG}(\mathbf{k},\mathbf{v},\omega) = \frac{m_i^{-1}\,\mathbf{k}\cdot\nabla_{\mathbf{v}} f_{iG}(v)}{\mathbf{v}\cdot\mathbf{k}-\omega_{\tau_i}} \times\left(U_{tot}+\frac{i}{\mathbf{v}\cdot\mathbf{k}}\sum_j\frac{1}{\tau_{ij}}\left(\delta\mu_i+\mathbf{p}_i\cdot\delta\mathbf{u}_{ij}+\left(\frac{p_i^2}{2m_i}-\mu_i\right)\frac{\delta T_{ij}}{T}\right)\right). \tag{3.18'}$$

The zeroth moment of Eq(3.18) is is given by

$$\delta n = U_{\rm tot}P\left[\mathbf{v}\cdot\mathbf{k}\right]+\frac{i}{\tau_i}P\left[1\right]\delta\mu_i+\sum_j\frac{i}{\tau_{ij}}P\left[\mathbf{p}_i\cdot\delta\mathbf{u}\right]+\sum_j\frac{i}{\tau_{ij}}\left(P\left[\frac{p_i^2}{2m_i}\right]-\mu_i P\left[1\right]\right)\frac{\delta T_{ij}}{T}. \tag{3C.1}$$

The linear functional P is defined

$$P\left[g\right]\equiv\int d\mathbf{v}\frac{m_i^{-1}\mathbf{k}\cdot\nabla_{\mathbf{v}}f_{iG}}{\mathbf{v}\cdot\mathbf{k}\left(\mathbf{v}\cdot\mathbf{k}-\omega_{\tau_i}\right)}g. \tag{3C.2}$$

This results in the following functionals

$$P\left[p_i^{2n}(\mathbf{v}\cdot\mathbf{k})\right]=C_{i,2n}^M, \tag{3C.3a}$$

$$P\left[p_i^{2n}(\mathbf{v}\cdot\mathbf{k}-\omega_\tau)\right]=B_{i,2n}^M, \tag{3C.3b}$$

$$P\left[\left(\frac{p_i^2}{2m_i}\right)^n\right]=\frac{1}{\omega_\tau}\left(\frac{C_{2n}^M}{(2m_i)^n}-\frac{B_{2n}^M}{(2m_i)^n}\right), \tag{3C.3c}$$

$$P\left[\mathbf{p}_i\cdot\delta\mathbf{u}\right]=\frac{m_i}{k^2}\,C_{i,0}^M\,\mathbf{k}\cdot\delta\mathbf{u}. \tag{3C.3d}$$

Note that, for $n=0$, Eq(3C.3c) simplifies to $P\left[1\right]$. By substituting these expressions of the functional P into Eq(3C.1), we obtain Eq(3.24), as claimed.

APPENDIX 3D

IMPLEMENTING OUR MODEL

In this appendix, we collect the information necessary to compute the multi-species completed Mermin susceptibilty.

Expressing $C_{i,2n}$ with Dimensional Quantities

The completed Mermin susceptibilty has been expressed in terms of $C_{2n}(\mathbf{k},\omega)$. Thus, our first step is create a dimensional version of this expression for $n = 0, 2, 4$. We reproduce Eq(3.22a) here for the reader's convenience

$$C^M_{i,n}(\mathbf{k},\omega) \equiv \int d\mathbf{v}|\mathbf{p}|^n \frac{m_i^{-1}\mathbf{k}\cdot\nabla_{\mathbf{v}} f_{iG}}{\mathbf{v}\cdot\mathbf{k}-\omega}. \tag{3.22a'}$$

In the absence of an external magnetic field, the x axis is arbitrarily chosen as the direction of the wave vector (*i.e.* $\mathbf{v}\cdot\mathbf{v} = v_x^2$ and $\mathbf{v}\cdot\mathbf{k} = v_x k_x$). We insert $\nabla_{\mathbf{v}} f_{iG}$ and evaluate the v_y, v_z integrals. This recasts our function as

$$C_{i,2n} = -\frac{n_i}{T}(m_i T)^n \left(\frac{1}{2\pi}\right)^{1/2} \int_C d\tilde{v}\ \tilde{v}^{2n} \frac{\tilde{v} e^{-\tilde{v}^2/2}}{\tilde{v} - \sqrt{\frac{m_i}{T}}\frac{\omega_\tau}{k_x}}. \tag{3D.1}$$

Here $\tilde{v} = \sqrt{\frac{m_i}{T}} v_x$ is the dimensionless velocity. We can express the term in the denominator in relation to the electron's dimensionless phase velocity

$$\sqrt{\frac{m_i}{T}}\frac{\omega_\tau}{k_x} = \zeta_i \tilde{v}_p. \tag{3D.2}$$

This equality follows from the definitions of the electron plasma frequency $\omega_{p,e}^2 \equiv 4\pi n_e\ e^2/m_e$, the electron Debye wavenumber $k_{D,e}^2 \equiv 4\pi n_e\ e^2/T$, the mass fraction $\zeta_i \equiv \sqrt{m_i/m_e}$, and the dimensionless phase velocity $\tilde{v}_p \equiv \frac{\omega_\tau/\omega_{p,e}}{k_x/k_{D,e}}$. We use the electron based normalization to make the multi-species calculations simpler. The final dimensionless expression of $C_{i,2n}$ is,

$$C_{i,2n}(k,\omega_\tau) = -\frac{n_i}{T}(m_i T)^n F_{2n}(\zeta_i \tilde{v}_p), \tag{3D.3a}$$

$$B_{i,2n} \equiv C_{i,0}(k,0) \tag{3D.3b}$$

$$F_{2n}(z) = \left(\frac{1}{2\pi}\right)^{1/2} \int_C d\tilde{v}\ \tilde{v}^{2n} \frac{\tilde{v}}{\tilde{v}-z}. \tag{3D.3c}$$

For the reader's convenience, we note that $B_{i,0} = -\frac{n_i}{T}$, $B_{i,2} = -\frac{n_i}{T} m_i T$, and $B_{i,4} = -3\frac{n_i}{T}(m_i T)^2$; this can be computed considering the $z \to 0$ limit.

Expressing χ with Dimensionless Quantities

Our next step is to propagate these expressions for $C_{i,2n}$ and $B_{i,2n}$ into the completed Mermin susceptibility Eq(3.27). Consider the modified dielectric function

$$\begin{aligned}\varepsilon_1^* = 1 - v_{11}(k) C_{1,0}^M - \frac{i}{\omega_{\tau_1}\tau_1}\left(1 - \frac{C_{1,0}^M}{B_{1,0}^M}\right) \\ - i\frac{\omega}{k^2}\left(\frac{m_1}{n_{1,0}\tau_{11}} + \frac{\tau_{21}}{\tau_{12}}\frac{m_1^2}{m_1 n_{0,1}\tau_{21} + m_2 n_{0,2}\tau_{12}}\right) C_{1,0}^M.\end{aligned} \tag{3D.4}$$

Substituting $C_{i,2n}$ and $B_{i,2n}$ from Eq(3D.3) and $m_i/T = \zeta_i^2 k_{D,e}^2/\omega_{D,e}^2$, we can recast the modified dielectric function as

$$\begin{aligned}\varepsilon_1^* = 1 - v_{11}(k) C_{1,0}^M - \frac{i}{\omega_{\tau_1}\tau_1}\left(1 - F_0(\zeta_1 \tilde{v}_p)\right) \\ + \left(i\frac{\zeta_1^2\omega}{k^2\tau_{11}}\frac{k_{D,e}^2}{\omega_{p,e}^2} + i\frac{\omega}{k^2}\,\frac{\tau_{21}}{\tau_{12}}\frac{\psi_1^2\zeta_1^4}{\zeta_1^2\psi_1^2\tau_{21} + \zeta_2^2\psi_2^2\tau_{12}}\frac{k_{D,e}^2}{\omega_{p,e}^2}\right) F_0(\zeta_1\tilde{v}_p).\end{aligned} \tag{3D.5}$$

We normalized our parameters to electronic scales $\tilde{k} = k/k_{D,e}$, $\tilde{\tau} = \tau\omega_{p,e}$, $\tilde{\omega} = \omega/\omega_{p,e}$, and $\tilde{\omega}_{\tau_1} = \omega_{\tau_1}/\omega_{p,e}$. The result is

$$\varepsilon_1^* = 1 - v_{11}(k) C_{1,0}^M - \frac{i}{\tilde{\omega}_{\tau_1}\tilde{\tau}_1}(1 - F_0) + \left(i\frac{\zeta_1^2\tilde{\omega}}{\tilde{k}^2\tilde{\tau}_{11}} + i\frac{\tilde{\omega}}{\tilde{k}^2}\,\frac{\tilde{\tau}_{21}}{\tilde{\tau}_{12}}\frac{\psi_1^2\zeta_1^4}{\zeta_1^2\psi_1^2\tilde{\tau}_{21} + \zeta_2^2\psi_2^2\tilde{\tau}_{12}}\right) F_0, \tag{3D.6}$$

where we have suppressed the arguments in $F_0(\zeta_i\tilde{v}_p)$ for brevity.

Next, we non-dimensionalize $v_{11}(k)C_{1,0}^M$, in Eq(3D.6). To do this, we assume that $v_{ij}(k)$ is the screeened Coulomb interaction

$$v_{ij}(r) = \frac{Z_i Z_j e^2}{r} e^{-r/\lambda_s}. \tag{3D.7}$$

We group terms into a dimensionless parameters $\tilde{r} = k_{D,e} r$, $\tilde{\kappa} = (\lambda_s k_{D,e})^{-1}$ and Fourier transform over $\tilde{r}$ to arrive at

$$v_{ij}(k) = \frac{T}{n_e}\left(\frac{Z_i Z_j}{\tilde{k}^2 + \tilde{\kappa}^2}\right). \tag{3D.8}$$

Notice that if we let $\lambda_s^{-1} = k_{D,e}$, as is the case in Thomas-Fermi theory, then $\tilde{\kappa} = 1$. The factor of T/n_e will multiply $-n_i/T$ from the susceptibility and leave behind $-n_i/n_\mathrm{e} = -\psi_i^2$. Therefore the product is expressed

$$v_{ij}(k)C_{i,0}^M = -\psi_i^2 \left(\frac{Z_i Z_j}{\tilde{k}^2 + \tilde{\kappa}^2}\right) F_0. \tag{3D.9}$$

Inserting Eq(3D.9) into Eq(3D.6), yields the final expression for the modified dielectric function

$$\begin{aligned}\varepsilon_1^* = 1 &+ \psi_i^2 \left(\frac{Z_1^2}{\tilde{k}^2 + \tilde{\kappa}^2}\right) F_0(\zeta_1 \tilde{v}_p) - \frac{i}{\tilde{\omega}_{\tau_1}\tilde{\tau}_1}\left(1 - F_0(\zeta_1 \tilde{v}_p)\right) \\ &+ \left(i\frac{\zeta_1^2 \tilde{\omega}}{\tilde{k}^2 \tilde{\tau}_{11}} + i\frac{\tilde{\omega}}{\tilde{k}^2}\,\frac{\tilde{\tau}_{21}}{\tilde{\tau}_{12}}\frac{\psi_1^2 \zeta_1^4}{\zeta_1^2 \psi_1^2 \tilde{\tau}_{21} + \zeta_2^2 \psi_2^2 \tilde{\tau}_{12}}\right) F_0(\zeta_1 \tilde{v}_p).\end{aligned} \tag{3D.10}$$

The only remaining expression in Eq(3.27) is the momentum conservation coupling term. Following the same steps as above yields

$$\begin{aligned}&\left(v_{12}(k) + i\frac{\omega}{k^2}\frac{m_1 m_2}{m_1 n_1 \tau_{21} + m_2 n_2 \tau_{12}}\right) C_{1,0} \\ &\quad = -\left(\left(\frac{Z_1 Z_2}{\tilde{k}^2 + \tilde{\kappa}^2}\right) + i\frac{\tilde{\omega}}{k^2}\frac{\zeta_1^2 \zeta_2^2}{\zeta_1^2 \psi_1^2 \tilde{\tau}_{21} + \zeta_2^2 \psi_2^2 \tilde{\tau}_{12}}\right) \psi_1^2 F_0(\zeta_2 \tilde{v}_p).\end{aligned} \tag{3D.11}$$

Together Eq(3D.9), Eq(3D.10), and Eq(3D.11) provide a complete dimensionless representation of the completed Mermin susceptibilty Eq(3.27).

Representing F_{2n} with Special Functions

To evaluate Eq(3D.9), Eq(3D.10), and Eq(3D.11), we need numerical implementations of $F_0(z)$. Ichimaru Ch.4, expresses $F_0(z)$ in terms of the special function $W(Z)$ [6]. We extended Ichimaru's procedure to calculate $F_2(z)$ and $F_4(z)$. The resulting expressions are

$$F_0(z) = 1 + z\left(i\sqrt{\frac{\pi}{2}}\mathrm{WofZ}(z/\sqrt{2})\right), \tag{3D.12a}$$

$$F_2(z) = 1 + z^2 + z^3\left(i\sqrt{\frac{\pi}{2}}\mathrm{WofZ}(z/\sqrt{2})\right), \tag{3D.12b}$$

$$F_4(z) = 3 + z^2 + z^4 + z^5\left(i\sqrt{\frac{\pi}{2}}\mathrm{WofZ}(z/\sqrt{2})\right), \tag{3D.12c}$$

$$\mathrm{WofZ}(\frac{z}{\sqrt{2}}) \equiv i\sqrt{\frac{2}{\pi}}e^{-z^2/2}\int_0^z d\tilde{v}e^{\tilde{v}^2/2} + e^{-z^2/2}. \tag{3D.12d}$$

We denote $W(z)$ as $\mathrm{WofZ}(z)$ to align with scipy's notation. The only remaining unknowns are the parameters which describe our plasma system: ψ_i, ζ_i, Z_i, $\tilde{\kappa}$, ν_{ij}.

APPENDIX 3E

EXPANDING THE DIELECTRIC FUNCTION AT LONG WAVELENGTHS

In this appendix, we compute the long wave expansions presented in Eq(3.37). For single species, Eq(3.34) informs us that

$$\frac{1}{\varepsilon(k,\omega)} = v(k)\chi(k,\omega). \tag{3E.1}$$

Here χ is the mean field corrected susceptibility. We rewrite Eq(3.34) in terms of susceptibilities without mean field corrections (*i.e.*, $\chi = \chi_0/(1 - v(k)\chi_0)$) as

$$\frac{1}{\varepsilon(k,\omega)} = \frac{v(k)\chi_0}{1 - v(k)\chi_0}. \tag{3E.2}$$

We will use Eq(3E.2) to compute the long wave expansions presented in Eq(3.37).

Starting from Mermin Eq(3.30), completed Mermin Eq(3.29), and Atwal-Ashcroft [20], we follow the same steps as Appendix 3D to produce non-dimensional representations of the single species susceptibilities *without* mean field correction. These expressions are

$$\tilde{\chi}_0^M \equiv \frac{-F_0}{\frac{\tilde{\omega}}{\tilde{\omega}_\tau} + \frac{i}{\tilde{\tau}\tilde{\omega}_\tau}F_0}, \tag{3E.3a}$$

$$\tilde{\chi}_0^{CM} \equiv \frac{-F_0}{\frac{\tilde{\omega}}{\tilde{\omega}_\tau} + i\left(\frac{1}{\tilde{\tau}\tilde{\omega}_\tau} + \frac{\zeta_i^2\tilde{\omega}}{\tilde{k}^2\tilde{\tau}}\right)F_0}, \tag{3E.3b}$$

$$\tilde{\chi}_0^{AA} \equiv \frac{-F_0 + \frac{i}{2\tilde{\tau}\tilde{\omega}}\left(F_2F_2 - F_0F_4\right)}{\frac{\tilde{\omega}}{\tilde{\omega}_\tau} + \frac{i\zeta_i^2\tilde{\omega}}{k^2\tilde{\tau}}F_0 + \left(\frac{1}{2\tilde{\omega}\tilde{\omega}_\tau\tilde{\tau}^2} + \frac{\zeta_i^2}{2\tilde{\tau}^2\tilde{k}^2}\right)\left(F_2F_2 - F_0F_4\right) + \frac{i}{2\tilde{\tau}\tilde{\omega}_\tau}\left(3F_0 - 2F_2 + F_4\right)}, \tag{3E.3c}$$

where we have normalized our parameters to electronic scales: $\zeta_i^2 = m_i/m_e$, $\tilde{k} = k/k_{D,e}$, $\tilde{\tau} = \tau\omega_{p,e}$, $\tilde{\omega} = \omega/\omega_{p,e}$, and $\tilde{\omega}_\tau = \omega_\tau/\omega_{p,e}$. Additionally, we have suppressed the dependence of $F_0(\zeta_i\tilde{v}_p)$, $F_2(\zeta_i\tilde{v}_p)$, and $F_4(\zeta_i\tilde{v}_p)$.

As shown in Appendix 3D, $F_0(z)$, $F_2(z)$, and $F_4(z)$ can be expressed in terms of the WofZ function, which has known $z \to \infty$ expansions. Expanding $F_0(z)$, $F_2(z)$, and $F_4(z)$ at large z yields

the following analytic expressions:

$$\lim_{z\to\infty} F_0(z) = -1/z^2 + O[z^{-4}], \tag{3E.4a}$$

$$\lim_{z\to\infty} F_2(z) = -3/z^2 + O[z^{-4}], \tag{3E.4b}$$

$$\lim_{z\to\infty} F_4(z) = -15/z^2 + O[z^{-4}]. \tag{3E.4c}$$

To construct Eq(3.37), we first substitute Eq(3E.4) into the susceptibilities Eq(3E.3) and then we substitute the susceptibilities into Eq(3E.2).

BIBLIOGRAPHY

[1] Siegfried H. Glenzer and Ronald Redmer. X-ray thomson scattering in high energy density plasmas. *Rev. Mod. Phys.*, 81:1625–1663, Dec 2009.

[2] Frank Graziani, Michael P Desjarlais, Ronald Redmer, and Samuel B Trickey. *Frontiers and challenges in warm dense matter*, volume 96. Springer Science & Business, 2014.

[3] Peter M. Celliers, Marius Millot, Stephanie Brygoo, R. Stewart McWilliams, Dayne E. Fratanduono, J. Ryan Rygg, Alexander F. Goncharov, Paul Loubeyre, Jon H. Eggert, J. Luc Peterson, Nathan B. Meezan, Sebastien Le Pape, Gilbert W. Collins, Raymond Jeanloz, and Russell J. Hemley. Insulator-metal transition in dense fluid deuterium. *Science*, 361(6403):677–682, 2018.

[4] Monica Pozzo, Michael P. Desjarlais, and Dario Alfè. Electrical and thermal conductivity of liquid sodium from first-principles calculations. *Phys. Rev. B*, 84:054203, Aug 2011.

[5] James F Ziegler, Matthias D Ziegler, and Jochen P Biersack. Srim–the stopping and range of ions in matter (2010). *Nuclear Instruments and Methods in Physics Research Section B: Beam Interactions with Materials and Atoms*, 268(11-12):1818–1823, 2010.

[6] Setsuo Ichimaru. *Statistical Plasma Physics, Vol1: Basic Principles*. CRC Press, 1991.

[7] Zhijiang Chen, CB Curry, R Zhang, F Treffert, N Stojanovic, S Toleikis, R Pan, M Gauthier, E Zapolnova, LE Seipp, et al. Ultrafast multi-cycle terahertz measurements of the electrical conductivity in strongly excited solids. *Nature communications*, 12(1):1638, 2021.

[8] James Lloyd-Hughes and Tae-In Jeon. A review of the terahertz conductivity of bulk and nano-materials. *Journal of Infrared, Millimeter, and Terahertz Waves*, 33:871–925, 2012.

[9] Petr Kuzel and Hynek Nemec. Terahertz spectroscopy of nanomaterials: a close look at charge-carrier transport. *Advanced Optical Materials*, 8(3):1900623, 2020.

[10] N.V. Smith. Drude theory and the optical properties of liquid mercury. *Physics Letters A*, 26(3):126–127, 1968.

[11] Hynek Nemec, Petr Kuzel, and Villy Sundstrom. Far-infrared response of free charge carriers localized in semiconductor nanoparticles. *Phys. Rev. B*, 79:115309, Mar 2009.

[12] Koichi Shimakawa and Safa Kasap. Dynamics of carrier transport in nanoscale materials: Origin of non-drude behavior in the terahertz frequency range. *Applied Sciences*, 6(2):50, 2016.

[13] N. V. Smith. Classical generalization of the drude formula for the optical conductivity. *Phys. Rev. B*, 64:155106, Sep 2001.

[14] T. L. Cocker, D. Baillie, M. Buruma, L. V. Titova, R. D. Sydora, F. Marsiglio, and F. A. Hegmann. Microscopic origin of the drude-smith model. *Phys. Rev. B*, 96:205439, Nov 2017.

[15] N. D. Mermin. Lindhard dielectric function in the relaxation-time approximation. *Phys. Rev. B*, 1:2362–2363, Mar 1970.

[16] KU Plagemann, P Sperling, R Thiele, MP Desjarlais, C Fortmann, T Döppner, HJ Lee, Siegfried H Glenzer, and R Redmer. Dynamic structure factor in warm dense beryllium. *New Journal of Physics*, 14(5):055020, 2012.

[17] P. Sperling, E. J. Gamboa, H. J. Lee, H. K. Chung, E. Galtier, Y. Omarbakiyeva, H. Reinholz, G. Röpke, U. Zastrau, J. Hastings, L. B. Fletcher, and S. H. Glenzer. Free-electron x-ray laser measurements of collisional-damped plasmons in isochorically heated warm dense matter. *Phys. Rev. Lett.*, 115:115001, Sep 2015.

[18] B. B. L. Witte, L. B. Fletcher, E. Galtier, E. Gamboa, H. J. Lee, U. Zastrau, R. Redmer, S. H. Glenzer, and P. Sperling. Warm dense matter demonstrating non-drude conductivity from observations of nonlinear plasmon damping. *Phys. Rev. Lett.*, 118:225001, May 2017.

[19] Thomas W Hentschel, Alina Kononov, Alexandra Olmstead, Attila Cangi, Andrew D Baczewski, and Stephanie B Hansen. Improving dynamic collision frequencies: Impacts on dynamic structure factors and stopping powers in warm dense matter. *Physics of Plasmas*, 30(6), 2023.

[20] G. S. Atwal and N. W. Ashcroft. Relaxation of an electron system: Conserving approximation. *Phys. Rev. B*, 65:115109, Feb 2002.

[21] Klaus Morawetz and Uwe Fuhrmann. Momentum conservation and local field corrections for the response of interacting fermi gases. *Phys. Rev. E*, 62:4382–4385, Sep 2000.

[22] A. Selchow and K. Morawetz. Dielectric properties of interacting storage ring plasmas. *Phys. Rev. E*, 59:1015–1023, Jan 1999.

[23] P. L. Bhatnagar, E. P. Gross, and M. Krook. A model for collision processes in gases. i. small amplitude processes in charged and neutral one-component systems. *Phys. Rev.*, 94:511–525, May 1954.

[24] Adriaan Daniël Fokker. Die mittlere energie rotierender elektrischer dipole im strahlungsfeld. *Annalen der Physik*, 348(5):810–820, 1914.

[25] VM Planck. Über einen satz der statistischen dynamik und seine erweiterung in der quantentheorie. *Sitzungberichte der*, 1917.

[26] A. Selchow, G. Röpke, A. Wierling, H. Reinholz, T. Pschiwul, and G. Zwicknagel. Dynamic structure factor for a two-component model plasma. *Phys. Rev. E*, 64:056410, Oct 2001.

[27] Jeffrey R. Haack, Cory D. Hauck, and Michael S. Murillo. A conservative, entropic multispecies bgk model. *Journal of Statistical Physics*, 168:826–856, 2017.

[28] CR Weber, DS Clark, A Pak, N Alfonso, B Bachmann, LF Berzak Hopkins, T Bunn, J Crippen, L Divol, T Dittrich, et al. Mixing in icf implosions on the national ignition facility caused by the fill-tube. *Physics of Plasmas*, 27(3):032703, 2020.

[29] G. Röpke, A. Selchow, A. Wierling, and H. Reinholz. Lindhard dielectric function in the relaxation-time approximation and generalized linear response theory. *Physics Letters A*, 260(5):365–369, 1999.

[30] A Selchow, G Röpke, and A Wierling. Extended mermin-like dielectric function for a two-component plasma. *Contributions to Plasma Physics*, 42(1):43–54, 2002.

[31] Jean Pierre Boon and Sidney Yip. *Molecular hydrodynamics*. Courier Corporation, 1991.

[32] Jean-Pierre Hansen and Ian Ranald McDonald. *Theory of simple liquids: with applications to soft matter*. Academic press, 2013.

[33] S. X. Hu, B. Militzer, V. N. Goncharov, and S. Skupsky. Strong coupling and degeneracy effects in inertial confinement fusion implosions. *Phys. Rev. Lett.*, 104:235003, Jun 2010.

[34] RM More. Pressure ionization, resonances, and the continuity of bound and free states. In *Advances in atomic and molecular physics*, volume 21, pages 305–356. Elsevier, 1985.

[35] Liam G. Stanton and Michael S. Murillo. Ionic transport in high-energy-density matter. *Phys. Rev. E*, 93:043203, Apr 2016.

CHAPTER 4

MULTI-SPECIES KINETIC-FLUID COUPLING FOR HIGH-ENERGY DENSITY SIMULATIONS

4.1 Introduction

Material flows with long mean free paths (*i.e.* high Knudsen numbers), also known as kinetic flows, occur in plasmas, neutron and radiation transport, and dilute gases. Their evolution is often described by equations which are prohibitively difficult to solve numerically. However, if the Knudsen number is small enough, moment-based, i.e. hydrodynamic, models are applicable. These contain fewer degrees of freedom and thereby greatly reduce the computational cost. For many applications, such as interfaces and shocks, the spatial region over which the material is kinetic is proportionately small, suggesting the usage of a fluid-kinetic hybrid model that locally utilizes both kinetic and hydrodynamic approaches. Such a model has been proposed, for example, by Degond et al. [1]. Their work introduced the concept of a buffer region, in which a convex combination of both models is computed. Subsequent works extended this method to include time-dependent buffer zones [2], as well as applying a micro-macro framework for coupling the equations [3, 4, 5, 6]. A more recent study [7] proposes an infinitely thin buffer region and the transitioning from one cell to another using flux matching. Degond's original method was developed for single charge-neutral particle species. Here, we generalize it to the case of mixtures with electric fields. While this approach can be used in a wide variety of applications, in this chapter, we apply it to a high-energy density physics (HEDP) problem, specifically an experiment in intertial confinement fusion (ICF) to study preheat mixing in separated reactants.

ICF experiments span a wide range of plasma conditions, with densities and temperatures that can vary over many orders of magnitude. In addition, materials can be composed of light and/or heavy ions (e.g. deuterium (D), tritium (T) and gold (Au), respectively) and change between strong to weak collisionality. These experiments are typically designed and analyzed by radiation hydrodynamics simulations which attempt to capture the multiphysics nature of HEDP matter. However, significant differences between simulations and experiments remain, with a number of

possible sources for these discrepancies. For example, in near-vacuum hohlraums, multi-material mixing beyond what is predicted by hydrodynamic instabilities has been attributed to kinetic effects [8], i.e., a breakdown in the underlying assumption that collision times and mean free paths are sufficiently small for a fluid description to apply. Some phenomena attributed to kinetic effects may be attributable to other radiation hydrodynamics features, e.g., a study by Pape et al. [9] that shows that a small amount of helium fill in the hohlraum can suppress interpenetration of the ablator and wall plasmas, and cross-beam energy transfer is the main driver of discrepancies with past modeling mismatches.

A kinetic description of multi-material mixing will impact predictions for several important processes in ICF experiments [8]. For example, a mixing layer can occur at material interfaces in the capsule, such as between the ablator and the DT ice as well as the DT ice and vapor. Material interdiffusion due to preheating may result in significantly different configurations when the main driving shock(s) arrive [10, 11], causing unwanted material injection into the hot spot. The sharpness of interfaces in ICF capsules implies that physical phenomena of large particle mean free paths might be relevant. Indeed, experiments on an Au-CDH interface on the Trident laser [12] have shown a superdiffusive evolution of the interface which is in line with kinetic trajectories of fast particles. Another mixing layer occurs when plasma that is ejected from the hohlraum wall intersects with ablated material from the capsule in the region crossed by the inner laser beams [13]. A kinetic description of this mixing layer would predict that the wall and capsule plasmas interpenetrate. However, this phenomenon cannot be captured in a single-species hydrodynamic code and the resulting density spike interferes with the propagation of the inner beams. Intermediate moment models [14] have shown that a mixing layer may be described by a hydrodynamic description in some configurations, and in fact laser-plasma interactions (e.g. CBET) are the culprit for asymmetric drive. This hybrid model or future adaptive versions could also be used to study the suppression of interpenetration. Finally, due to the relatively low density of the capsule fill gas *in some ICF experiments*, kinetic effects manifest themselves via species separation between the D and T atoms in the fusion gas. This results in DD and DT yield ratios

that differ greatly from hydrodynamic prediction [15, 16].

These mixing issues are just a few examples of kinetic effects; other non-equilibrium physics such as laser-plasma interaction, self-generated electromagnetic fields, Knudsen layers, and detailed shock structure may also have a significant impact on predictive modeling of ICF [8]. Due to the integrated nature of ICF experiments, it is difficult to study any of these effects in isolation. The MARBLE campaign fielded a unique separated reactants experiment in an attempt to measure mixing rates in ICF implosions via changes in the capsule DT yield [17, 18]. It was conjectured that atomic mixing and ion temperature separation played significant roles in the resulting DT/DD fusion yields [19]. The impending BOSQUE campaign is a direct drive follow-up to MARBLE campaign that uses larger capsules (~2X). The larger burn volumes are expected to achieve triple the temperatures and much higher thermonuclear yields (~100X to ~1000X) [20]. It is reasonable to expect kinetic effects like atomic mixing and temperature seperation will remain significant at higher hot spot temperatures.

Accurate predictions of ICF experiments benefit from the ability to describe temperature separation, velocity separation, viscosity, conduction, and diffusion in mixed material regions. Due to the dimensionality and time resolution constraints required by non-equilibrium models, a fully kinetic simulation of an ICF experiment is currently not feasible. Most approaches are limited to short time scales and small regions in space. With that, we propose a hybrid, coupled, multispecies fluid-kinetic approach which ensures that the added expense of kinetic modeling is only applied in regions where it is necessary, while the relatively less expensive hydrodynamic equations are solved in the remainder of the computational domain. This chapter builds on and extends the original kinetic-continuum domain decomposition by Degond et al. [1] to consider multiple particle species. Throughout the chapter, we will refer to this method as the *kinetic-hydro* decomposition or hybrid method. For the kinetic and hydrodynamic models we use an entropic, conservative Bhatnagar-Gross-Krook (BGK) description [21] and its associated multi-species fluid equations, respectively. In this chapter, the Chapman-Enskog expansion is used to obtain the associated multi-species fluid equations in both the Euler and Naver-Stokes limits in three dimensions (3D).

The chapter is organized as follows. In Section 2, we introduce the multispecies kinetic equation and the associated Euler and Navier-Stokes hydrodynamic limits. In Section 3, we describe the hybrid method which couples the kinetic and hydrodynamic models via a buffer region, providing a continuous transition between both. In Section 4, we present proof of concept 1D simulations which demonstrate the method for a Sod problem and a preheated pore inspired by the pores in a MARBLE capsule [17]. We present summary and outlook in Section 5. Additional details of the analytic derivation of the hybrid method, especially for the Navier-Stokes hydrodynamic model, are provided in the Appendix.

4.2 The multispecies kinetic and hydrodynamic models

In this section, we give a brief description of the BGK model and its limiting hydrodynamic equations. Both limits will be coupled via the hybrid approach in Section 4.3. For a single particle species, the BGK collision operator is a nonlinear relaxation operator of the form

$$Q_{BGK}[f] = \nu\,(M[f] - f), \tag{4.1}$$

where ν is a collision frequency, $f = f(\mathbf{x}, \mathbf{c}, t)$ is the phase-space density function depending on particle position $\mathbf{x}$, velocity $\mathbf{c}$, and time t. The Maxwellian $M[f]$ is the local equilibrium state based on the moments of f:

$$M[f] = n\left(\frac{m}{2\pi T}\right)^{3/2} \exp\left(-\frac{m(\mathbf{c}-\mathbf{v})^2}{2T}\right). \tag{4.2}$$

Here m is the mass of the species, while the particle number density n, bulk velocity $\mathbf{v}$, and temperature T are defined by

$$n \equiv \int f\, d\mathbf{c}, \qquad \mathbf{v} \equiv \frac{1}{n}\int \mathbf{c} f\, d\mathbf{c}, \qquad T \equiv \frac{m}{3n}\int (\mathbf{c}-\mathbf{v})^2 f\, d\mathbf{c}. \tag{4.3}$$

The BGK model is the simplest kinetic approach which captures the most fundamental properties of the Boltzmann collision model, namely, that it locally conserves mass, momentum, and energy and satisfies Boltzmann's H-Theorem. The multispecies BGK model is an analogue of the description for a single species. It is a set of nonlinear relaxation operators that conserve the species masses,

pairwise momentum, and pairwise kinetic energy as well as satisfies the multispecies H-Theorem [21]. In a nutshell, the model is defined as

$$Q_i^{\mathrm{BGK}} = \sum_j Q_{ij}^{\mathrm{BGK}}[f_i, f_j], \tag{4.4}$$

where Q_i^{BGK} is the collision operator for species i,

$$Q_{ij}^{BGK}[f_i, f_j] \equiv \nu_{ij}(M_{ij}[f_i, f_j] - f_i) \tag{4.5}$$

is the multi-species collision operator for the interaction between species i and j with the corresponding phase-space density functions f_i and f_j. ν_{ij} is the frequency which the i species collides with the j species. Furthermore, the inter-species Maxwellians are

$$M_{ij}[f_i, f_j] \equiv n_i \left(\frac{m_i}{2\pi T_{ij}}\right)^{3/2} \exp\left(-\frac{m_i(\mathbf{c} - \mathbf{v}_{ij})^2}{2T_{ij}}\right) \tag{4.6}$$

To define v_{ij} and T_{ij}, we enforce conservation of mass, momentum, and energy [21] which gives the following algebraic relations:

$$\mathbf{v}_{ij} = \frac{\rho_i \nu_{ij}\mathbf{v}_i + \rho_j \nu_{ji}\mathbf{v}_j}{\rho_i \nu_{ij} + \rho_j \nu_{ji}}, \qquad T_{ij} = \frac{n_i \nu_{ij} T_i + n_j \nu_{ji} T_j}{n_i \nu_{ij} + n_j \nu_{ji}} + \frac{\rho_i \nu_{ij}(v_i^2 - v_{ij}^2) + \rho_j \nu_{ji}(v_j^2 - v_{ij}^2)}{3\left(n_i \nu_{ij} + n_j \nu_{ji}\right)}. \tag{4.7}$$

Equivalent to Eq.Eq(4.3), the moments of each species are given by

$$n_i \equiv \int f_i d\mathbf{c}, \qquad \mathbf{v}_i \equiv \frac{1}{n_i}\int \mathbf{c} f_i d\mathbf{c}, \qquad T_i \equiv \frac{m_i}{3n_i}\int (\mathbf{c} - \mathbf{v}_i)^2 f_i d\mathbf{c}. \tag{4.8}$$

The multi-species collision operator forms a key part of the BGK equation,

$$\partial_t f_i + \mathbf{c} \cdot \nabla_x f_i + \mathbf{a}_i \cdot \nabla_{\mathbf{c}} f_i = \sum_j Q_{ij}^{\mathrm{BGK}}[f_i, f_j], \tag{4.9}$$

where $\mathbf{a}_i$ is an acceleration term, for example for charged particles in the presence of an electric field.

4.2.1 The multi-species Navier-Stokes model

The Navier-Stokes equations for the conservation of mass, momentum and energy, associated to the multispecies BGK model are [21, 22]

$$\partial_t \rho_i + \nabla_{\mathbf{x}} \cdot (\rho_i \mathbf{v}) + \nabla_{\mathbf{x}} \cdot (\rho_i \mathbf{V}_i) = 0, \tag{4.10}$$

$$\partial_t (\rho \mathbf{v}) + \nabla_{\mathbf{x}} \cdot (\rho \mathbf{v} \otimes \mathbf{v}) + \nabla_{\mathbf{x}} \cdot \mathrm{P} = \sum_i \rho_i \, \mathbf{a}_i, \tag{4.11}$$

$$\frac{3}{2} \left(\partial_t (nT) + \nabla_{\mathbf{x}} \cdot (nT\mathbf{v}) \right) + \nabla_{\mathbf{x}} \cdot \mathbf{q} + \mathrm{P} : \nabla_x \mathbf{v} = \sum_i \mathbf{V}_i \cdot \mathbf{a}_i. \tag{4.12}$$

Here, $n = \sum_i n_i$ is the total particle number density, $\rho_i = m_i n_i$ is the species mass density with the total density $\rho = \sum_i \rho_i$. The velocity of the mixture is given by $\mathbf{v} = \frac{1}{\rho} \sum_i \rho_i \mathbf{v}_i$ while $\mathbf{V}_i = \mathbf{v}_i - \mathbf{v}$ is the (macroscopic) diffusion velocity for species i. Finally, the pressure tensor[1] is P, T is the mixture temperature, and $\mathbf{q}$ is the heat flux. These thermodynamic quantities can be given in terms of the distributions f_i by

$$\mathrm{P} = \sum_i \mathrm{P}_i \equiv \sum_i \int m_i \mathbf{C} \otimes \mathbf{C} f_i d\mathbf{c}, \tag{4.13}$$

$$T \equiv \frac{2}{3n} \sum_i \int \frac{m_i}{2} C^2 f_i d\mathbf{c}, \tag{4.14}$$

$$\mathbf{q} = \sum \mathbf{q}_i \equiv \sum_i \int \frac{m_1}{2} \mathbf{C} C^2 f_i d\mathbf{c}, \tag{4.15}$$

where $\mathbf{C} = \mathbf{c} - \mathbf{v}$ is the microscopic diffusion velocity. The macroscopic diffusion velocity, pressure tensor, and heat flux are written in terms of the hydrodynamic variables as

$$\mathbf{V}_i = \sum_j D_{ij} \mathbf{d}_j, \tag{4.16}$$

$$\mathrm{P} = nT\mathrm{I} - \eta \left(\nabla_{\mathbf{x}} \mathbf{v} + (\nabla_{\mathbf{x}} \mathbf{v})^T - \frac{2}{3} (\nabla_{\mathbf{x}} \cdot \mathbf{v}) \mathrm{I} \right), \tag{4.17}$$

$$\mathbf{q} = -\kappa \nabla_{\mathbf{x}} T + \sum_i \frac{5T}{2m_i} \rho_i \mathbf{V}_i, \tag{4.18}$$

[1] Technically P is a mean-field pressure tensor, and additional contributions from the various force terms $\mathbf{a}_i$ can be grouped with the pressure in the resultant hydrodynamic equations, e.g., electron pressure terms. For other EOS types, e.g. polyatomic gases with additional degrees of freedom, matching an EOS requires introducing additional phase space variables; see [Munafo et al, JCP, 2014].

with the diffusion driving force term $\mathbf{d}_i$ defined in 4A. The coefficients D_{ij}, ν, κ for interdiffusion, viscosity, and thermal conductivity, respectively, are the *transport coefficients* of the hydrodynamic model. Their formulations are directly related to the underlying BGK kinetic system [21]. Note that in the Euler equations, these transport coefficients are zero.

4.3 Coupling of the BGK and continuum equations for multiple species in 3D

In this section, we derive the analytical description for the kinetic-hydro decomposition and the connecting buffer region, both for the multispecies BGK, as well as the associated Euler and Navier-Stokes equations. For simplicity, we drop the acceleration term $\mathbf{a}_i$ in the remainder of the chapter. As will be shown in section 4.5.2, it can be reintroduced to the fluid limit without major changes to the resulting equations. We begin with the multi-species BGK formulation.

As in [21], we introduce a scaling parameter ϵ to the collision operators that is analogous to the Knudsen number. Its role is to emphasize the highly collisional regime and assist with the approximation process. The corresponding BGK equations are:

$$\begin{aligned} \partial_t f_i + \mathbf{c} \cdot \nabla_x f_i &= \frac{1}{\epsilon} Q_i[f], \\ Q_i[f] &= \sum_j Q_{ij}[f_i, f_j], \end{aligned} \tag{4.19}$$

where we remove the BGK superscript for better readability. We assume that the kinetic effects are only important in relatively small, localized regions of the computational domain, for example around an interface or shock. The domain is decomposed into fluid regions, where we expect the usual hydrodynamic limit to hold locally, and kinetic regions, where non-equilibrium physics has a significant effect. However, simply inserting an interface between the two models requires devising compatible boundary conditions for each model. Following [1] we therefore introduce a buffer region between the kinetic and hydrodynamic areas that provides a smooth transition between the two models. In this buffer region, both the fluid and kinetic models are solved with some modifications. The solution to the hybrid model is recovered as the weighted sum of the coupled kinetic and hydrodynamic descriptions. At the edge of the buffer region, the modified fluid or kinetic model becomes degenerate and the hybrid model smoothly transitions into only

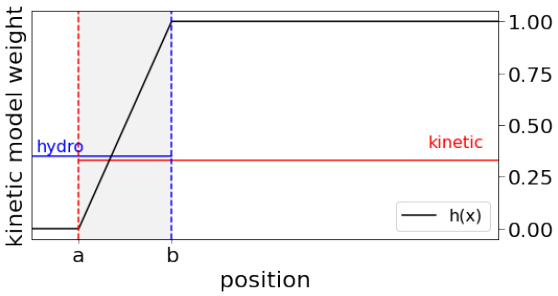

Figure 4.1 Example of a buffer function $h(x)$. As $h(x)$ varies within the interval $[0, 1]$, it transitions the hybrid model between pure hydrodynamic and pure kinetic regions. For $x \leq a$, a value of $h(x) = 0$ indicates the continuum regime. For $x \geq b$, the transition function is $h(x) = 1$ and matter is in non-equilibrium.

solving the respective kinetic or fluid equations. Thus no special boundary conditions are required. However, as we will show below, one must ensure that the buffer region is placed in an area where a hydrodynamic limit is reasonable. In practice, the spatial location of the kinetic region may dynamically change, and a moving buffer region may be required. As is shown in the single species context [2], the addition of a time-dependent buffer region adds many extra terms to the hybrid equations. For simplicity of presentation, we focus on a fixed buffer region in this manuscript, and the extension to moving buffer regions in the multispecies context will be the subject of future work.

The buffer region is characterized by a continuous transition function $h(x)$ which is defined to be 1 and 0 in the kinetic and fluid regimes, respectively. For a buffer region in an interval $[a, b]$, the simplest choice is a linear dependence on x, i.e.,

$$h(x) = \begin{cases} 1, & x \leq a, \\ 0, & x \geq b, \\ 0 \leq (x-b)/(a-b) \leq 1, & x \in [a, b]. \end{cases} \tag{4.20}$$

Figure 4.1 gives a graphical example of a computational domain that is divided in hydrodynamic, buffer, and kinetic regions, together with the corresponding transition function.

In order to focus on the coupled equations in the buffer region, we assume that the transition function is fixed in time. Dynamic buffer regions, as e.g. derived for the single species hybrid model [2], will be the subject of future work. For simplicity, we will also express the transition

function as h. We use it to create a coupled system of kinetic and hydrodynamic equations by splitting the full distribution function f_i into kinetic and a fluid parts,

$$f_i = f_{iK} + f_{iF}, \tag{4.21}$$

$$f_{iF} \equiv (1-h)\, f_i, \qquad f_{iK} \equiv h\, f_i. \tag{4.22}$$

Multiplying Eq. (4.19) with h and $(1-h)$ and using the definitions of f_{iK} and f_{iF}, we can rewrite the transport equation into a system of two coupled equations:

$$\partial_t f_{iK} + h\,\mathbf{c}\cdot\nabla_x f_{iK} + h\,\mathbf{c}\cdot\nabla_x f_{iF} = \frac{h}{\epsilon}\, Q_i\,[f] \tag{4.23}$$

$$\partial_t f_{iF} + (1-h)\,\mathbf{c}\cdot\nabla_x f_{iF} + (1-h)\,\mathbf{c}\cdot\nabla_x f_{iK} = \frac{(1-h)}{\epsilon}\, Q_i\,[f]. \tag{4.24}$$

In the following, we will take moments of the equation for f_{iF} with respect to

$$\mathbf{m} = \left(m_i,\ m_i\mathbf{c},\ \frac{m_i}{2}c^2\right) \tag{4.25}$$

to obtain the equations for the mass, momentum, and energy *contained in the fluid piece* of the decomposition. This results in the continuum equations

$$\langle \partial_t \mathbf{m} f_{iF}\rangle + (1-h)\,\langle \mathbf{mc}\cdot\nabla_x f_{iF}\rangle + (1-h)\,\langle \mathbf{mc}\cdot\nabla_x f_{iK}\rangle = \frac{1-h}{\epsilon}\left\langle \mathbf{m}\sum_j Q_{ij}[f_i, f_j]\right\rangle. \tag{4.26}$$

Here and for the remainder of this chapter, $\langle\rangle$ denotes

$$\langle\phi\rangle = \int \phi\ \mathrm{d}\mathbf{c}. \tag{4.27}$$

When $h = 1$, the system simply reduces to the original kinetic transport equation for f_{iK} as given in Eq. Eq(4.9). For $h = 0$ and assuming the standard Euler (or Navier-Stokes) closure, Eq. Eq(4.26) can be written as a set of hydrodynamic equations for n_i, $\mathbf{v}$, and T, as given in Eqs. Eq(4.10) - Eq(4.12). Finally, when $0 < h < 1$, Eq. Eq(4.23) requires f_{iF} for its streaming and collision updates while Eq. Eq(4.26) uses f_{iK} for one of its flux terms. Furthermore, we note that in the buffer region, the moment variables n_i, $\mathbf{v}$, and T in Eq. Eq(4.26) correspond to the *moments of* f_{iF} and not the moments of the total distribution function $f = f_{iK} + f_{iF}$. The main remaining task is to determine the Euler and Navier-Stokes closures of the new fluid system in Eq. Eq(4.26), which differs from the standard approach due to the presence of h and the kinetic contribution f_{iK}.

4.3.1 Multi-species kinetic-Euler system in the buffer region

We begin by deriving the kinetic-hydro coupling for an Euler closure. The coupling between BGK and the Navier-Stokes equations will be discussed in the next section and naturally builds on top of this foundation. For the Euler derivation, we assume that $\epsilon \ll 1$ in Eq. Eq(4.24) and order terms by its powers. Recalling that the collision operator depends of the full distribution function f_i, the leading order term is

$$0 = \sum_j Q_{ij} \left[f_{iF} + f_{iK}, f_{jF} + f_{jK} \right]. \tag{4.28}$$

We can rewrite the right-hand side into

$$0 = \sum_j Q_{ij} \left[f_{iF}, f_{jF} \right] + \left(Q_{ij} \left[f_{iF} + f_{iK}, f_{jF} + f_{jK} \right] - Q_{ij} \left[f_{iF}, f_{jF} \right] \right). \tag{4.29}$$

Since $\epsilon \ll 1$, that is, the buffer region is in a regime where the hydrodynamic limit applies, we assume that $f - f_F \approx O(\epsilon)$ and thus the difference term in Eq. Eq(4.29) satisfies

$$\sum_j \left(Q_{ij} \left[f_{iF} + f_{iK}, f_{jF} + f_{jK} \right] - Q_{ij} \left[f_{iF}, f_{jF} \right] \right) \approx O(\epsilon). \tag{4.30}$$

As a result, at leading order, the collision operator is

$$\sum_j Q_{ij} \left[f_{iF}, f_{jF} \right] = 0. \tag{4.31}$$

By standard H-Theorem arguments [22], f_{iF} must therefore be a Maxwellian distribution given by Eq. Eq(4.2). With this approximation to f_{iF}, we derive the resulting Euler equations. To simplify the moment calculations we note that any reasonable collision operator, including the multi-species BGK operator, should conserve pairwise mass, momentum, and energy. For any given distribution functions, ψ and ϕ, these conservation properties can be written as [21]

$$\begin{aligned} \left\langle m_i Q_{ij} \left[\psi, \phi \right] \right\rangle &= 0 \\ \left\langle m_i \, \mathbf{c} \, Q_{ij} \left[\psi, \phi \right] \right\rangle + \left\langle m_j \, \mathbf{c} \, Q_{ji} [\psi, \phi] \right\rangle &= 0 \\ \left\langle m_i \, c^2 \, Q_{ij} [\psi, \phi] \right\rangle + \left\langle m_j \, c^2 \, Q_{ji} [\psi, \phi] \right\rangle &= 0. \end{aligned} \tag{4.32}$$

For compactness in the following derivations, we define the 1^{st}, 2^{nd}, and 3^{rd} moments of the kinetic distribution function as

$$\mathbf{K}_{1,i} \equiv \langle m_i \, \mathbf{c} \, f_{iK} \rangle \,, \quad \mathrm{K}_{2,i} \equiv \langle m_i \, (\mathbf{c} \otimes \mathbf{c}) \, f_{iK} \rangle \,, \quad \mathbf{K}_{3,i} \equiv \left\langle \frac{m_i}{2} \, \mathbf{c} \, c^2 \, f_{iK} \right\rangle . \tag{4.33}$$

The total n^{th} kinetic moment across all species i is given by

$$\mathbf{K}_n \equiv \sum_i \mathbf{K}_{n,i}. \tag{4.34}$$

To obtain the equation for the conservation of mass, we compute

$$\langle m_i \, \partial_t f_{iF} \rangle + (1-h) \, \langle m_i \, \mathbf{c} \cdot \nabla_x f_{iF} \rangle + (1-h) \, \langle m_i \, \mathbf{c} \cdot \nabla_x f_{iK} \rangle = \frac{(1-h)}{\epsilon} \, \langle m_i \, Q_i \, [f] \rangle \,, \tag{4.35}$$

which results in

$$\partial_t \rho_i + \, (1-h) \, \nabla_x \cdot (\rho_i \mathbf{v}) + (1-h) \, \nabla_x \cdot \langle m_i \, \mathbf{c} \, f_{iK} \rangle = 0. \tag{4.36}$$

This can be rewritten as an equation for the conservation of the number density. Defining $\tilde{\mathbf{K}}_{1,i} \equiv \mathbf{K}_{1,i}/m_i$, we obtain

$$\partial_t n_i + (1-h) \nabla_x \cdot (n_i \mathbf{v}) + (1-h) \, \nabla_x \cdot \tilde{\mathbf{K}}_{1,i} = 0. \tag{4.37}$$

We also note that this can be trivially re-formulated into an expression for the conservation of mass fraction $Y_i = \rho_i / \rho$

$$\partial_t (\rho Y_i) + (1-h) \nabla_x \cdot (\rho \mathbf{v} Y_i) + (1-h) \, \nabla_x \cdot \mathbf{K}_1 = 0. \tag{4.38}$$

Summing Eq. Eq(4.36) over all species i, we arrive at the conservation equation for the total mass

$$\mathrm{D}_t \, \rho + (1-h) \, \rho \nabla_x \cdot \mathbf{v} + (1-h) \, \nabla_x \cdot \mathbf{K}_1 = 0, \tag{4.39}$$

where the time derivative is given by $\mathrm{D}_t = \partial_t + (1-h) \, \mathbf{v} \cdot \nabla_x$. The equation for conservation of total momentum can be obtained by multiplying Eq. (4.24) by $m_i \mathbf{c}$, integrating over $\mathbf{c}$, and summing the result over all species. This gives

$$\partial_t (\rho \mathbf{v}) + (1-h) \nabla_{\mathbf{x}} \cdot (\rho \mathbf{v} \otimes \mathbf{v}) + (1-h) \nabla_{\mathbf{x}} \cdot \mathrm{P} + (1-h) \nabla_{\mathbf{x}} \cdot \mathrm{K}_2 = 0 \tag{4.40}$$

where $\mathrm{P} = \sum_i \mathrm{P}_i = nT\mathrm{I}$. For convenience, we reformulate this expression in terms of the primitive variable $\mathbf{v}$ by using Eq. Eq(4.39). We obtain

$$\rho\, \mathrm{D}_t\mathbf{v} + (1-h)\, \nabla_x \cdot \mathrm{P} - (1-h)\, \mathbf{v}\ (\nabla_x \cdot \mathbf{K}_1) + (1-h)\, \nabla_x \cdot \mathrm{K}_2 = 0. \tag{4.41}$$

Next we define J_{iK} and J_K

$$\mathbf{J}_K = \sum_i \mathbf{J}_{iK} \equiv \sum_i \nabla_x \cdot \mathrm{K}_{2,i} - \mathbf{v}\ \left(\nabla_x \cdot \mathbf{K}_{1,i}\right), \tag{4.42}$$

where the subscript K marks the fact that these contributions come from the kinetic distributions f_{iK}. With this definition, we can rewrite Eq. Eq(4.41) in a more compact form as

$$\rho\, \mathrm{D}_t\mathbf{v} + (1-h)\, \nabla_x \cdot \mathrm{P} + (1-h)\, \mathbf{J}_K = 0. \tag{4.43}$$

Finally, for the conservation of energy, we multiply Eq. (4.24) by $\frac{m_i}{2}C^2$, integrate again over $\mathbf{c}$, and sum over all species. This gives

$$\partial_t \left(\frac{3}{2}nT\right) + (1-h)\, \nabla_x \cdot \left(\frac{3}{2}nT\mathbf{v}\right) + (1-h)\, \mathrm{P} : \nabla_x\mathbf{v} + (1-h)\, H_K = 0, \tag{4.44}$$

where H_K gathers moments of f_{iK} and is defined by

$$H_K = \sum_i H_{iK} \equiv \sum_i \left\langle \frac{m_i}{2}C^2\, (\mathbf{c} \cdot \nabla_x f_{iK}) \right\rangle. \tag{4.45}$$

Using the fact that f_{iF} is a Maxwellian, we have $\mathrm{P} : \nabla_x\mathbf{v} = nT(\nabla_x \cdot \mathbf{v})$ and $\mathbf{q} = 0$. We can also reformulate this in terms of the primitive variable T. Using Eq. (4.37), we obtain

$$\mathrm{D}_t T + (1-h)\frac{2}{3}T\, (\nabla_x \cdot \mathbf{v}) + (1-h)\frac{2}{3}\frac{1}{n}H_K - (1-h)\frac{1}{n}T\, \nabla_x \cdot \tilde{\mathbf{K}}_1 = 0. \tag{4.46}$$

Equations (4.23), (4.36), (4.43), and (4.46) form the closed set of hybrid kinetic-Euler equations that describe the flow dynamics in the buffer region.

4.3.2 Multi-species kinetic-Navier-Stokes system in the buffer region

As the Euler equations assume inviscid fluids, they are often not sufficient to describe physical flows in the continuum region. Instead, capturing near-equilibrium effects such as viscosity or atomic interdiffusion requires a further extension of the hydrodynamics model to the Navier-Stokes

closure. To describe near-equilibrium effects in the hydrodynamic model, we therefore expand f_{iF} in terms of ϵ

$$f_{iF} = f_{iF}^{(0)} + \epsilon f_{iF}^{(1)}. \tag{4.47}$$

Note that the term $f_{iF}^{(1)}$ describes the deviation from equilibrium but is different from the kinetic distribution f_{iK}. Instead, this term captures the Navier-Stokes closure in terms of the moments of f_{iF}. In a pure fluid region where $h = 0$, the term $f_{iF}^{(1)}$ is simply the standard Navier-Stokes correction [22, 21]

$$f_{iF}^{(1)} = -\frac{M_i}{\nu_i}\left[\left(\frac{m_i}{2T}C^2 - \frac{5}{2}\right)\mathbf{C}\cdot\nabla_{\mathbf{x}}\log T + \frac{n}{n_i}\mathbf{C}\cdot\mathbf{d}_i + \frac{m_i}{T}\left(\mathbf{C}\otimes\mathbf{C} - \frac{1}{3}\mathrm{I}\right) : \nabla_{\mathbf{x}}\mathbf{v} + \sum_j \frac{\nu_{ij}}{\nu_i}\frac{m_i}{T}\mathbf{C}\cdot\mathbf{v}_{ij}^{(1)}\right], \tag{4.48}$$

where M_i is again the Maxwellian for species i with moments $n_i, \mathbf{v}, T$, and $\nu_i = \sum_j \nu_{ij}$. The diffusive velocity correction $\mathbf{v}_{ij}^{(1)}$ is the solution to a symmetric linear system. As in the Euler case, we cannot use the standard Chapman-Enskog result due to the presence of the kinetic distributions f_{iK} and must determine its effect on the eventual hydrodynamic equations. To simplify the calculation, we rewrite Eq. Eq(4.24) in terms of the diffusion velocity $\mathbf{C}$. The time and space derivatives are then expressed as $\partial_t \to \partial_t - \partial_t\mathbf{v}\cdot\nabla_{\mathbf{C}}$ and $\nabla_x \to \nabla_x - (\nabla_x \otimes \mathbf{v})\cdot\nabla_{\mathbf{C}}$ respectively [22], and Eq. Eq(4.24) becomes:

$$\begin{aligned}\partial_t f_{iF} - \mathrm{D}_t\left(\mathbf{v}\cdot\nabla_{\mathbf{C}} f_{iF}\right) + (1-h)(\mathbf{C}+\mathbf{v})\cdot\nabla_x f_{iF} - (1-h)(\mathbf{C}\otimes\nabla_{\mathbf{C}} f_{iF}) : (\nabla_x\otimes\mathbf{v}) \\ +(1-h)\,\mathbf{c}\cdot\nabla_x f_{iK} = \frac{(1-h)}{\epsilon}Q_i[f].\end{aligned} \tag{4.49}$$

Note that we did not modify the term including f_{iK}, as there is no benefit to do so. This term is passively carried along during the Navier-Stokes derivation for f_{iF} [2]. As in the Euler case, we add and subtract a collision term that contains only f_{iF} and rewrite the collision operator as

$$Q_i[f] = \Delta_i + \sum_j Q[f_{iF}, f_{jF}], \tag{4.50}$$

$$\Delta_i = \sum_j \Delta_{ij} = \sum_j \left(Q[f_i, f_j] - Q[f_{iF}, f_{jF}]\right). \tag{4.51}$$

[2] One can simply write $\mathbf{c} = \mathbf{C} + \mathbf{v}$ to use the same set of variables as f_{iF}

Here, Δ_i is the difference between the collision operator for the full distributions f_i and the operator for the fluid distributions f_{iF}. We write $Q_{ij}[f_{iF}, f_{jF}] \equiv Q[f_{iF}, f_{jF}]$ for simplicity. Assuming that the hydrodynamic approximation applies in the buffer region means that Δ_i is of the order ϵ and any following expansion produces terms of the order ϵ^2. We further assume (and will later show) that inserting the expansion of Eq. Eq(4.47) into the first term of the collision operator yields

$$Q[f_{iF}, f_{jF}] \approx Q^{(0)}[f_{iF}, f_{jF}] + \epsilon Q^{(1)}[f_{iF}, f_{jF}] \tag{4.52}$$

and thus

$$Q[f_{iF}, f_{jF}] \approx \epsilon Q^{(1)}[f_{iF}, f_{jF}]. \tag{4.53}$$

$Q^{(1)}$ and related terms are defined in 4A (see e.g., Eq. Eq(4A.17)). As in the Euler case, at leading order in ϵ, Eq.Eq(4.24) results in

$$\sum_j Q_{ij}\left[f_{iF}^{(0)}, f_{jF}^{(0)}\right] = 0. \tag{4.54}$$

By the same argument, the leading order terms in the expansion must be Maxwellians. At the next order, we have

$$\begin{aligned}\partial_t f_{iF}^{(0)} - \mathrm{D}_t\left(\mathbf{v}\cdot\nabla_{\mathbf{C}} f_{iF}^{(0)}\right) + (1-h)\,(\mathbf{C}+\mathbf{v})\cdot\nabla_x f_{iF}^{(0)} \\ - (1-h)\,(\mathbf{C}\otimes\nabla_{\mathbf{C}} f_{iF}^{(0)}) : (\nabla_x \otimes \mathbf{v}) + (1-h)\,\mathbf{c}\cdot\nabla_x f_{iK} = (1-h)\,Q_i^{(1)}[f_{iF}^{(1)}] + (1-h)\,\Delta_i.\end{aligned} \tag{4.55}$$

From here, the usual Chapman-Enskog workflow is to compute an expression for $f_{iF}^{(1)}$ via equations Eq(4.37), Eq(4.43), and Eq(4.46). Once $f_{iF}^{(1)}$ is known, we can determine the various Navier-Stokes correction terms, i.e. $\mathbf{V}_i$, P, $\mathbf{q}$. The calculations to expand Q in terms of ϵ and subsequently

determine $f_{iF}^{(1)}$ can be found in 4A. Here, we present the final result [3]

$$
\begin{aligned}
f_i^{(1)} = &\sum_j \frac{\nu_{ij}}{\nu_i} f_{iF}^{(0)} \left[\frac{m_i}{T} \mathbf{C} \cdot \mathbf{v}_{ij}^{(1)} + \left(\frac{\frac{1}{2} m_i C^2}{T} - \frac{3}{2} \right) \frac{T_{ij}^{(1)}}{T} \right] \\
&- \frac{f_{iF}^{(0)}}{\nu_i} \left[\frac{m_i}{T} \left(\mathbf{C} \otimes \mathbf{C} - \frac{1}{3} C^2 \mathrm{I} \right) : (\nabla_x \otimes \mathbf{v}) + \mathbf{C} \cdot \left(\left(\frac{m_i}{2T} C^2 - \frac{5}{2} \right) \nabla_x \log(T) \right) + \frac{n}{n_i} \mathbf{C} \cdot \mathbf{d}_i \right. \\
&\left. - \frac{m_i}{\rho T} \mathbf{C} \cdot \mathbf{J}_K + \left(1 - \frac{m_i C^2}{3T} \right) \left(\frac{1}{nT} H_K - \frac{3}{2n} \nabla_x \cdot \tilde{\mathbf{K}}_1 \right) - \frac{1}{n_i} \nabla_x \cdot \tilde{\mathbf{K}}_{1,i} \right] - \frac{1}{\nu_i} \mathbf{c} \cdot \nabla_x f_{iK} + \frac{1}{\nu_i} \Delta_i .
\end{aligned}
\tag{4.56}
$$

We derive the conservation of total mass by inserting Eq. Eq(4.47) into Eq. Eq(4.49) and performing the usual integration. The result is,

$$
\partial_t \, \rho + (1 - h) \, \nabla_x \cdot (\rho \mathbf{v}) + (1 - h) \nabla_{\mathbf{x}} \cdot (\rho \mathbf{V}_i) + (1 - h) \, \nabla_x \cdot \mathbf{K}_1 = 0. \tag{4.57}
$$

The species diffusion velocities $\mathbf{V}_i$ are obtained by solving the system of equations

$$
A \mathbf{V}_i = \mathbf{w} - \langle m \mathbf{C} \, \Delta_i \rangle \, , \tag{4.58}
$$

with

$$
A_{ij} = \begin{cases} - \sum_j \frac{\rho_i \rho_j \nu_{ij} \nu_{ji}}{\rho_i \nu_{ij} + \rho_j \nu_{ji}} - \rho_i \, \rho_j, & \text{if } i = j \\ \frac{\rho_i \rho_j \nu_{ij} \nu_{ji}}{\rho_i \nu_{ij} + \rho_j \nu_{ji}} - \rho_i \, \rho_j, & \text{if } i \neq j \end{cases} , \tag{4.59}
$$

$$
\mathbf{w}_i \equiv nT \mathbf{d}_i - \frac{\rho_i}{\rho} \, \mathbf{J}_K + \mathbf{J}_{iK}, \tag{4.60}
$$

$$
\mathbf{J}_{iK} \equiv \nabla_x \cdot \mathrm{K}_{2,i} - \mathbf{v} \, (\nabla_x \cdot \mathbf{K}_{1,i}). \tag{4.61}
$$

For the conservation of momentum, we insert the expansion for f_{iF} from Eq. Eq(4.47) into the Eq. Eq(4.49), multiply by $m_i \mathbf{c}$, integrate over $\mathbf{c}$, and sum over all species. The resulting equation is

$$
\partial_t \, (\rho \mathbf{v}) + (1 - h) \, \nabla_x \cdot \left(p \mathrm{I} + \epsilon \sum_i \mathrm{P}_i^{(1)} \right) + (1 - h) \, \nabla_x \cdot (\mathbf{v} \otimes \mathbf{v} \rho) + (1 - h) \, \nabla_x \cdot \mathrm{K}_2 = 0 \tag{4.62}
$$

[3] This expression is not closed, as $\mathbf{v}_{ij}^{(1)}$ and $T_{ij}^{(1)}$ implicitly depend on $f_{iF}^{(1)}$. See 4A.3 for the linear systems that must be satisfied to fully define $f_{iF}^{(1)}$

with:

$$\mathrm{P}_i^{(1)} = -\frac{n_i T}{\nu_i}\left((\nabla_x \otimes \mathbf{v}) + (\nabla_x \otimes \mathbf{v})^{\mathrm{T}} - \frac{2}{3}(\nabla_x \cdot \mathbf{v})\,\mathrm{I}\right) + \sum_j \frac{\nu_{ij}}{\nu_i} T_{ij}^{(1)}\, n_i\,\mathrm{I} \tag{4.63}$$

$$+\frac{1}{\nu_i} s_i\,\mathrm{I} - \left\langle m_i \left(\mathbf{C}\otimes\mathbf{C} - \frac{1}{3}C^2\,\mathrm{I}\right)\,\mathbf{c}\cdot\nabla_x f_{iK}\right\rangle + \frac{1}{\nu_i}\left\langle m_i\,(\mathbf{C}\otimes\mathbf{C})\,\Delta_i\right\rangle. \tag{4.64}$$

The cross-species temperature

$$T_{ij}^{(1)} = \frac{n_i \nu_{ij} T_i^{(1)} + n_j \nu_{ji} T_j^{(1)}}{n_i \nu_{ij} + n_j \nu_{ji}}, \tag{4.65}$$

is obtained by solving the system of equations

$$B\,\mathbf{T}^{(1)} = \mathbf{s} - \left\langle m_i C^2 \Delta_i\right\rangle,$$
$$B_{ij} = \begin{cases} -\sum_j \frac{n_i n_j \nu_{ij}\nu_{ji}}{n_i\nu_{ij}+n_j\nu_{ji}} - n_i n_j, & \text{if } i = j \\ \frac{n_i n_j \nu_{ij}\nu_{ji}}{n_i\nu_{ij}+n_j\nu_{ji}} - n_i n_j, & \text{if } i \neq j \end{cases}. \tag{4.66}$$

with

$$s_i \equiv -\frac{2}{3}\left(\frac{n_i}{n}H - H_i\right) + T\left(\frac{n_i}{n}\nabla_x\cdot\tilde{\mathbf{K}}_1 - \nabla_x\cdot\tilde{\mathbf{K}}_{1,i}\right) \tag{4.67}$$

$$H_{iK} \equiv \frac{1}{2}\,\mathbf{v}^2\,\nabla_x\cdot\mathbf{K}_{1,i} - \mathbf{v}\cdot\left(\nabla_x\cdot\mathrm{K}_{2,i}\right) + \nabla_x\cdot\mathbf{K}_{3,i}. \tag{4.68}$$

Finally, for the conservation of energy, we insert Eq.Eq(4.47) into the Eq.Eq(4.49), multiply by $\frac{m_i}{2}C^2$, integrate over $\mathbf{c}$, and sum over all species. This gives,

$$\frac{3}{2}\,\partial_t\,(nT) + (1-h)\,\frac{3}{2}\nabla_x\cdot(nT\mathbf{v}) + (1-h)\,\nabla_x\cdot\mathbf{q} + (1-h)\,\mathrm{P}:(\nabla_x\otimes\mathbf{v}) + (1-h)\,H_K = 0, \tag{4.69}$$

where $\mathbf{q} = \epsilon\sum_i \mathbf{q}_i$ and

$$\mathbf{q}_i = \frac{5}{2}\frac{T}{m_i}\left(\rho_i\mathbf{v}_i + \frac{1}{\nu_i}\mathbf{J}_i - \frac{n_i}{\nu_i}\nabla_x T\right) - \frac{1}{\nu_i}\left\langle\frac{m_i}{2}\,C^2\,\mathbf{C}\,(\mathbf{c}\cdot\nabla_x f_{iK})\right\rangle + \frac{1}{\nu_i}\left\langle\frac{m_i}{2}\,C^2\mathbf{C}\,\Delta_i\right\rangle. \tag{4.70}$$

Equivalent to the Euler closure, Eqn. Eq(4.23), Eq(4.57), Eq(4.62), and Eq(4.69) form the coupled kinetic and Navier-Stokes equations.

4.4 Example for the BGK-Navier-Stokes Coupling for Two Species

As an illustrative example and for potential future applications, we present the coupled BGK-NS equations for a system of two particle species. The conservation equations of mass densities ρ_1 and ρ_2 are:

$$\begin{aligned}
&\partial_t \rho_1 + (1-h)\,\nabla_x \cdot (\rho_1 \mathbf{v}) + (1-h)\,\nabla_x \cdot (\rho_1 \mathbf{V}_1) + (1-h)\,\nabla_x \cdot \mathbf{K}_{1,1} = 0,\\
&\partial_t \rho_2 + (1-h)\,\nabla_x \cdot (\rho_2 \mathbf{v}) + (1-h)\,\nabla_x \cdot (\rho_2 \mathbf{V}_2) + (1-h)\,\nabla_x \cdot \mathbf{K}_{1,2} = 0,
\end{aligned} \tag{4.71}$$

with

$$\begin{aligned}
\mathbf{V}_1 &= -\frac{\rho_2}{\rho_1}\frac{1}{\rho^2}\frac{\rho_i \nu_{ij} + \rho_j \nu_{ji}}{\nu_{ij}\nu_{ji}}(\mathbf{w}_1 - \langle m_1 \mathbf{C}\,\Delta_1\rangle) + \frac{1}{\rho^2}\frac{\rho_i \nu_{ij} + \rho_j \nu_{ji}}{\nu_{ij}\nu_{ji}}(\mathbf{w}_2 - \langle m_2 \mathbf{C}\,\Delta_2\rangle)\\
\mathbf{V}_2 &= \frac{1}{\rho^2}\,\frac{\rho_i \nu_{ij} + \rho_j \nu_{ji}}{\nu_{ij}\nu_{ji}}(\mathbf{w}_1 - \langle m_1 \mathbf{C}\,\Delta_1\rangle) - \frac{\rho_1}{\rho_2}\frac{1}{\rho^2}\frac{\rho_i \nu_{ij} + \rho_j \nu_{ji}}{\nu_{ij}\nu_{ji}}(\mathbf{w}_2 - \langle m_2 \mathbf{C}\,\Delta_2\rangle).
\end{aligned} \tag{4.72}$$

Inserting in values for $\mathbf{w}_1$ and $\mathbf{w}_2$ that are obtained by Eq. Eq(4.60), produces:

$$\begin{pmatrix}\mathbf{V}_1\\ \mathbf{V}_2\end{pmatrix} = -D\left(nT\begin{pmatrix}\mathbf{d}_1\\ \mathbf{d}_2\end{pmatrix} + \begin{pmatrix}\mathbf{J}_{1K}\\ \mathbf{J}_{2K}\end{pmatrix} - \begin{pmatrix}\langle m_1 \mathbf{C}\,\Delta_1\rangle\\ \langle m_2 \mathbf{C}\,\Delta_2\rangle\end{pmatrix}\right), \tag{4.73}$$

where the diffusion coefficients are

$$D = \frac{1}{\rho^2}\frac{\rho_1 \nu_{12} + \rho_2 \nu_{21}}{\nu_{12}\nu_{21}}\begin{bmatrix}\rho_2/\rho_1 & -1\\ -1 & \rho_1/\rho_2\end{bmatrix}. \tag{4.74}$$

The equation for the conservation of total momentum is

$$\partial_t(\rho \mathbf{v}) + (1-h)\,\nabla_x \cdot \left(p\mathrm{I} + \epsilon \mathrm{P}_1^{(1)} + \epsilon \mathrm{P}_2^{(1)}\right) + (1-h)\,\nabla_x \cdot (\mathbf{v} \otimes \mathbf{v}\rho) + (1-h)\,\nabla_x \cdot \mathrm{K}_2 = 0, \tag{4.75}$$

where

$$\begin{aligned}
\mathrm{P}_1^{(1)} =& -\frac{n_1 T}{\nu_1}\left((\nabla_x \otimes \mathbf{v}) + (\nabla_x \otimes \mathbf{v})^T - \frac{2}{3}(\nabla_x \cdot \mathbf{v})\,\mathrm{I}\right) + \frac{\nu_{11}}{\nu_1}T_{11}^{(1)}\,n_1\,\mathrm{I} + \frac{\nu_{12}}{\nu_1}T_{12}^{(1)}\,n_1\,\mathrm{I}\\
&+\frac{1}{\nu_1}s_1\mathrm{I} - \left\langle m_1\left(\mathbf{C}\otimes\mathbf{C} - \frac{1}{3}C^2\mathrm{I}\right)\mathbf{c}\cdot\nabla_x f_{1K}\right\rangle + \frac{1}{\nu_i}\left\langle m_i\,(\mathbf{C}\otimes\mathbf{C})\,\Delta_1\right\rangle,
\end{aligned} \tag{4.76}$$

$$\begin{aligned}
\mathrm{P}_2^{(1)} =& -\frac{n_2 T}{\nu_2}\left((\nabla_x \otimes \mathbf{v}) + (\nabla_x \otimes \mathbf{v})^T - \frac{2}{3}(\nabla_x \cdot \mathbf{v})\,\mathrm{I}\right) + \frac{\nu_{21}}{\nu_2}T_{21}^{(1)}\,n_2\,\mathrm{I} + \frac{\nu_{22}}{\nu_2}T_{22}^{(1)}\,n_2\,\mathrm{I}\\
&+\frac{1}{\nu_2}s_2\mathrm{I} - \left\langle m_2\left(\mathbf{C}\otimes\mathbf{C} - \frac{1}{3}C^2\mathrm{I}\right)\mathbf{c}\cdot\nabla_x f_{2K}\right\rangle + \frac{1}{\nu_i}\left\langle m_i\,(\mathbf{C}\otimes\mathbf{C})\,\Delta_2\right\rangle,
\end{aligned} \tag{4.77}$$

and the temperature corrections $T_1^{(1)}$ and $T_2^{(1)}$ are given by

$$T_1^{(1)} = -\frac{n_2}{n_1}\frac{1}{n^2}\frac{n_1\nu_{12}+n_2\nu_{21}}{\nu_{12}\nu_{21}}\left(s_1 - \langle m_1 C^2 \Delta_1\rangle\right) + \frac{1}{n^2}\frac{n_1\nu_{12}+n_2\nu_{21}}{\nu_{12}\nu_{21}}\left(s_2 - \langle m_2 C^2 \Delta_2\rangle\right),$$
$$T_2^{(1)} = \frac{1}{n^2}\frac{n_1\nu_{12}+n_2\nu_{21}}{\nu_{12}\nu_{21}}\left(s_1 - \langle m_1 C^2 \Delta_1\rangle\right) - \frac{n_1}{n_2}\frac{1}{n^2}\frac{n_1\nu_{12}+n_2\nu_{21}}{\nu_{12}\nu_{21}}\left(s_2 - \langle m_2 C^2 \Delta_2\rangle\right). \tag{4.78}$$

Plugging in the values for s_1 and s_2 according to Eq. Eq(4.67) produces:

$$\begin{pmatrix} T_1^{(1)} \\ T_2^{(1)} \end{pmatrix} = A\left(T\begin{bmatrix} \nabla_x \cdot K_{1,1} \\ \nabla_x \cdot K_{1,2} \end{bmatrix} - \frac{2}{3}\begin{bmatrix} H_{1K} \\ H_{2K} \end{bmatrix} + \begin{bmatrix} \langle mC^2\,\Delta_1\rangle \\ \langle mC^2\,\Delta_2\rangle \end{bmatrix}\right), \quad A = \frac{1}{n^2}\frac{n_1\nu_{12}+n_2\nu_{21}}{\nu_{12}\nu_{21}}\begin{bmatrix} n_2/n_1 & -1 \\ -1 & n_1/n_2 \end{bmatrix}. \tag{4.79}$$

Next, we solve for the the cross-species temperatures$T_{12}^{(1)}$ and see that,

$$T_{12}^{(1)} = T_{21}^{(1)} = \frac{n_1\nu_{12}T_1^{(1)} + n_2\nu_{21}T_2^{(1)}}{n_1\nu_{12}+n_2\nu_{21}} = \frac{n_1}{n^2}\left(\frac{\nu_{12}-\nu_{21}}{\nu_{21}\nu_{12}}\right)\left(s_2 - \langle m_2 C^2\Delta_2\rangle\right) + \frac{n_2}{n^2}\left(\frac{\nu_{21}-\nu_{12}}{\nu_{21}\nu_{12}}\right)\left(s_1 - \langle m_1 C^2\Delta_1\rangle\right). \tag{4.80}$$

Finally, the conservation of energy is:

$$\frac{3}{2}\partial_t(nT) + (1-h)\,\frac{3}{2}\nabla_x\cdot(nT\mathbf{v}) + (1-h)\,\mathrm{P}:(\nabla_x\otimes\mathbf{v}) + (1-h)\,\nabla_x\cdot\mathbf{q} + (1-h)\,(H_{1K}+H_{2K}) = 0, \tag{4.81}$$

where $\mathbf{q} = \epsilon(\mathbf{q}_1+\mathbf{q}_2)$, and

$$\mathbf{q}_i = \frac{5}{2}\frac{T}{m_i}\left(\rho_i\mathbf{V}_i + \frac{1}{\nu_i}\mathbf{J}_{iK} - \frac{n_i}{\nu_i}\nabla_x T\right) - \frac{1}{\nu_i}\left\langle\frac{m_i}{2}C^2\mathbf{C}(\mathbf{c}\cdot\nabla_x f_{iK})\right\rangle + \frac{1}{\nu_i}\langle\frac{m_i}{2}C^2\mathbf{C}\,\Delta_i\rangle, \tag{4.82}$$

$$\mathbf{J}_{iK} = \nabla_x\cdot\mathrm{K}_{2,i} - \mathbf{v}\,(\nabla_x\cdot\mathbf{K}_{1,i}). \tag{4.83}$$

In addition to the above equations, we also have to solve:

$$\partial_t f_{1K} + h\mathbf{c}\cdot\nabla_x f_{1K} + h\mathbf{c}\cdot\nabla_x f_{1F} = \epsilon^{-1}h\,Q_1[f], \tag{4.84}$$

$$\partial_t f_{2K} + h\mathbf{c}\cdot\nabla_x f_{2K} + h\mathbf{c}\cdot\nabla_x f_{2F} = \epsilon^{-1}h\,Q_2[f]. \tag{4.85}$$

Where $f_{iF} = f_i^{(0)}$ or $f_{iF} = f_i^{(0)} + \epsilon f_i^{(1)}$, depending on whether we are using the Euler or Navier-Stokes closure, respectively.

4.5 Numerical Results

4.5.1 Sod Shock Simulation

We begin the verification of our hybrid model with a simple 1D-1V single-species Riemann problem known as the Sod shock. This dimensionless test is defined by its left (L) and right (R) initial conditions for mass density, material velocity, and pressure: $\rho_L, u_L, p_L = [1, 0, 1]$ and $\rho_R, u_R, p_R = [0.125, 0.0, 0.1]$, respectively. Our hybrid approach combines a single species BGK model with no external field ($\mathbf{a} = 0$) and its Euler limit. The Euler model is implemented with a local Lax-Friedrichs scheme and the single species BGK model is implemented with an operator splitting approach, which disentangles the collisions from the phase space advection. We use a first order upwind stencil for phase space advection and a Crank-Nicholson stencil for the BGK collision terms. Because Crank-Nicholson is unconditionally stable, we set our time step based on the advection CFL condition. The McBGK model is directly derived from and tested against the MultiBGK code from [23].

We define the collision frequency for BGK using simple hard sphere scattering with

$$\nu = \pi R^2 n \sqrt{\frac{2k_b T}{m}}. \tag{4.86}$$

The non-dimensional parameter R is analogous to the radius of the hard spheres and allows us to tune the collision frequency in order to capture both kinetic and hydrodynamic regimes. Figure 4.2 shows a snapshot of the density and velocity at time $t = 1$ as obtained by the kinetic model for different values of R in comparison to the continuum solution. In general, the BGK calculation converges to the continuum result with increasing R. For $R = 1$, the collisionality is small enough that the BGK model produces diffusion. For $R = 25$ there is clear separation into rarefaction wave, contact discontinuity, and shock that are found in the Euler calculation. The simulation with $R = 5$ lies between the results with $R = 1$ and $R = 25$.

In the context of the Chapman-Enskog expansion, the non-dimensional Knudsen number can be defined as the ratio of the mean free path between collisions and a macroscopic reference scale. This definition quantifies the deviation of the distribution function f from the Maxwellian and

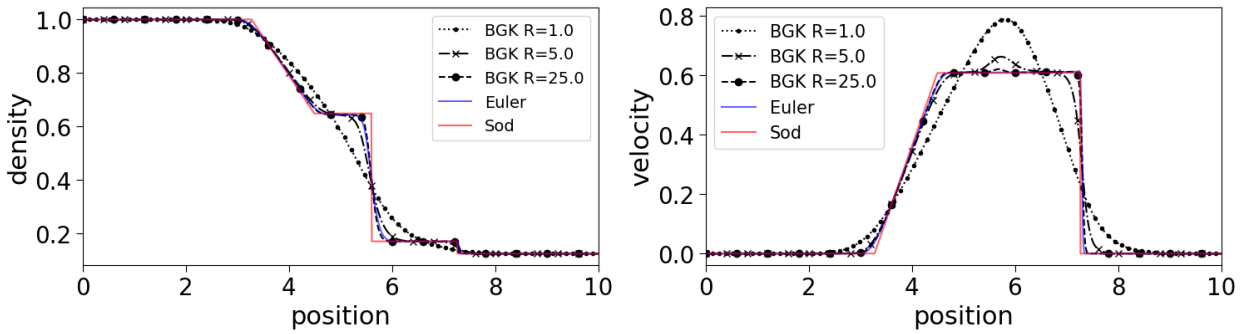

Figure 4.2 Snapshots of the density (left) and velocity (right) at time t = 1 as obtained by the kinetic model for different values of R. We increase collisionality by increasing the non-dimensional hard sphere radius R. As R increases, we recover the fluid limit. We emphasize that the Euler simulation matches the Sod analytic solution and that the BGK simulation converges to the Sod analytic solution in the large R (i.e. hydrodynamic) limit.

can be related to the expansion parameter ϵ in the Navier-Stokes closure. However, due to the ambiguity of choosing a macroscopic scale, we instead define two *effective* Knudsen numbers to quantify the deviation from a Maxwellian. We are able to do this since we have access to the underlying distribution functions as part of our hybrid model. The effective Knudsen numbers are defined as

$$Kn_1 = \frac{1}{n}\int dc\ |\mathcal{M}[f] - f|, \tag{4.87}$$

$$Kn_2 = 1 - \frac{\langle v^4 \rangle}{3\langle v^2 \rangle^2}, \tag{4.88}$$

where $\mathcal{M}[f]$ is the Maxwellian in Eq. Eq(4.2) that is associated with the moments of f. The value of Kn_1 quantifies the absolute deviation of f in phase space from its associated Maxwellian, while Kn_2 characterizes the deviation of the distribution function's 4^{th} moment from the one predicted by M [24]. In both cases, a value of zero indicates that f is a Maxwellian distribution. In Figure 4.3, we plot the local values of Kn_1 and Kn_2 for the Sod problem and different BGK collisionalities. As expected, both Knudsen numbers generally decrease for larger collision frequencies. Note that at the shock front and the contact discontinuity, Kn_1 and Kn_2 show persistent peaks. This signals that kinetic behavior is important around such sharp features in the Euler solution. Furthermore the left side of the domain, which contains the fluid and buffer regions, has relatively small Knudsen numbers which shows that this is a good choice for their placement.

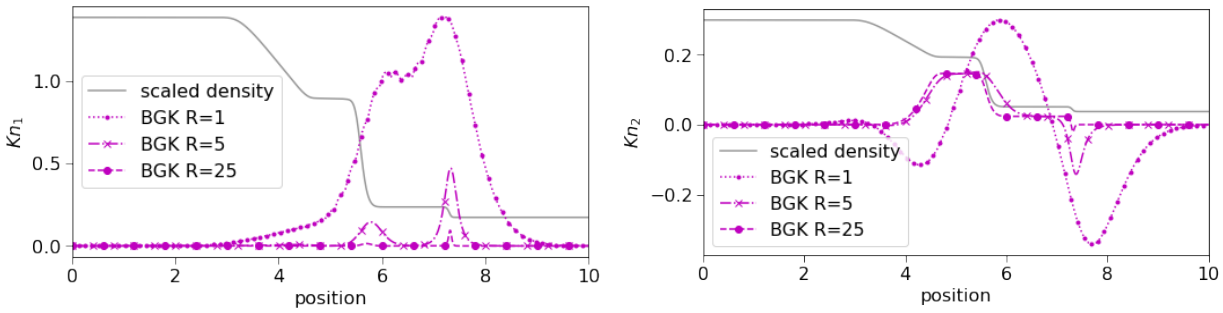

(a) Knudsen number Kn_1 according to Eq. Eq(4.87) (b) Knudsen number Kn_2 according to Eq. Eq(4.88)

Figure 4.3 Estimates of the deviation from equilibrium for different collisionalities via the Knudsen number definitions in Eqn. Eq(4.87) and Eq(4.88), varied via the nondimensional particle radius R, for the Sod problem. For reference, we also plot the (scaled) density profile of the Euler solution. Left: effective Knudsen number via integrated deviations from Maxwellian, see Eq. Eq(4.87). Right: effective Knudsen number via moment ratio, see Eq. Eq(4.88). Both models for the effective Knudsen number show that the deviation from a Maxwellian is greatest near the the shock.

In Figure 4.4, we plot the hybrid model which couples kinetic dynamics with $R = 1$ to its associated Euler model. In the left pane we show, if the buffer region is correctly placed then the hybrid model produces an equivalent result as the BGK model without using kinetic dynamics over the entire physical domain. Here 'correctly placed' means that the buffer region is placed where the Knudsen number is near zero. In other words, where the hydrodynamic description is valid. In the right pane we show, if the buffer region is incorrectly placed in a part of the domain where kinetic effects are still important, then we suppress the kinetic phenomena. Here 'incorrectly placed' means that the kinetic dynamics are NOT used where the Knudsen number was shown to be large. In effect, we have assumed that the continuum approximation applies where it actually does not. As a consequence, even in the buffer region, the hybrid model largely resembles the hydrodynamic density pattern. Only at around $x = 6.5$ it finally begins to reproduce the density curve of the BGK calculation. This demonstrates that the buffer region should be placed sufficiently far away from regions with kinetic phenomena such as shock fronts and material interfaces. Of course, we want to place the buffer region to define the smallest kinetic region possible. Additionally, the kinetic and hydro models are run in the buffer region it more expensive than either. In our study of buffer width, we recovered nothing substantively different than what is presented in Degond et al.'s study [1] of the 1-D SOD shock solution.

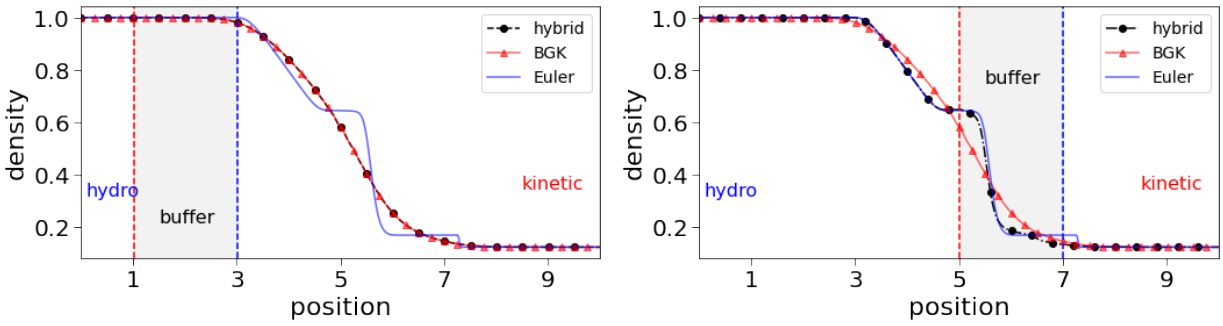

Figure 4.4 Sod problem with $R = 1$. Left: the kinetic-hydro buffer region is placed in the space interval $[1, 3]$, i.e. away from the shock. Right: the buffer region is placed in $[5, 7]$, i.e., around the shock. Since the coupled model is derived for a system near equilibrium, this assumption is imprinted in the buffer region. While in the left plot, the coupled model correctly follows the kinetic and continuum solutions where appropriate, in the right plot, it tracks the hydrodynamic solution and only transitions to the reference kinetic solution near the edge of the buffer region.

However, it is important to remember that here we zoom into the shock area. In a real physics setup that is targeted by the kinetic-hydro approach, such a shock would occupy a relatively small region with the hydrodynamic regime dominating the simulation volume.

4.5.2 MARBLE pore preheat problem

To demonstrate the multi-species modeling capabilities of our hybrid approach we simulate an experimental setup that was designed to measure the amount of mix in ICF-type implosions. The MARBLE campaign sought to quantify mixing by using separated reactants in ICF capsules and examining the thermonuclear burn output [17]. Instead of a typical capsule, MARBLE used a deuterated plastic foam studded with pores. The pores were filled with a gas containing tritium (see Figure 4.5). In this chapter, we are focusing the qualitative macro pore collapse; therefore we only consider the HT gas in macro pores and do not consider HT gas in any CD micro-pores. While we do not expect the additional tritium in the micropores to significantly affect the macropore dynamics studied here, one would need to include this in a larger capsule simulation that estimates the total yield. Since the deuterium and tritium start separated, then DD vs DT yield is a diagnostic tool for the amount of mix. The initial experiments found that varying the pore sizes showed little of the expected effect. It is proposed that the capsule's preheat phase left the separated reactants more mixed than predicted by simulations. These simulations were done using hydrodynamic codes

Material	Location	Number density [1/cc]	density [1/cc]	Ionization Level
Deuterium	Foam	3.61×10^{21}	1.20×10^{-2}	full
Carbon	Foam	3.61×10^{21}	7.22×10^{-2}	4 electrons ionized
Hydrogen	Pore	8.80×10^{20}	1.47×10^{-3}	full
Tritium	Pore	1.15×10^{20}	5.77×10^{-4}	full

Table 4.1 Material location, number densities, densities, and ionization levels in the MARBLE preheat problem

which only considered mixing from fluid instabilities or turbulence. Since these results have been released, others have shown that non-equilibrium effects can play a role in the mix morphology of the D and T ions in the preheat stages of the experiment. In particular, preheat mixing of the pores may have a strong effect on the DT fusion yield [18, 25, 26]. This emphasizes the need to include kinetic dynamics in the simulations.

With that, we simulate a simplified model of a single MARBLE pore using the hybrid method in 1D and planar geometry. We note that this choice of dimensionality will suppress certain kinds of hydrodynamic instabilities and emphasize the atomic mixing. However, it is a reasonable initial demonstration of our coupled method. Follow-up studies may explore simulation setups in 2D or 3D along with more precise computational cost studies. Here, we assume that the material is initially at rest with a 50 eV background temperature, which is a reasonable facsimile of the preheat conditions before shock arrival. The initial number densities and densities for the carbon-deuterium (CD) foam and hydrogen-tritium (HT) pore gas are given in Table 4.1. The background preheating will expand the foam thereby compressing the gas in the pore. With that, atomic mixing is likely to occur at the foam/gas interface. Based on the findings in the Sod test, we expect that kinetic dynamics will be necessary to model the interfaces during pore compression. A transition function $h(x)$ and its associated hydrodynamic and kinetic regions are plotted in Figure 4.6. This transition function places the pore and the interfaces within the kinetic region and places the buffer regions in the foam which are expected to be hydrodynamic. Due to the high temperature of the experiment, we include electric fields via the amipolar approximation in both the kinetic and fluid models. For the Euler model, this results in an additional term in the momentum equation:

$$\partial_t \ (\rho u) = \nabla \ \left(\rho u^2 + (n + n_e) \ k_b T \right). \tag{4.89}$$

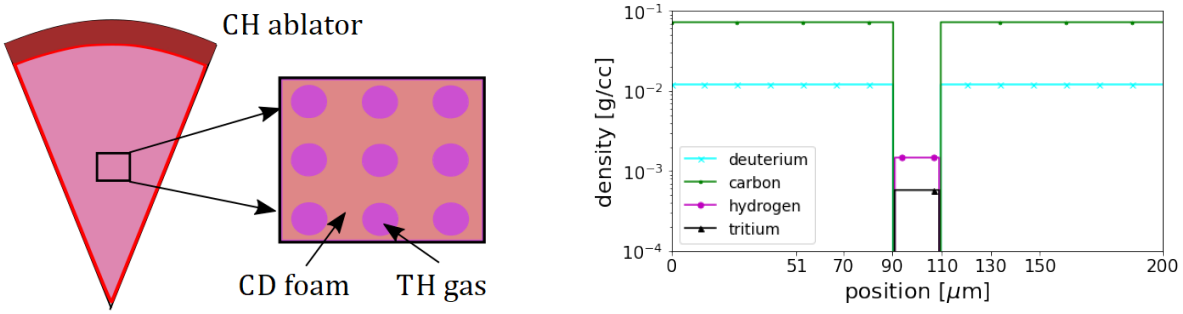

Figure 4.5 Left: Illustration of the Marble-type foam which is studied in this chapter. Orange represents the CD foam while the purple disks represent the macro-pores that are filled with TH gas. Note that the CD foam also contains many smaller micro-pores; for the purpose of this study we consider the foam region to be a homogenous CD material. Right: Initial densities used in the 1D planar MARBLE pore preheat problem (see Sec. (4.5.2)). We simulate a 200μm slice of carbon-deuterium foam with a 20μm hydrogen-tritium pore located at the center.

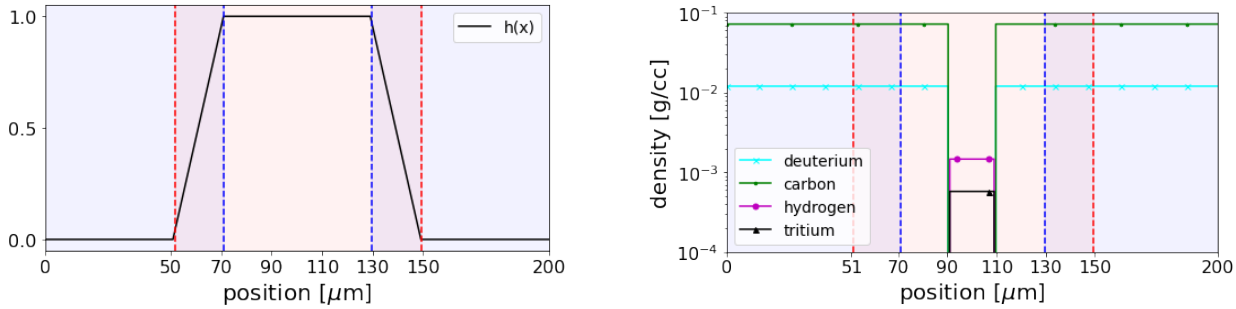

Figure 4.6 Left: Transition function $h(x)$ for the MARBLE pore preheat problem (Sec. 4.5.2). The edges of the buffer regions are indicated by the dashed lines. Right: Material densities together with the edges of the buffer regions. Due to the sharp interfaces which define the pore, we expect kinetic effects to be important around the pore. To ensure our assumption that the buffer region is placed in a hydrodynamic region is satisfied, we place the buffer edges away from where we expect shock fronts (*i.e* in the foam).

For the kinetic equations we include a Vlasov term:

$$\mathbf{a} = \frac{eE}{m} = -\frac{1}{m\, n_e} \nabla\, n_e T. \tag{4.90}$$

We focus on the simulation results for deuterium and tritium. Other species are still present, but we plot the two species of greatest interest for clarity of presentation We start with Figure 4.7, which shows the full time evolution of the deuterium and tritium densities as a heat map, simulated with the BGK, hybrid, and Euler methods. This figure, along with the equivalent figure plotting the hydrodynamic velocities, Figure 4.9, are the major results for the MARBLE pore preheat example problem. Similar to Figure 4.4 for the Sod shock, these plots demonstrate that the hybrid model can

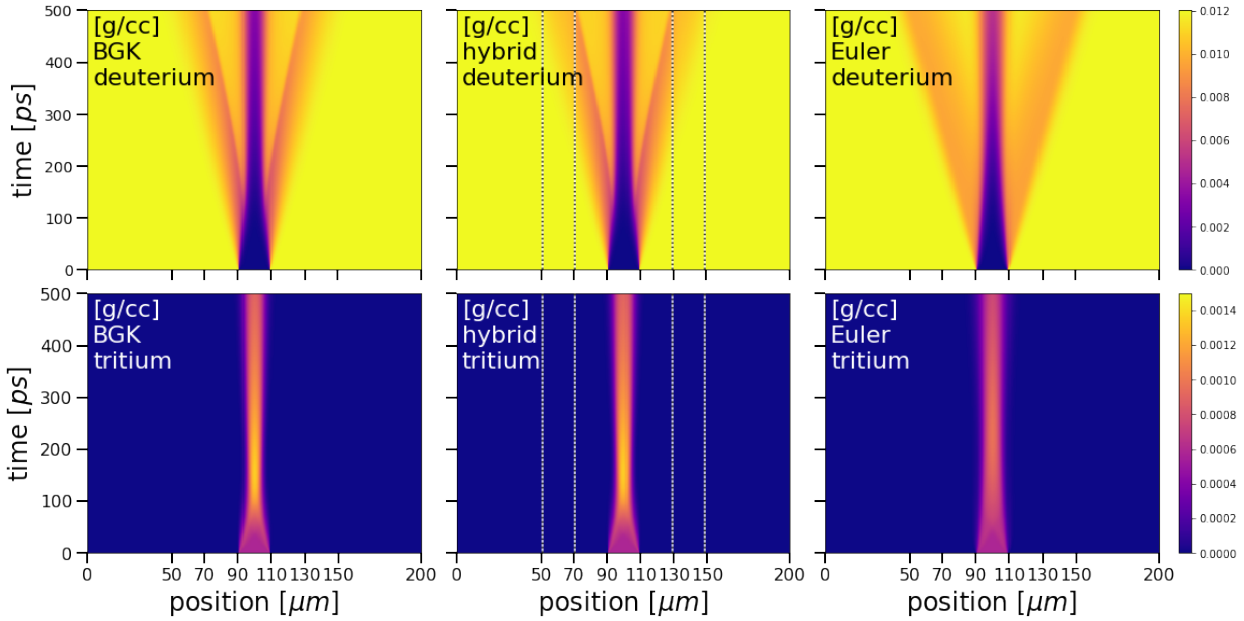

Figure 4.7 Evolution of the material densities as compared across models for the MARBLE pore preheat problem (Sec. 4.5.2). Each heat map has time evolution on vertical axis and spatial position on the horizontal axis. In the hybrid simulation, we visualize the buffer region as dashed lines. Note that initial conditions plotted in Figure 4.6 Right are a cross section from the heat map at time 0ps. The top row shows the deuterium in the foam while the bottom row gives the evolution of the tritium densities. The left to right columns correspond to the BGK, hybrid, and Euler methods. For every model, these heat maps show that the pore is compressed for approximately 150ps as the foam/pore expands. For the Euler model the compression is not nearly as great as the others. Eventually the pore is compressed enough to trigger a rarefaction wave. This rarefaction wave looks sharpest for the BGK and hybrid model because the compression of the pore was greatest.

replicate a full kinetic simulation without needing kinetic dynamics in all physical regions of the simulation. The remainder of the section is dedicated to exploring and understanding the dynamics which kinetic models include.

In the first few picoseconds of the simulation, there are very large electric fields at the pore interface, which rapidly diminish greatly by 10 picoseconds. This is shown in Figure 4.8. Such behavior matches results from atomistic interface simulations, as presented by Stanton et al. [10]. Depending on the model (*i.e.* BGK, hybrid, Euler) the electric field has different effects on the velocity profiles. As with the density evolution, the velocity profiles for kinetic and hybrid models agree. Furthermore, they have significant differences with the continuum calculation. To see this, examine the evolution of the velocity profiles for D and T across models in Figure 4.9. The figure

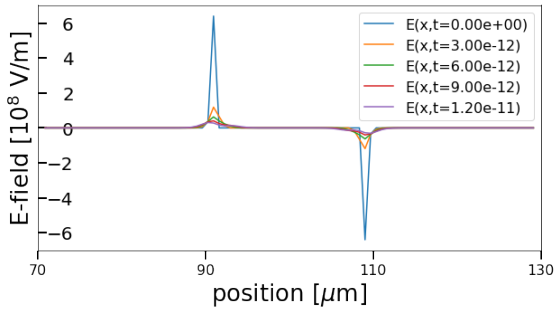

Figure 4.8 Electric field profiles at early times in the MARBLE pore preheat problem. The electric fields evolution for the kinetic model (BGK) and Euler model are indistinguishable so only BGK is presented here. The strong electric fields accelerate positively charged HT ions The constituents of the plasma quickly redistribute to diminish the electric fields. (*i.e.* less than 10 ps)

shows that the electric fields in the BGK and hybrid models accelerate some tritium (and hydrogen) particles to large velocities and eject them into the foam. This separate, electric field induced mixing is possible because the BGK and hybrid models allow each species to have individualized velocity fields around the pore region, while the Euler model enforces a common bulk velocity among all species over the entire physical domain. Two important conclusions arise. First, since the tritium velocity profile differs from the mixture bulk velocity, which is used as the reference equlibrium velocity assumed in the hydroynamic approximation; this these ejected particles are not an equilibrium phenomenon. Second, because the Euler solution's bulk velocity is not affected by the electric field, we can conclude that the proportion of the mass density comprised by the TH ejecta is negligible.

Next, we investigate how the ejecta, which violate the assumptions made when placing the buffer regions, did not corrupt the simulation. In Figure 4.10, we plot Kn_1 for the four species in the simulation at 20 ps. This is 10 ps after the electric field has reduced and the pore ejecta are traveling through the foam. We overlay the species density and see that a negligible amount of hydrogen and tritium were ejected from the pore into the foam. In Figure 4.11, we plot the evolution of tritium's effective Knudsen number Kn_1 throughout the simulation as a heat map. First, notice that the tritium Knudsen plot from Figure 4.10 (Bottom Right) is a horizontal cross section of the BGK evolution in Figure 4.11 (Left) at time 20ps. Second, notice for the the BGK evolution in Figure 4.11 (Left) that for all times the high Knudsen numbers exist in a region where number

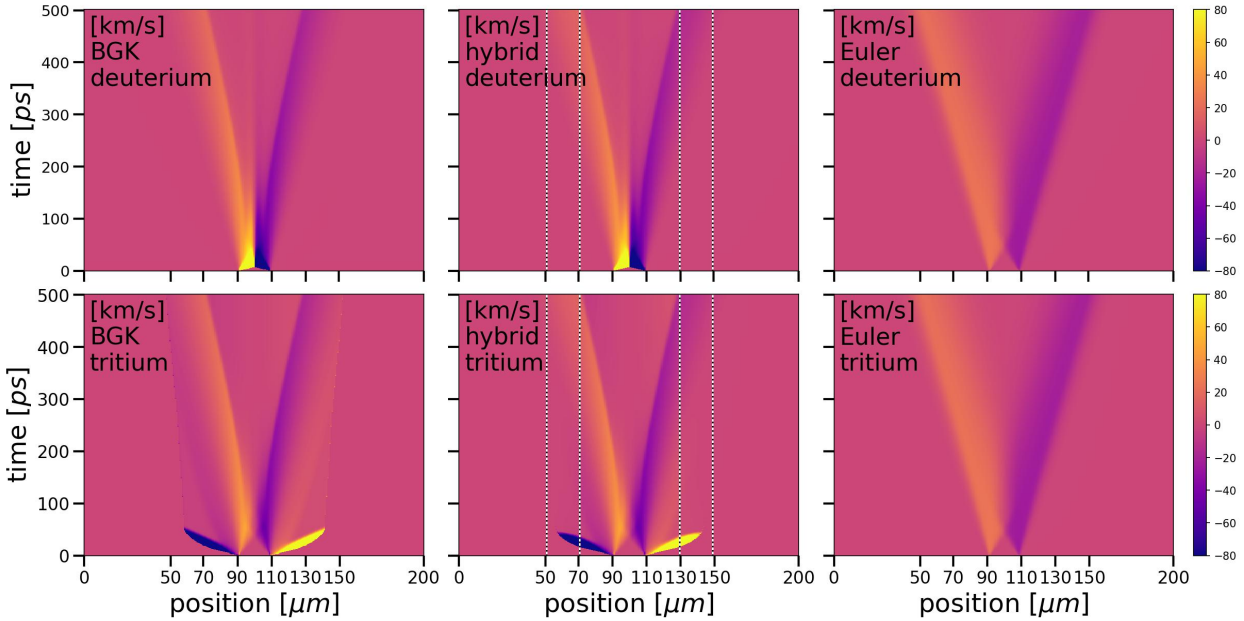

Figure 4.9 Time evolution of the velocity profiles in the MARBLE pore preheat problem. The top row shows the velocity in the deuterium foam material, while the bottom row gives the velocities in the pore tritium. The left to right columns correspond to the BGK, hybrid, and Euler solutions. Since the hydrodynamic model assumes a single velocity, the deuterium and tritium are both propelled inward. In the kinetic and hybrid models, however, the tritium distribution shows an additional velocity jet at early times which corresponds to a very small amount of tritium ejected from the pore by the electric field at a large velocity. Furthermore, tritium ions show a non-zero velocity field beyond the edges of the pore (90μm - 100μm). This is due to the few ejected ions which have been sprinkled throughout the CD foam. Note that for display purposes, the maximum velocity in the color map is set to ±80 km/s to ensure a representative color map on the region of interest; the velocities in the ejection 'plumes' typically exceed ±200 km/s.

density is less than 1 particle per cc. Therefore, even though the ejecta have a high Knudsen number they are rarefied enough to not corrupt our assumption that the foam is hydrodynamic. Additionally, notice in the hybrid evolution in Figure 4.11 (Center) that the choice of the buffer location can impact the hybrid solution when compared to the reference kinetic model. This matches what was seen in the Sod shock, in Figure 4.4. Indeed, the ejecta are forcibly equilibrated to the local Maxwellian of the mixture, and any deviation from mixture velocity and temperature is lost (*i.e.* ejecta are brought to a halt and never enter the hydrodynamic region). As with BGK, the curve for 1 particle per cc indicates that the number density is again small enough to find this spurious halting irrelevant.

Now consider the rarefaction wave which exists in the time range of 100 picoseconds and beyond

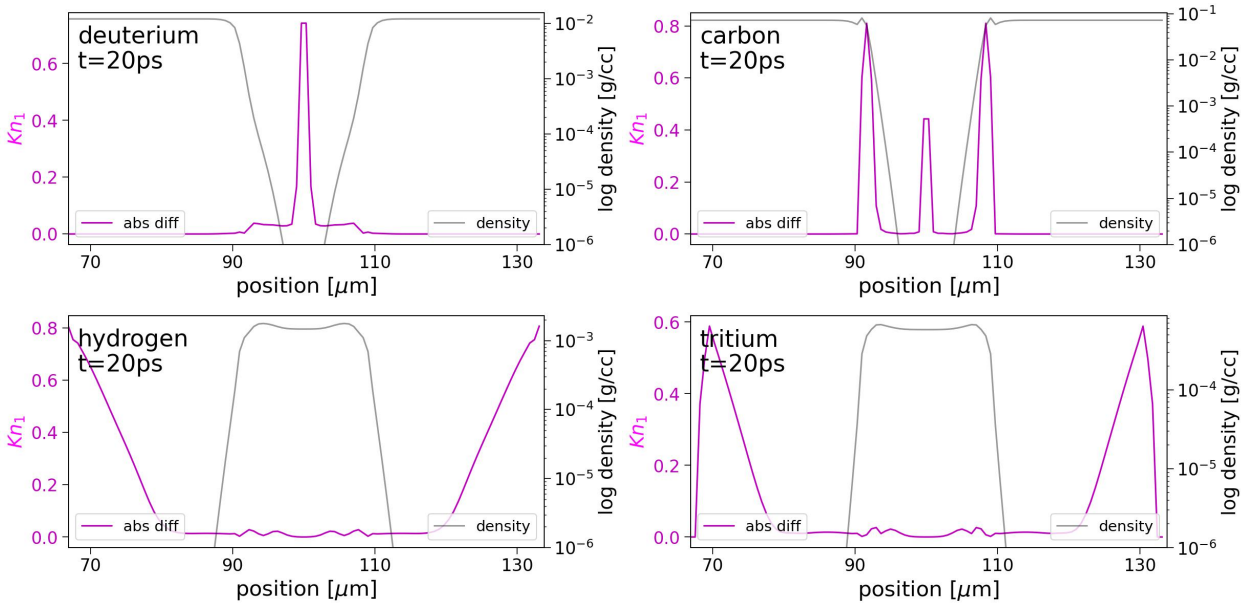

Figure 4.10 Comparison of effective Knudsen number Eq(4.87) across species for the MARBLE pore preheat problem, at time 250ps. The (rescaled) density profile is shown in the background for reference. As expected, the effective Knudsen number is larger in carbon and deuterium where there rapid changes in density, i.e., where the gradient scale length is small. Additionally, the tritium and hydrogen ejections produce a large Knudsen number which travels into the buffer region (*i.e.* $[50, 70]$ and $[130, 150]$). However the associated densities are negligible. Thus, the hydrodynamic model does not cause the hybrid results to differ from the BGK results.

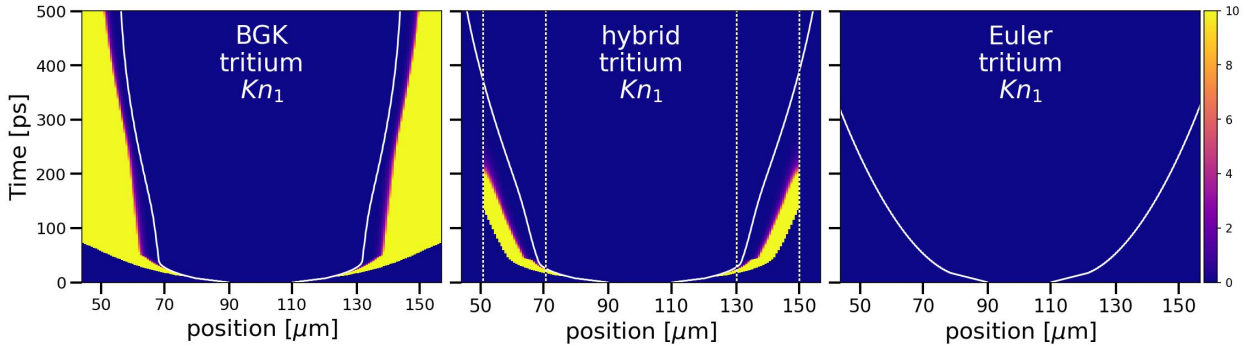

Figure 4.11 Plots of the effective Knudsen number Kn_1 for BGK, hybrid, and Euler solutions of the Marble preheat problem. For reference we have added a solid white contour which marks where the material number density is less that 1 particle per cc. The minuscule amount of particles ejected by the strong interface electric fields carry high Knudsen values as they propagate through the foam until they collide with each other on the periodic boundary conditions. As can be seen by Kn_1 in the buffer region for the hybrid method, the transition to Euler in the buffer region suppresses the high speed, uncollided ejected particles from penetrating further into the foam. In both cases, the contour indicates that the high Knudsen values occur where a negligible amount of particles exist. Thus, the Knudsen number of the ejecta does not corrupt our hydrodynamic assumptions.

in this section's main result, Figure 4.7. Right around peak compression, at approximately 150ps, a rarefaction wave forms in all models. The propagation of this rarefaction wave constitutes the remainder of the simulation. For the following discussion of this rarefaction wave it is important to notice that the BGK and hybrid model lead to a stronger compression of the pore material. This is visualized by the brighter, thinner width of the pore. In Figure 4.12 we plot the density profiles (*i.e.* cross sections from Figure 4.7) at 250ps, 375ps, and 500ps. These cross sections emphasize the form of the rarefaction wavefront as it propagates through the deuterium. As well as, the expansion of the tritium as the rarefaction wave propagates. For 250ps and 375ps, kinetic and hybrid models share the same form of the wavefront, but differ from the Euler model. It is the higher compression attained in the kinetic and hybrid models which leads them to have sharper rarefaction wave fronts than the Euler model. In the deuterium cross section at 500ps, we see that rarefaction has propagated into the hydrodynamic region. At this point, the BGK and hybrid model differ from each other. This behavior indicates that the hybrid model differs from BGK because our assumptions that f can be approximated by a Maxwellian has broken down and we are artificially suppressing kinetic phenomena. This behavior was studied in the Sod problem in Figure 4.4. As before, the Eulerian contribution to the coupled solution is forcing the wave front to be less diffusive (*i.e.* more sharp). This is an important sanity check.

Note that the Euler equations, as defined by the zeroth order Chapman-Enskog expansion, require all species share same bulk velocity and bulk temperature. Allowing one or more species to deviate from this would violate this definition of the Euler equation. If we violate the definition of Euler then this flexibility would be possible, but the scheme would not be consistent. We believe this species separation along with an adaptive buffer region are both needed for large scale projects, but creating this separation is beyond the scope of this dissertation and will be the subject of future work.

4.6 Summary and outlook

We have presented a hybrid model for coupling the multispecies Bhatnagar-Gross-Krook (BGK) kinetic model with their limiting Euler and Navier-Stokes hydrodynamic equations. The hybrid

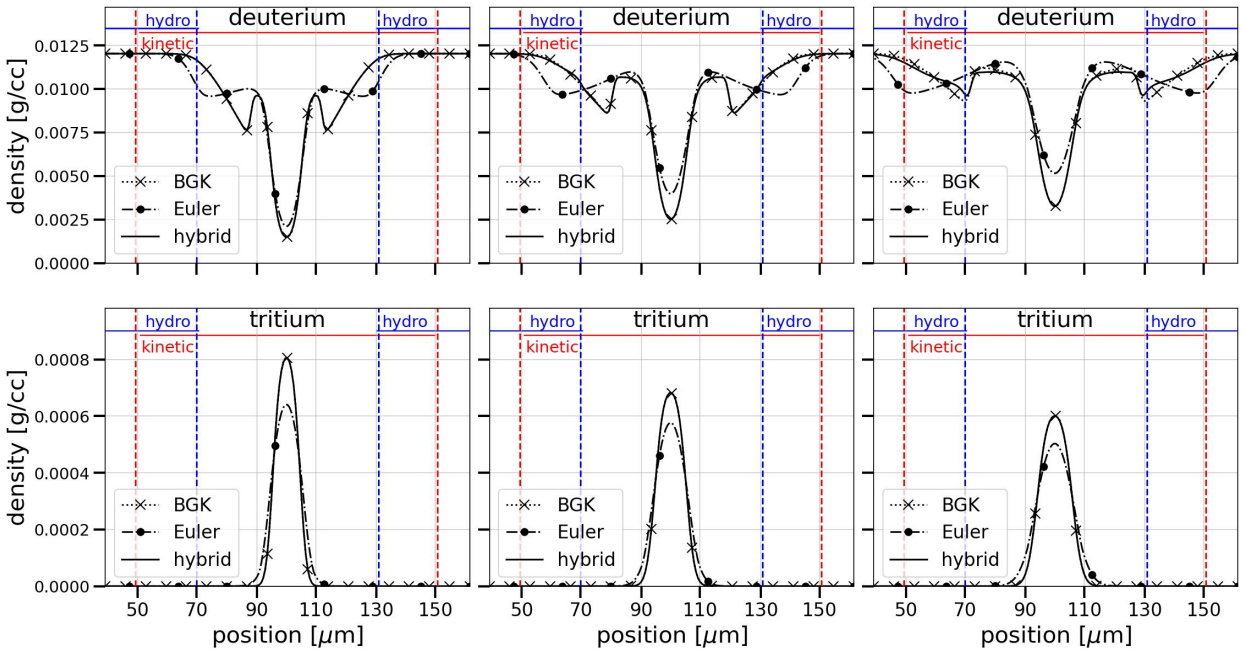

Figure 4.12 Each plot contains BGK, hybrid, and Euler density curves for a different species and time. The rows separate deuterium (top) and tritium (bottom) density profiles. From left to right, the plots are 250ps, 375ps, and 500ps. The top row illustrates the propagation of the rarefaction wave through the foam. The bottom row illustrates the expansion of the pore after peak compression. The rarefaction wave enters the buffer zone at around 500ps. We can see that a difference emerges between the coupled model and BGK after that time. The difference indicates that our assumption that tritium's distribution function is at local equilibrium around the wavefront is incorrect and we are therefore artificially suppressing kinetic dynamics.

model is not merely a weighted average of independent kinetic and hydrodynamic calculations with the same initial conditions. Rather, the hybrid model is the simultaneous evolution of the two models coupled together. Our technique uses a buffer region to impose meaningful boundary conditions when modeling the transition from a kinetic into a fluid region, generalizing the single species approach introduced by Degond et al. (see e.g. [1]). In the buffer region, both the kinetic and hydrodynamic equations are solved simultaneously, and the solution to the hybrid model is a weighted sum of the solutions to the coupled models. The smooth transition between models avoids the need to find direct interface conditions, which can introduce unphysical effects in hydrodynamic regions. Kinetic models, while expensive due to their dimensionality, are able to capture important multispecies physics effects such as velocity and temperature separation. This hybrid method allows one to localize the use of a high dimensional kinetic model only where it is needed, therefore

maximizing the computational efficiency. We validated our model with simple Sod shock problem example and then applied the method to study the effect of kinetic multispecies mixing in the preheat phase of a high energy-density physics experiment. We demonstrated that if the buffer regions are placed correctly the hybrid model can produce kinetic simulations without needing kinetic dynamics over the entire physical domain.

One advantage of this approach is that a direct mesh decomposition is not needed; especially in higher spatial dimensions, the transition function can take care of any potentially geometric features of the interface. Similarly the transition function could be modified to take dynamically evolution of the kinetic region into account; see [2]. This will be the subject of future work.

Acknowledgement

Thomas Chuna would like to acknowledge F.D.C. Willard for insightful discussions and proof reading. This work was supported by the U.S. Department of Energy through the Los Alamos National Laboratory. Los Alamos National Laboratory is operated by Triad National Security, LLC, for the National Nuclear Security Administration of U.S. Department of Energy (Contract No. 89233218CNA000001). Research presented in this article/presentation/report was supported by the Laboratory Directed Research and Development program of Los Alamos National Laboratory under project number 20190005DR.

BIBLIOGRAPHY

[1] Pierre Degond, Shi Jin, and Luc Mieussens. A smooth transition model between kinetic and hydrodynamic equations. *Journal of Computational Physics*, 209(2):665 – 694, 2005.

[2] Pierre Degond, Giacomo Dimarco, and Luc Mieussens. A moving interface method for dynamic kinetic-fluid coupling. *Journal of Computational Physics*, 227(2):1176 – 1208, 2007.

[3] P. Degond, J. Liu, and L. Mieussens. Macroscopic fluid models with localized kinetic upscaling effects. *Multiscale Modeling & Simulation*, 5(3):940–979, 2006.

[4] Pierre Degond, Giacomo Dimarco, and Luc Mieussens. A multiscale kinetic fluid solver with dynamic localization of kinetic effects. *Journal of Computational Physics*, 229(13):4907 – 4933, 2010.

[5] Pierre Degond and Giacomo Dimarco. Fluid simulations with localized boltzmann upscaling by direct simulation monte-carlo. *Journal of Computational Physics*, 231(6):2414 – 2437, 2012.

[6] G. Dimarco and L. Pareschi. Numerical methods for kinetic equations. *Acta Numerica*, 23:369–520, 2014.

[7] Andrew Ho, Iman Anwar Michael Datta, and Uri Shumlak. Physics-based-adaptive plasma model for high-fidelity numerical simulations. *Frontiers in Physics*, 6, 2018.

[8] H. Rinderknecht, P. Amendt, S. Wilks, and G. Collins. Kinetic physics in icf: present understanding and future directions. *Plasma Physics and Controlled Fusion*, 60(6):099601, 2018.

[9] S. Le Pape, L. Divol, G. Huser, J. Katz, A. Kemp, J. S. Ross, R. Wallace, and S. Wilks. Plasma collision in a gas atmosphere. *Phys. Rev. Lett.*, 124:025003, Jan 2020.

[10] L. G. Stanton, J. N. Glosli, and M. S. Murillo. Multiscale molecular dynamics model for heterogeneous charged systems. *Phys. Rev. X*, 8:021044, May 2018.

[11] Jeffrey R. Haack, Cory D. Hauck, and Michael S. Murillo. Interfacial mixing in high-energy-density matter with a multiphysics kinetic model. *Phys. Rev. E*, 96:063310, Dec 2017.

[12] W Bang, BJ Albright, PA Bradley, DC Gautier, S Palaniyappan, EL Vold, MA Cordoba, CE Hamilton, and JC Fernández. Visualization of expanding warm dense gold and diamond heated rapidly by laser-generated ion beams. *Scientific reports*, 5(1):1–7, 2015.

[13] L. F. Berzak Hopkins, S. Le Pape, L. Divol, N. B. Meezan, A. J. Mackinnon, D. D. Ho, O. S. Jones, S. Khan, J. L. Milovich, J. S. Ross, P. Amendt, D. Casey, P. M. Celliers, A. Pak, J. L.

Peterson, J. Ralph, and J. R. Rygg. Near-vacuum hohlraums for driving fusion implosions with high density carbon ablators. *Physics of Plasmas*, 22(5):056318, 2015.

[14] Drew P Higginson, DJ Strozzi, D Bailey, SA MacLaren, NB Meezan, SC Wilks, and G Zimmerman. Understanding and controlling capsule symmetry in near vacuum hohlraums at the national ignition facility. *Physics of Plasmas*, 29(7):072714, 2022.

[15] J. R. Rygg, J. A. Frenje, C. K. Li, F. H. Séguin, R. D. Petrasso, J. A. Delettrez, V. Yu Glebov, V. N. Goncharov, D. D. Meyerhofer, S. P. Regan, T. C. Sangster, and C. Stoeckl. Tests of the hydrodynamic equivalence of direct-drive implosions with different d2 and he3 mixtures. *Physics of Plasmas*, 13(5):052702, 2006.

[16] D. T. Casey, J. A. Frenje, M. Gatu Johnson, M. J.-E. Manuel, H. G. Rinderknecht, N. Sinenian, F. H. Séguin, C. K. Li, R. D. Petrasso, P. B. Radha, J. A. Delettrez, V. Yu Glebov, D. D. Meyerhofer, T. C. Sangster, D. P. McNabb, P. A. Amendt, R. N. Boyd, J. R. Rygg, H. W. Herrmann, Y. H. Kim, and A. D. Bacher. Evidence for stratification of deuterium-tritium fuel in inertial confinement fusion implosions. *Phys. Rev. Lett.*, 108:075002, Feb 2012.

[17] T J Murphy, M R Douglas, J R Fincke, R E Olson, J A Cobble, B M Haines, C E Hamilton, M N Lee, J A Oertel, N A G Parra-Vasquez, R B Randolph, D W Schmidt, R C Shah, J M Smidt, and I L Tregillis. Progress in the development of the MARBLE platform for studying thermonuclear burn in the presence of heterogeneous mix on OMEGA and the national ignition facility. *Journal of Physics: Conference Series*, 717:012072, may 2016.

[18] B. J. Albright, T. J. Murphy, B. M. Haines, M. R. Douglas, J. H. Cooley, T. H. Day, N. A. Denissen, C. Di Stefano, P. Donovan, S. L. Edwards, J. Fincke, L. M. Green, L. Goodwin, R. A. Gore, M. A. Gunderson, J. R. Haack, C. E. Hamilton, E. P. Hartouni, N. V. Kabadi, S. Khan, P. M. Kozlowski, Y. Kim, M. N. Lee, R. Lester, T. Morrow, J. A. Oertel, R. E. Olson, B. M. Patterson, T. Quintana, R. B. Randolph, D. W. Schmidt, R. C. Shah, J. M. Smidt, A. Strickland, C. Wilson, and L. Yin. Experimental quantification of the impact of heterogeneous mix on thermonuclear burn. *Physics of Plasmas*, 29(2):022702, 2022.

[19] B.M. et al. Haines. Observation of persistent species temperature separation in inertial confinement fusion mixtures. *Nature Communications*, 11, 2020.

[20] Rick Olson, Brian Haines, Yongho Kim, Lauren Green, Derek Schmidt, and Brian Albright. Design of a direct-drive experimental platform for exploring the effects of heterogeneous mix on fusion burn. *Bulletin of the American Physical Society*, 2022.

[21] Jeffrey R. Haack, Cory D. Hauck, and Michael S. Murillo. A conservative, entropic multispecies bgk model. *Journal of Statistical Physics*, 168(4):826–856, Aug 2017.

[22] S. Chapman and T.G. Cowling. *The Mathematical Theory of Non-uniform Gases: An Account of the Kinetic Theory of Viscosity, Thermal Conduction, and Diffusion in Gases*. Cambridge University Press, 1958.

[23] Jeffrey R Haack, Cory D Hauck, and Michael S Murillo. Interfacial mixing in high-energy-density matter with a multiphysics kinetic model. *Physical Review E*, 96(6):063310, 2017.

[24] R. Sprenkle, L. Silvestri, M. Murillo, and S. Bergeson. Temperature relaxation in strongly-coupled binary ionic mixtures. *Nature Communications*, 13(15), 2022.

[25] P. Brady, J. H. Cooley, A. Diaw, J. Haack, and D. Livescu. Examination of the marble initial conditions due to preheat, in prep.

[26] L. Yin, B. J. Albright, E. L. Vold, W. D. Nystrom, R. F. Bird, and K. J. Bowers. Plasma kinetic effects on interfacial mix and burn rates in multispatial dimensions. *Physics of Plasmas*, 26(6):062302, 2019.

APPENDIX 4A

COMPUTING THE FLUID CORRECTION $f_{iF}^{(1)}$ IN BUFFER REGION

For the convenience of the reader we group the definitions which will be frequently used in this section:

$$\frac{3}{2}n_i T \equiv \left\langle \frac{m_i}{2} C^2 \, f_{iF} \right\rangle, \quad \nabla_x \cdot \mathbf{q}_i \equiv \nabla_x \cdot \left\langle \frac{m_i}{2} C^2 \mathbf{C} \, f_{iF} \right\rangle, \tag{4A.1}$$

$$\mathbf{K}_{1,i} \equiv \langle m_i \, \mathbf{c} \, f_{iK} \rangle, \quad \mathrm{K}_{2,i} \equiv \langle m_i \, (\mathbf{c} \otimes \mathbf{c}) f_{iK} \rangle, \quad \mathbf{K}_3 \equiv \left\langle \frac{m_i}{2} \, \mathbf{c} \, c^2 \, f_{iK} \right\rangle, \tag{4A.2}$$

$$\mathbf{J}_K \equiv \sum_i \mathbf{J}_{iK} \equiv \sum_i \nabla_x \cdot \mathrm{K}_{2,i} - \mathbf{v} \, (\nabla_x \cdot \mathbf{K}_{1,i}), \tag{4A.3}$$

$$H_K \equiv \sum_i H_{iK} \equiv \sum_i \left\langle \frac{m_i}{2} C^2 \, (\mathbf{c} \cdot \nabla_x f_{iK}) \right\rangle, \tag{4A.4}$$

We start from Eq. 4.55, rewritten here for convenience.

$$\begin{aligned} &\partial_t f_{iF}^{(0)} - \mathrm{D}_t \left(\mathbf{v} \cdot \nabla_{\mathbf{C}} f_{iF}^{(0)} \right) + (1-h)(\mathbf{C} + \mathbf{v}) \cdot \nabla_x f_{iF}^{(0)} \\ &\quad - (1-h)(\mathbf{C} \otimes \nabla_{\mathbf{C}} f_{iF}^{(0)}) : (\nabla_x \otimes \mathbf{v}) + (1-h) \, \mathbf{c} \cdot \nabla_x f_{iK} = (1-h) Q_i^{(1)}[f_{iF}] + (1-h)\Delta_i. \end{aligned} \tag{4A.5}$$

4A.1 Computing the $f_{iF}^{(0)}$ terms

We begin by focusing on reformulating the left hand side of Eq(4A.5) in terms of n_i, $\mathbf{v}$, T, and f_{iK}. To simplify many derivative calculations, we rewrite this expression using $\partial_t \ln f = 1/f \; \partial_t f$

$$\begin{aligned} &f_{iF}^{(0)} \left[\partial_t \log(f_{iF}^{(0)}) - \mathrm{D}_t \mathbf{v} \cdot \nabla_{\mathbf{c}} \log(f_{iF}^{(0)}) + (1-h) \left((\mathbf{C} + \mathbf{v}) \cdot \nabla_x \log(f_{iF}^{(0)}) - (\mathbf{C} \otimes \nabla_{\mathbf{C}} \log(f_{iF}^{(0)})) : (\nabla_x \otimes \mathbf{v}) \right) \right] \\ &+ (1-h) \, \mathbf{c} \cdot \nabla_x f_{iK} = (1-h) Q_i^{(1)}[f_{iF}] + (1-h)\Delta_i. \end{aligned} \tag{4A.6}$$

Note that $f_{iF}^{(0)}$ is the Maxwellian, so logarithmic properties can used to avoid complicated chain rules. With the aid of Eqs. (4.37), (4.43), and (4.46), the above equation becomes,

$$\begin{aligned} Q_i^{(1)}[f_{iF}] = f_{iF}^{(0)} \Bigg[&\frac{m_i}{T} (\mathbf{C} \otimes \mathbf{C} - \frac{1}{3}\mathbf{C}^2 \mathrm{I}) : (\nabla_x \otimes \mathbf{v}) + \mathbf{C} \cdot \left(\left(\frac{m_i}{2T} \mathbf{C}^2 - \frac{5}{2} \right) \nabla_x \log(T) \right) + \frac{n}{n_i} \mathbf{C} \cdot \mathbf{d}_i \\ &- \frac{m_i}{\rho T} \mathbf{C} \cdot \mathbf{J}_K + \left(1 - \frac{m_i \mathbf{C}^2}{3T} \right) \left(\frac{1}{nT} H_K - \frac{3}{2n} \nabla_x \cdot \tilde{\mathbf{K}}_1 \right) - \frac{1}{n_i} \nabla \cdot \tilde{\mathbf{K}}_{1,i} \Bigg] + \mathbf{c} \cdot \nabla_x f_{iK} - \Delta_i, \end{aligned} \tag{4A.7}$$

where

$$\mathbf{d}_i = \frac{n_i}{n}\nabla_x \log(p_i) - \frac{\rho_i}{\rho}\nabla_x \log(p) \tag{4A.8}$$

is the diffusion driving force and $p_i = n_i T$. The first line contains the typical Chapman-Enskog terms from [21], and the second line contains the new terms arising from the presence of f_{iK}.

4A.2 Computation of $f^{(1)}$

Although the derivation of the correction to the BGK collision operator in the first part of this section has been presented in earlier works [21], we repeat it here for completeness. We want to find $Q_i^{(1)} = \sum_j Q_{ij}^{(1)}$. For this we first write the bulk velocity as,

$$n_i \mathbf{v}_i = \langle \mathbf{c} f_i \rangle = \langle \mathbf{c} f_i^{(0)} \rangle + \epsilon \langle \mathbf{c} f_i^{(1)} \rangle = \langle (\mathbf{C} + \mathbf{v}) f_i^{(0)} \rangle + \epsilon \langle \mathbf{c} f_i^{(1)} \rangle = n_i \mathbf{v} + \epsilon \langle \mathbf{c} f_i^{(1)} \rangle = n_i \mathbf{v} + \epsilon\, n_i \mathbf{v}_i^{(1)}. \tag{4A.9}$$

and note that $\mathbf{v}_i = \mathbf{v} + \epsilon\, \mathbf{v}_i^{(1)}$. Similarly, for the temperature:

$$\begin{aligned}
\frac{3}{2} n_i T_i &= \left\langle \frac{m_i}{2} (\mathbf{c} - \mathbf{v}_i)^2 (f_i^{(0)} + \epsilon f_i^{(1)}) \right\rangle = \left\langle \frac{m_i}{2} (\mathbf{C} + \mathbf{v} - \mathbf{v}_i)^2 f_i^{(0)} \right\rangle + \epsilon \left\langle \frac{m_i}{2} (\mathbf{c} - \mathbf{v}_i)^2 f_i^{(1)} \right\rangle \\
&= \left\langle \frac{m_i}{2} \left(C^2 + (\mathbf{v} - \mathbf{v}_i)^2 \right) f_i^{(0)} \right\rangle + \frac{3}{2} \epsilon \left\langle \frac{m_i}{3} (\mathbf{c} - \mathbf{v}_i)^2 f_i^{(1)} \right\rangle \\
&= \frac{3}{2} n_i T + \frac{1}{2} (\mathbf{v} - \mathbf{v}_i)^2 \rho_i + \frac{3}{2} \epsilon n_i T_i^{(1)}
\end{aligned} \tag{4A.10}$$

we use that $\mathbf{v}_i - \mathbf{v} = \epsilon \mathbf{v}_i^{(1)}$ so that $T_i = T + \epsilon T_i^{(1)}$. One may want to include f_{iK} since it is at order ϵ in the buffer region. However, the collision operator solely depends on f_{iF} here. Thus the definitions of $\mathbf{v}_{ij}$ and T_{ij} are defined as in [21]:

$$\mathbf{v}_{ij} = \frac{\rho_i \nu_{ij} \mathbf{v}_i + \rho_j \nu_{ji} \mathbf{v}_j}{\rho_i \nu_{ij} + \rho_j \nu_{ji}} = \mathbf{v} + \epsilon\, \frac{\rho_i \nu_{ij} \mathbf{v}_i^{(1)} + \rho_j \nu_{ji} \mathbf{v}_j^{(1)}}{\rho_i \nu_{ij} + \rho_j \nu_{ji}} = \mathbf{v} + \epsilon\, \mathbf{v}_{ij}^{(1)} \tag{4A.11}$$

$$T_{ij} = \frac{n_i \nu_{ij} T_i + n_j \nu_{ji} T_j}{n_i \nu_{ij} + n_j \nu_{ji}} + \frac{\rho_i \nu_{ij} (\mathbf{v}_i^2 - \mathbf{v}_{ij}^2) + \rho_j \nu_{ji} (\mathbf{v}_j^2 - \mathbf{v}_{ji}^2)}{3(n_i \nu_{ij} + n_j \nu_{ji})} = T + \epsilon\, T_{ij}^{(1)}. \tag{4A.12}$$

Next, we will apply these terms in the expansion of the multi-species Maxwellian:

$$M_{ij} = M_{ij}\big|_{\epsilon=0} + \epsilon \left(\frac{\partial}{\partial \epsilon} M_{ij} \right)_{\epsilon=0} = f_i^{(0)} + \epsilon \left(\frac{\partial}{\partial \epsilon} M_{ij} \right)_{\epsilon=0} \tag{4A.13}$$

with [21]

$$M_{ij} = n_i \left(\frac{m_i}{2\pi T_{ij}}\right)^{3/2} \exp\left(-\frac{m_i \left(\mathbf{c} - \mathbf{v}_{ij}\right)^2}{2T_{ij}}\right)$$
$$= n_i \left(\frac{m_i}{2\pi \left(T + \epsilon T_{ij}^{(1)}\right)}\right)^{3/2} \exp\left(-\frac{m_i \left(\mathbf{c} - \mathbf{v} - \epsilon\, \mathbf{v}_{ij}^{(1)}\right)^2}{2\left(T + \epsilon\, T_{ij}^{(1)}\right)}\right) \tag{4A.14}$$

so that

$$\left(\frac{\partial}{\partial \epsilon} M_{ij}\right)_{\epsilon=0} = f_i^{(0)} \left[\frac{m_i}{T}\mathbf{C}\cdot\mathbf{v}_{ij}^{(1)} + \left(\frac{\frac{1}{2}m_i C^2}{T} - \frac{3}{2}\right)\frac{T_{ij}^{(1)}}{T}\right] = M_{ij}^{(1)} \tag{4A.15}$$

and $M_{ij} = f_i^{(0)} + \epsilon M_{ij}^{(1)}$. Inserting this expression into the multi-species BGK collision operator results in:

$$Q_{ij}^{\mathrm{BGK}} = \nu_{ij}\left(M_{ij} - f_i\right) = \nu_{ij}\left(f_i^{(0)} + \epsilon M_{ij}^{(1)} - f_i^{(0)} - \epsilon f_i^{(1)}\right) = \nu_{ij}\,\epsilon\,\left(M_{ij}^{(1)} - f_i^{(1)}\right). \tag{4A.16}$$

Considering that $Q_{ij}^{\mathrm{BGK}} = \epsilon Q_{ij}^{(1)} + O(\epsilon^2)$ we also can use the previously derived expression for $Q_i^{(1)}$:

$$Q_i^{(1)} = \sum_j Q_{ij}^{(1)} = \sum_j \nu_{ij}\left(M_{ij}^{(1)} - f_i^{(1)}\right) = \sum_j \nu_{ij} M_{ij}^{(1)} - \sum_j \nu_{ij} f_i^{(1)} \tag{4A.17}$$

which gives us an expression for $f_i^{(1)}$:

$$f_i^{(1)} = \frac{1}{\sum_j \nu_{ij}}\left(\sum_j \nu_{ij} M_{ij}^{(1)} - Q_i^{(1)}\right) \tag{4A.18}$$

Inserting expressions for $M_{ij}^{(1)}$ and $Q_i^{(1)}$

$$f_i^{(1)} = \sum_j \frac{\nu_{ij}}{\nu_i} f_{iF}^{(0)} \left[\frac{m_i}{T}\mathbf{C}\cdot\mathbf{v}_{ij}^{(1)} + \left(\frac{\frac{1}{2}m_i C^2}{T} - \frac{3}{2}\right)\frac{T_{ij}^{(1)}}{T}\right]$$
$$- \frac{f_{iF}^{(0)}}{\nu_i}\left[\frac{m_i}{T}\left(\mathbf{C}\otimes\mathbf{C} - \frac{1}{3}C^2\mathbf{I}\right) : (\nabla_x \otimes \mathbf{v}) + \mathbf{C}\cdot\left(\left(\frac{m_i}{2T}C^2 - \frac{5}{2}\right)\nabla_x \log(T)\right) + \frac{n}{n_i}\mathbf{C}\cdot\mathbf{d}_i\right.$$
$$\left. - \frac{m_i}{\rho T}\mathbf{C}\cdot\mathbf{J}_K + \left(1 - \frac{m_i C^2}{3T}\right)\left(\frac{1}{nT}H_K - \frac{3}{2n}\nabla_x\cdot\tilde{\mathbf{K}}_1\right) - \frac{1}{n_i}\nabla_x\cdot\tilde{\mathbf{K}}_{1,i}\right] - \frac{1}{\nu_i}\mathbf{c}\cdot\nabla_x f_{iK} + \frac{1}{\nu_i}\Delta_i. \tag{4A.19}$$

Note that for $h \to 0$, the kinetic terms in the last line go to zero and we recover the standard Navier-Stokes correction for $f_i^{(1)}$ from Eq(4.48).

4A.3 Computation of $\mathbf{v}_{ij}^{(1)}$ and $T_{ij}^{(1)}$

According to Eq. 4A.11, to compute $\mathbf{v}_{ij}^{(1)}$ we need to determine $\mathbf{v}_{i}^{(1)}$. To do this we multiply both sides of the expression for $f_i^{(1)}$ with $m_i\mathbf{C}$ and integrate over $\mathbf{C}$ (*i.e.* compute $\rho_i\mathbf{V}_i = \rho_i\epsilon\mathbf{v}_i^{(1)} = \epsilon\left\langle m_i\mathbf{C}f_i^{(1)}\right\rangle$). Most of the terms are zero because f_{iF} has no odd moments and we are left with:

$$\rho_i\mathbf{v}_i^{(1)} = \frac{\rho_i}{\nu_i}\sum_j \nu_{ij}\mathbf{v}_{ij}^{(1)} - \frac{1}{\nu_i}\mathbf{w}_i + \frac{1}{\nu_i}\left\langle m_i\mathbf{C}\,\Delta_i\right\rangle, \quad \mathbf{w}_i \equiv nT\mathbf{d}_i + \frac{\rho_i}{\rho}\mathbf{J}_K - \mathbf{J}_{iK}. \tag{4A.20}$$

Using the definition of $\mathbf{v}_{ij}^{(1)}$ we obtain,

$$\sum_j \frac{\rho_i\rho_j\nu_{ij}\nu_{ji}}{\rho_i\nu_{ij}+\rho_j\nu_{ji}}(\mathbf{V}_j - \mathbf{V}_i) = \mathbf{w}_i - \left\langle m_i\mathbf{C}\,\Delta_i\right\rangle. \tag{4A.21}$$

As deduced in previous works [21], if the system in eq.(4A.21) is subject to the constraint, $\sum_i \rho_i\mathbf{V}_i = 0$, then the system of equations can be formulated as $A\mathbf{v} = \mathbf{w}$, where:

$$A_{ij} = \begin{cases} -\sum_j \frac{\rho_i\rho_j\nu_{ij}\nu_{ji}}{\rho_i\nu_{ij}+\rho_j\nu_{ji}} - \rho_i\rho_j, & \text{if } i = j \\ \frac{\rho_i\rho_j\nu_{ij}\nu_{ji}}{\rho_i\nu_{ij}+\rho_j\nu_{ji}} - \rho_i\rho_j, & \text{if } i \neq j \end{cases} \tag{4A.22}$$

Next, we focus on $T_{ij}^{(1)}$. According to Eq. 4A.12, to compute $T_{ij}^{(1)}$ we need to determine $T_i^{(1)}$. The mathematical steps here are the same as before (*i.e.* compute a moment and solve a system of equations). We multiply both sides of the expression for $f_i^{(1)}$ with m_iC^2 and integrate over $\mathbf{c}$ (*i.e.* compute $\left\langle m_iC^2f_i^{(1)}\right\rangle$). Most of the terms are zero because f_{iF} has no odd moments and we are left with:

$$n_iT_i^{(1)} = \sum_j \frac{\nu_{ij}}{\nu_i}n_iT_{ij}^{(1)} - \frac{s_i}{\nu_i} + \frac{1}{\nu_i}\left\langle m_iC^2\Delta\right\rangle, \quad s_i \equiv -\frac{2}{3}\left(\frac{n_i}{n}H_K - H_{iK}\right) + T\left(\frac{n_i}{n}\nabla_x\cdot\tilde{\mathbf{K}}_1 - \nabla_x\cdot\tilde{\mathbf{K}}_{1,i}\right) \tag{4A.23}$$

Next, we subtract the left-hand side and reformulate,

$$\sum_j \frac{n_in_j\nu_{ij}\nu_{ji}}{n_i\nu_{ij}+n_j\nu_{ji}}\left(T_j^{(1)} - T_i^{(1)}\right) = s_i - \left\langle m_iC^2\Delta_i\right\rangle. \tag{4A.24}$$

As deduced in previous works [21], if the system in eq.(4A.24) is subject to the constraint, $\sum_i n_iT_i^{(1)} = 0$, then the system of equations can be formulated as $B\mathbf{T}^{(1)} = \mathbf{s}$, where:

$$B_{ij} = \begin{cases} -\sum_j \frac{n_in_j\nu_{ij}\nu_{ji}}{n_i\nu_{ij}+n_j\nu_{ji}} - n_in_j, & \text{if } i = j \\ \frac{n_in_j\nu_{ij}\nu_{ji}}{n_i\nu_{ij}+n_j\nu_{ji}} - n_in_j, & \text{if } i \neq j \end{cases} \tag{4A.25}$$

This system has a unique solution with a symmetric formulation.

APPENDIX 4B

CORRECTIONS TO THE STRESS TENSOR

To find the correction to the stress tensor, we have to calculate $\mathrm{P}_i^{(1)} = \langle m_i \left(\mathbf{C}\otimes\mathbf{C}\right)\ f_i^{(1)}\rangle$. Only terms in $f_i^{(1)}$ that contain an even power of $\mathbf{C}$ should be non-zero. The first term is [21]:

$$-\frac{1}{\nu_i}\left\langle m_i\left[\frac{m_i}{T}\left(\mathbf{C}\otimes\mathbf{C}-\frac{1}{3}C^2\mathrm{I}\right):\left(\nabla_x\otimes\mathbf{v}\right)\right]\left(\mathbf{C}\otimes\mathbf{C}\right)f_i^{(0)}\right\rangle = -\frac{n_iT}{\nu_i}\left(\left(\nabla_x\otimes\mathbf{v}\right)+\left(\nabla_x\otimes\mathbf{v}\right)^T-\frac{2}{3}(\nabla_x\cdot\mathbf{v})\mathrm{I}\right) \tag{4B.1}$$

The second relevant term is:

$$\sum_j\frac{\nu_{ij}}{\nu_i}T_{ij}^{(1)}\left\langle m_i\left(\mathbf{C}\otimes\mathbf{C}\right)\left(\frac{m_i}{2T^2}C^2-\frac{3}{2}\frac{1}{T}\right)f_i^{(0)}\right\rangle = \sum_j\frac{\nu_{ij}}{\nu_i}T_{ij}^{(1)}n_i\mathrm{I} \tag{4B.2}$$

followed by:

$$-\frac{1}{\nu_i}\left(\frac{1}{nT}H-\frac{3}{2n}\nabla_x\cdot\tilde{\mathbf{K}}_1\right)\left\langle m_i\left(\mathbf{C}\otimes\mathbf{C}\right)\left(1-\frac{m_iC^2}{3T}\right)f_i^{(0)}\right\rangle+\frac{1}{\nu_i}\left(\frac{1}{n_i}\nabla_x\cdot\tilde{\mathbf{K}}_{1,i}\right)\langle m_i\left(\mathbf{C}\otimes\mathbf{C}\right)\ f_i^{(0)}\rangle \tag{4B.3}$$

$$=\frac{1}{\nu_i}\left(\frac{2n_i}{3n}H_K-T\frac{n_i}{n}\nabla_x\cdot\tilde{\mathbf{K}}_1\right)\mathrm{I}+\frac{T}{\nu_i}\nabla_x\cdot\tilde{\mathbf{K}}_{1,i}\mathrm{I} \tag{4B.4}$$

$$=\frac{1}{\nu_i}\left(\frac{2}{3}\left(\frac{n_i}{n}H_K-H_{iK}\right)-T\left(\frac{n_i}{n}\nabla_x\cdot\tilde{\mathbf{K}}_1-\nabla_x\cdot\tilde{\mathbf{K}}_{1,i}\right)\right)\mathrm{I}+\frac{2}{3\nu_i}H_{iK}\mathrm{I}+\frac{1}{\nu_i} \tag{4B.5}$$

$$=\frac{1}{\nu_i}s_i\mathrm{I}+\frac{2}{3\nu_i}H_{iK}\mathrm{I} \tag{4B.6}$$

The final term can be used to eliminate the H_{iK} from the previous term:

$$-\frac{1}{\nu_i}\left\langle m_i\left(\mathbf{C}\otimes\mathbf{C}\right)\mathbf{c}\cdot\nabla_x f_{iK}\right\rangle = -\frac{1}{\nu_i}\left\langle m_i\left(\mathbf{C}\otimes\mathbf{C}-\frac{1}{3}C^2\mathrm{I}\right)\mathbf{c}\cdot\nabla_x f_{iK}\right\rangle-\frac{2}{3\nu_i}H_{iK}\mathrm{I} \tag{4B.7}$$

Combining these expressions with the Δ term which we didn't alter, the correction to the stress tensor is:

$$\begin{aligned}\mathrm{P}_i^{(1)} =& -\frac{n_iT}{\nu_i}\left(\left(\nabla_x\otimes\mathbf{v}\right)+\left(\nabla_x\otimes\mathbf{v}\right)^{\mathrm{T}}-\frac{2}{3}(\nabla_x\cdot\mathbf{v})\ \mathrm{I}\right)+\sum_j\frac{\nu_{ij}}{\nu_i}T_{ij}^{(1)}n_i\mathrm{I}\\ &+\frac{1}{\nu_i}s_i\mathrm{I}-\left\langle m_i\left(\mathbf{C}\otimes\mathbf{C}-\frac{1}{3}C^2\mathrm{I}\right)\mathbf{c}\cdot\nabla_x f_{iK}\right\rangle+\frac{1}{\nu_i}\left\langle m_i\left(\mathbf{C}\otimes\mathbf{C}\right)\Delta_i\right\rangle\end{aligned} \tag{4B.8}$$

APPENDIX 4C

CORRECTIONS TO THE HEAT FLUX

To find corrections to the heat flux, we must calculate $\mathrm{q}_i^{(1)} = \langle \frac{m_i}{2} C^2 \mathbf{C}\, f_i^{(1)} \rangle$. Many terms cancel due to symmetry; only terms in $f_i^{(1)}$ with odd powers of $\mathbf{C}$ will have non-zero contributions. The first non-zero term in the calculation is

$$-\frac{1}{2\nu_i}\left\langle m_i \left(C^2\mathbf{C}\right)\left(\mathbf{C}\cdot\left[\left(\frac{m_i}{2T}C^2-\frac{5}{2}\right)\nabla_x \log(T)\right]\right) f_i^{(0)}\right\rangle \tag{4C.1}$$

For a vector $\mathbf{A}$, not dependent on $\mathbf{C}$, we know that [22],

$$\langle C^{2n}\mathbf{C}\ (\mathbf{C}\cdot\mathbf{A})\ f_i^{(0)}\rangle = \frac{1}{3}\mathbf{A}\,\langle C^{2n+2} f_i^{(0)}\rangle\,. \tag{4C.2}$$

Thus, Eq(4C.1) simplifies to

$$-\frac{1}{2\nu_i}\left[\frac{35n_iT^2}{2m_i}-\frac{25n_iT^2}{2m_i}\right]\nabla_x\log(T) = -\frac{1}{\nu_i}\frac{5n_iT}{2m_i}\nabla_x T. \tag{4C.3}$$

Using the same identity, the remaining non-zero heat flux terms are given by

$$-\frac{1}{\nu_i}\frac{n}{n_i}\left\langle \frac{m_i}{2}C^2\mathbf{C}(\mathbf{C}\cdot\mathbf{d}_i)\ f_i^{(0)}\right\rangle = -\frac{1}{\nu_i}\frac{5nT^2}{2m_i}\mathbf{d}_i, \tag{4C.4}$$

$$\frac{1}{\nu_i}\frac{m_i}{\rho T}\left\langle \frac{m_i}{2}C^2\mathbf{C}(\mathbf{C}\cdot\mathbf{J}_K)\ f_i^{(0)}\right\rangle = \frac{1}{\nu_i}\frac{5n_iT}{2\rho}\,\mathbf{J}_K, \tag{4C.5}$$

and

$$\left\langle \frac{m_i}{2}C^2\mathbf{C}\left(\sum_j \frac{\nu_{ij}}{\nu_i} f_i^{(0)}\left[\frac{m_i}{T}\mathbf{C}\cdot\mathbf{v}_{ij}\right]\right)\right\rangle = \sum_j \frac{\nu_{ij}}{\nu_i}\frac{m_i}{T}\left\langle \frac{m_i}{2}C^2\mathbf{C}\left(\mathbf{C}\cdot\mathbf{v}_{ij}\right) f_i^{(0)}\right\rangle = \sum_j \frac{\nu_{ij}}{\nu_i}\frac{5}{2}n_i\,T\,\mathbf{v}_{ij}. \tag{4C.6}$$

Combining these calculations, the heat flux correction is

$$\begin{aligned}
\epsilon\mathbf{q}_i &= -\epsilon\frac{5}{2}\frac{n_iT}{m_i\nu_i}\nabla_x T + \epsilon\sum_j\frac{\nu_{ij}}{\nu_i}\frac{5}{2}n_iT\mathbf{v}_{ij} - \frac{\epsilon}{\nu_i}\frac{5}{2}\frac{nT^2}{m_i}\mathbf{d}_i + \frac{\epsilon}{\nu_i}\frac{5}{2}\frac{n_iT}{\rho}\mathbf{J}_K \\
&\quad - \frac{\epsilon}{\nu_i}\left\langle\frac{m_i}{2}C^2\mathbf{C}(\mathbf{c}\cdot\nabla_x f_{iK})\right\rangle + \frac{1}{\nu_i}\langle\frac{m_i}{2}C^2\mathbf{C}\,\Delta_i\rangle \\
&= -\frac{5}{2}\epsilon\,\frac{n_iT}{m_i\nu_i}\nabla_x T + \epsilon\frac{5}{2}\frac{T}{m_i}\left(\frac{\rho_i}{\nu_i}\sum_j\nu_{ij}\mathbf{v}_{ij} - \frac{nT}{\nu_i}\mathbf{d}_i + \frac{1}{\nu_i}\frac{\rho_i}{\rho}\mathbf{J}_K - \frac{1}{\nu_i}\mathbf{J}_{iK} + \frac{1}{\nu_i}\mathbf{J}_{iK}\right) \\
&\quad - \frac{\epsilon}{\nu_i}\left\langle\frac{m_i}{2}C^2\mathbf{C}(\mathbf{c}\cdot\nabla_x f_{iK})\right\rangle + \frac{1}{\nu_i}\langle\frac{m_i}{2}C^2\mathbf{C}\,\Delta_i\rangle \\
&= \epsilon\frac{5}{2}\frac{T}{m_i}\left(-\frac{n_i}{\nu_i}\nabla_x T + \rho_i\mathbf{v}_i + \frac{1}{\nu_i}\mathbf{J}_{iK}\right) - \frac{\epsilon}{\nu_i}\left\langle\frac{m_i}{2}C^2\mathbf{C}(\mathbf{c}\cdot\nabla_x f_{iK})\right\rangle + \frac{1}{\nu_i}\langle\frac{m_i}{2}C^2\mathbf{C}\,\Delta_i\rangle
\end{aligned} \tag{4C.7}$$

CHAPTER 5

MACHINE LEARNING MODEL CLOSURES

5.1 Introduction

In near-vacuum-hohlraum inertial confinement fusion (ICF) experiments, the ions' mean free path is too long for the system to be sufficiently described by the hydrodynamic equations [1]. To simulate such kinetic systems, extended moment hydrodynamic models can be employed [2]. By including moments of the distribution function beyond the moments which define a Gaussian, *i.e.*, density, velocity, temperature, these equations include more kinetic phenomena than typical fluid dynamics equations.

An infinite number of moments are needed to describe the non-equilibrium distribution evolved by a kinetic equation, but only a finite number can be simulated. Additionally, the N-th moment depends on an unknown $N+1$-th moment. Thus, truncating the hierarchy of moment equations requires an assumption which rewrites the $N+1$-th moment in terms of the previous N moments, often referred to as closure information. Often it is assumed that the system is near local equilibrium and this limits the model's predictive capacity. As such closures are a critical area of research for modeling systems with kinetic phenomena.

Machine learning (ML) techniques are emerging approaches to the moment closure problem, where a truncated system of moment equations is closed with a neural network [3]. This approach is often used because neural networks can go beyond local equilibrium assumptions [4]. Neural closures, a special type of Neural ODE (NODE) [5], are a leading approach to data-driven closures [6]. Many investigators have found that enforcing some structure in the NODE results in lower errors in long-term evolution, improving the predictive capacity [7, 8, 9]. For instance, Huang et al. have enforced hyperbolicity in the neural closure of extended moment methods [10, 11]. These constraints ensure that the system's evolution adheres to an invariant manifold within the solution space. However, Celledoni et al. indicate in their review of structure-preserving deep learning that the " generalisation of most [NODEs] to the manifold setting is still missing" [12].

In extended moment models, the closures include dissipation that returns the system to equilib-

rium. This equilibration process has been formulated as the convergence to the invariant manifold in the space of distributions [13]. Thus invariant manifold detection is a key criteria to assess the quality of a closure. According to the Hartman-Grobman theorem, a dynamical system's Jacobian near an equilibrium characterizes an invariant manifold. Alternatively, dynamic mode decomposition (DMD), rooted in the Koopman operator framework, is a computational approach that can be characterize the invariant manifold of a system [14]. Furthermore, Lan and Mezic's results indicate that DMD's linear operator may extend the Hartman–Grobman theorem, enlarging the domain of linearity from near the equilibrium to the next equilibrium point [15]. A DMD-based reconstruction error has been used to detect regime transition [16], but the authors do not make the explicit connection to the invariant manifold.

In this work, we apply DMD and dimension reduction techniques, developed by Roweis and Saul [17], to assess whether a closure guides a system towards an invariant manifold. We focus on observing both the convergence to the slow manifold and the slow manifold. This is an alternative to observing the constants of motion which characterize the invariant manifold. Our data-driven investigation is done in the context of extended moment fluid dynamics equations implemented with either Grad's closure [18] or a neural closure. We find that our neural closure can equilibrate towards a slow manifold.

The structure of this chapter is as follows. In Section 5.2 we introduce Grad's moment equations. In section 5.3 we introduce Neural ODEs and show how the technique is used to resolve the closure problem. Our major results are contained in section 5.4, we introduce the methods for observing system equilibration and apply these methods to investigate the slow manifold in Grad's system with and without a neural closure. We provide a summary and outlook in Section 5.5. Lastly, a numerical comparison between neural ODEs and neural closures is provided in the appendix.

5.2 Grad's Hydrodynamic Equations

Grad's extended moment hydrodynamic equations are derived from the Boltzmann equation by expanding the distribution function f in a Hermite basis [18]. The near-equilibrium, 1-dimensional

version of Grad's equations can be expressed [13]

$$\partial_t f + A(f) = \frac{1}{\epsilon} Q(f). \tag{5.1a}$$

The vector of moments f is defined as $f(x,t) \equiv [\rho(x,t), u(x,t), T(x,t), \sigma(x,t), q(x,t)]^T$, where $\rho = \delta\rho/\rho_0$ is the relative density, $u = \delta u/u_0$ is the relative velocity, and $T = \delta T/T_0$ is the relative temperature. Further, σ is the dimensionless pressure tensor, q is the dimensionless heat flux, t is the dimensionless time, and x is the dimensionless distance. The advection term $A(f)$ is defined

$$A(f) \equiv \begin{bmatrix} \partial_x u \\ \partial_x (p + u + \sigma) \\ \frac{2}{3}\partial_x (u + q) \\ \partial_x \left(2u + \frac{4}{5} q\right) \\ \partial_x \left(\frac{5}{2} T + \sigma\right) \end{bmatrix}, \tag{5.1b}$$

and the dissipative or "collisional" term Q is defined

$$Q(f) \equiv \begin{bmatrix} 0 \\ 0 \\ 0 \\ -\sigma \\ -2q/3 \end{bmatrix}. \tag{5.1c}$$

In this dissertation, we chose $k = 1$ and $\epsilon = \pi/25$, a decision that, according to dispersion relations, decouples the hydrodynamic modes from the kinetic modes [13]. Eq(5.1) is one of many approaches to the fluid dynamics moment closure problem, closing the typical hydrodynamics equations of ρ, $\mathbf{u}$, and T by expressing the dynamics of the pressure tensor σ and the heat flux q in terms of f. The conventions of Eq(5.1) are intentionally chosen to evoke connections between Grad's extended moment equations and kinetic equations.

Grad's equations are known to enforce equilibration to a slow manifold [13]. By the Hartmann-Grobmann theorem, we can expand about equilibrium to produce analytic estimates of the invariant

manifold. Let ϵ be small, expanding Eq(5.1) to linear order about

$$f_{\epsilon=0} \equiv Mf = [\rho, u, T, 0, 0], \tag{5.2}$$

where M is the matrix which projects the equilibrium moments, yields

$$\partial_t f_\epsilon = F(f_0) + \nabla_f F(f)\Big|_{f=f_0} \delta f. \tag{5.3}$$

In this expression, $\delta f = Q^{-1}(I - \partial_{f_0} f \cdot M)A(f_0)$ and $\nabla_f F(f)\Big|_{f=f_0}$ is the Jacobian. Evaluating the RHS produces the Navier-Stokes equations,

$$\partial_t \begin{bmatrix} \rho \\ u \\ T \\ \sigma \\ q \end{bmatrix} = - \begin{bmatrix} \partial_x u \\ \partial_x (p + u) - \epsilon \frac{4}{3} \partial_x^2 u \\ \frac{2}{3} \partial_x u - \epsilon \frac{5}{2} \partial_x T \\ 0 \\ 0 \end{bmatrix} \tag{5.4}$$

This equilibrium expansion is structured to emphasize the connection between the dynamic system's Jacobian and the Chapman-Enskog expansion used to produce the Navier Stokes equations. From these derivations, we see that, for rapidly dissipating systems $\epsilon \ll 1$, Grad's moment equations are well described by its invariant manifold.

In this work, we consider the Fourier transform $\rho(r, t) = \sum_{-\infty}^{+\infty} \rho_k(t) e^{i\mathbf{k}\cdot\mathbf{r}}$ of the these PDEs. For these near-equilibrium equations, the Fourier transform reduces Grad's equations to a system of ODEs. The eigenvalues of this ODE update matrix define the dispersion relations. A table organizing the equations and their Fourier transforms is presented in Table 5.1

5.3 Neural Closures

Neural ODEs (NODE) use neural networks (NN) to solve differential equations [5]. NODEs emerged as the continuous time version of ResNets [19]. NODEs were originally formulated to predict the difference between an input x_0 and the desired output x_1 as $x_1 = x_0 + \delta t NN(x_0)$, where $NN(x_0)$ is the output of the neural network. The structure resembles an Euler update, where the neural network is learning to predict the derivative. NODEs are particularly suited to inform

$$\partial_t \begin{bmatrix} \rho \\ u \\ T \\ \sigma \\ q \end{bmatrix} = - \begin{bmatrix} \partial_x u \\ \partial_x \left(p + u + \sigma\right) \\ \frac{2}{3}\partial_x \left(u + q\right) \\ \partial_x \left(2u + \frac{4}{5}q\right) \\ \partial_x \left(\frac{5}{2}T + \sigma\right) \end{bmatrix} - \frac{1}{\epsilon} \begin{bmatrix} 0 \\ 0 \\ 0 \\ \sigma \\ 2q/3 \end{bmatrix} \quad \overset{\text{Fourier}}{\longrightarrow} \quad \partial_t \begin{bmatrix} \rho_k \\ u_k \\ T_k \\ \sigma_k \\ q_k \end{bmatrix} = - \begin{bmatrix} -iku_k \\ -ik\left(p_k + u_k + \sigma_k\right) \\ -ik\frac{2}{3}\left(u_k + q_k\right) \\ -ik\left(2u_k + \frac{4}{5}q_k\right) - \sigma_k/\epsilon \\ -ik\left(\frac{5}{2}T_k + \sigma_k\right) - 2q/3\epsilon \end{bmatrix}$$

$$\downarrow \quad \sigma \approx -\epsilon\tfrac{4}{3}\partial_x u, \;\; q \approx -\epsilon\tfrac{15}{4}\partial_x T \qquad\qquad \downarrow \quad \sigma \approx -ik\epsilon\tfrac{4}{3}u, \;\; q \approx -ik\epsilon\tfrac{15}{4}T$$

$$\partial_t \begin{bmatrix} \rho \\ u \\ T_k \end{bmatrix} = - \begin{bmatrix} \partial_x u \\ \partial_x \left(p + u\right) - \epsilon\frac{4}{3}\partial_x^2 u \\ \frac{2}{3}\partial_x u - \epsilon\frac{5}{2}\partial_x T \end{bmatrix} \quad \overset{\text{Fourier}}{\longrightarrow} \quad \partial_t \begin{bmatrix} \rho_k \\ u_k \\ T_k \end{bmatrix} = - \begin{bmatrix} -iku_k \\ -ik\left(p_k + u_k\right) - \epsilon k^2\frac{4}{3}u \\ -ik\frac{2}{3}u_k - \epsilon k^2\frac{5}{2}T \end{bmatrix}$$

Table 5.1 A grid visualizing the relation between Grad's equations (upper) and Navier-Stokes' equations (lower) in both spatial (left) and Fourier space (right).

closures since closure information is often expressed as an ODE. A neural closure is a type of NODE, in which the neural net estimates a subset of the derivatives needed to update the system's current state. Such approaches often lead to better stability [6].

In the context of Grad's equations, we use our neural closure to estimate $\dot{\sigma}_k$ and $\dot{q}_k$ while $\dot{n}_k$, $\dot{u}_k, \dot{T}_k$ are determined using Grad's equations Eq(5.1). Therefore, our derivative estimator is

$$\dot{f}^{NN}(t) = \begin{bmatrix} \dot{\rho}_k(t) \\ \dot{u}_k(t) \\ \dot{T}_k(t) \\ \dot{\sigma}_k(t) \\ \dot{q}_k(t) \end{bmatrix} = - \begin{bmatrix} iku_k(t) \\ ik\left(p_k(t) + u_k(t) + \sigma_k(t)\right) \\ ik\frac{2}{3}\left(u_k(t) + q_k(t)\right) \\ NN(\text{inputs}) \\ NN(\text{inputs}) \end{bmatrix}. \tag{5.5}$$

In this derivative estimate, mass, momentum, and energy are conserved and the neural network is relegated to where traditional methods may be insufficient. We compare the neural closure to its NODE counterpart in Appendix 5A and demonstrate the neural closure has lower error and better stability.

We use a neural network comprised of a single layer of complex valued 500 Rectified Linear Units (ReLU), this is known as a complex valued neural network (CVNN) [20]. The CVNN predicts

two outputs $\dot{\sigma}_k(t)$ and $\dot{q}_k(t)$ but takes as input the current state $f_k(t) \equiv [\rho_k(t), u_k(t), T_k(t), \sigma_k(t), q_k(t)]^T$, the 5 preceding positions, and the 5 preceding derivatives. The training/testing data is gathered from 15 trajectories of Grad's moment equations evolved $t \in [0, 4]$ with $\delta t = 0.01$. Each trajectory is initialized with coordinates that are randomly sampled from inside a complex 5-dimensional unit ball, *i.e.*, 10 real numbers. For both training and testing data, $\dot{f}_k$ is estimated from the trajectories (with no added noise) using fourth order symmetric finite difference. The sequential inputs and outputs are presented in Figure 5.2.

Table 5.2 Visualization of the complex valued neural network's sequential input data (x) and output data (Y).

time	$t-5\delta t$	$t-4\delta t$	$t-3\delta t$	$t-2\delta t$	$t-\delta t$	t
f	×	×	×	×	×	×
$\partial_t f$	×	×	×	×	×	Y

This neural closure is a derivative approximation, which can be used inside the multi-step update scheme [21]; this approach is known as a multi-step neural closure (MsNC). Multi-step updates recycle previous derivative estimates to improve accuracy. The second order Adams-Bashforth (AB2) multi-step scheme is

$$f(t+\delta t) = f(t) + \delta t \left(\frac{3}{2} \dot{f}^{NN}(t) - \frac{1}{2} \dot{f}^{NN}(t-\delta t) \right). \tag{5.6}$$

We expect increasing the order will decrease the update error.However, we also expect that increasing the multi-step order has diminishing returns as the update error becomes on par with the CVNN prediction error. Numerical tests are conducted in Appendix 5A and these expectations are verified. Sample trajectories, using either Grad's closure Eq(5.1) updated with RK7 or the neural closure Eq(5.5) updated with AB2, are presented in Figure 5.1 Left. For 20 randomly sampled initial conditions, the mean squared error incurred at each time step is plotted in Figure 5.1 Right. The plots demonstrate that error does not grow exponentially at long times.

5.4 Invariant Manifolds

Previous data-driven investigations used manifold learning to observe dimension reduction during the equilibration process. Ellison et al. detected the onset of hydrodynamic evolution in

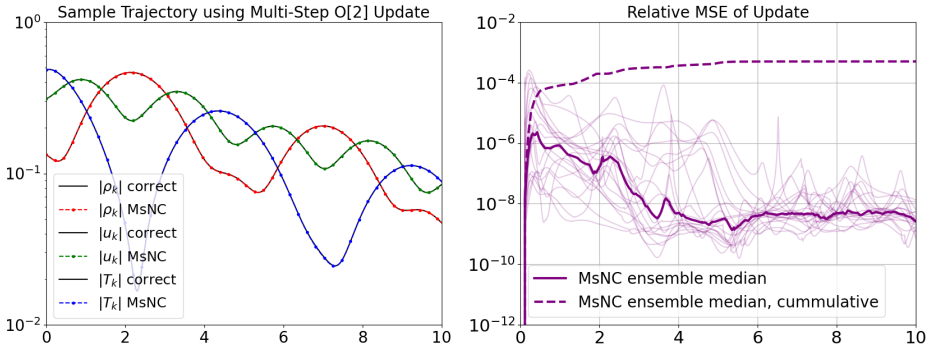

Figure 5.1 Left: neural closure Eq(5.5) evolved with second order multi-step neural closure, labeled as MsNC, plotted alongside Grad's closure Eq(5.1) evolved with seventh order Runge-Kutta, labeled as "correct". The difference between the trajectories is too small to see. Right: The mean square error incurred at each update for 20 trajectories, plotted alongside the smoothed median error, and cumulative smoothed median error. The plot demonstrates that the neural closure does not have exponentially increasing error.

kinetic equations by assessing the reducibility of an ensemble of kinetic evolutions (*i.e.*, ability to reduce the ensemble's dimensionality while preserving its structure) [22]. In this section, we extend this work, complementing it with dynamic mode decomposition to characterize the invariant manifold. We apply both tools to Grad's extended moment hydrodynamics equations with and without a neural closure.

To investigate reducibility, we create two ensembles of trajectories ($N = 10,000$) evolved according to Eq(5.1) with RK7 and Eq(5.5) with AB2. Each trajectory in an ensemble is initialized with coordinates randomly sampled from a complex 5-dimensional unit ball, (*i.e.*, 10 real dimensions) and evolved to $T_{\max} = 1$. At early times the ensemble of points is irreducible, but at late times the ensemble can be reduced from 10 dimensions to 6 dimensions. The reducibility of the data was assessed using Saul and Rowes' inverse reconstruction error E with a principal component analysis (PCA) dimension reduction technique [17]

$$E(t,n) = E_2(t,n)/E_1(t), \tag{5.7a}$$

$$E_1(t) = \|X(t) - W_{BC}(t)X(t)\|_2, \tag{5.7b}$$

$$E_2(t,n) = \|X(t) - W_{RBC}(n,t)X(t)\|_2. \tag{5.7c}$$

Here $X(t)$ is a matrix containing the coordinates of all N trajectories at time t, $W_{BC}(t)$ is the barycen-

ter weight matrix computed from $X(t)$. $W_{RBC}(n,t)$ is the barycenter weight matrix computed from the data after it has been reduced onto n principal vectors [23, 24]. We plot the reconstruction error $E(t,n)$ in Figure 5.2.

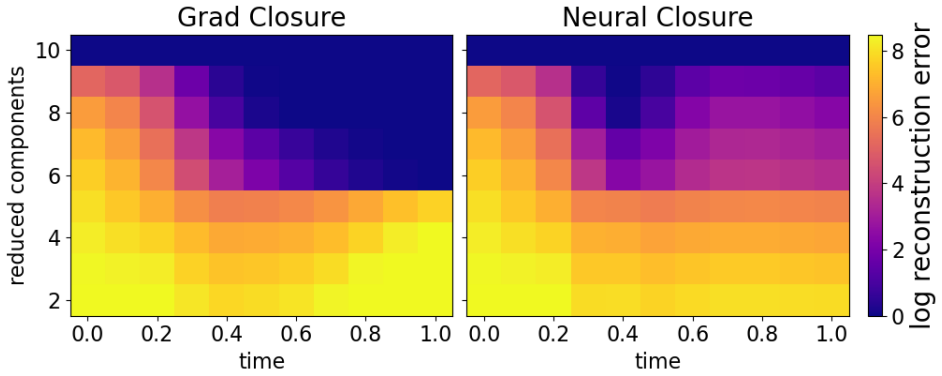

Figure 5.2 Plot of the reducibility of an ensemble of trajectories, as assessed by the inverse reconstruction error [23]. The ensemble is more reducible at later times. The ensemble is reduced using PCA into a various number of dimensions (varied along the y-axis) the evolution time is plotted along the x-axis. The yellow and orange regions indicate that reducing and un-reducing the data destroys the ensemble's local structure and the purple and blue regions indicate that local structure is preserved. Both Grad's closure and the neural closure's evolve to a reduced subspace, though the neural closure is not as reducible as Grad's closure at late time.

To characterize the invariant manifold, we again create two ensembles, initialized the same as in the reducibility investigation. However, each ensemble is composed of 20 simulations evolved to $T_{\max} = 10$, which is 10× longer than the reducibility trajectories. The invariant manifold can be characterized using dynamic mode decomposition (DMD) estimates of the Koopman operator K [14]. The Koopman operator is estimated from a single trajectory, not on the entire ensemble of points. Originally proposed by Schmid, the estimator is defined [25],

$$\min_K \left\| KY - Y' \right\|_F. \tag{5.8}$$

Y and Y' are constructed from the data in a sliding window (*i.e.*, a sub-sequence of a trajectory). Y is a matrix comprised of the initial values and Y' is a matrix comprised of the updated values. The sliding window, Y, and Y' are all visualized in Figure 5.3. The solution to this minimization problem can be computed explicitly as

$$K = Y'Y^{+} = \Xi\Lambda\Xi^{T}. \tag{5.9}$$

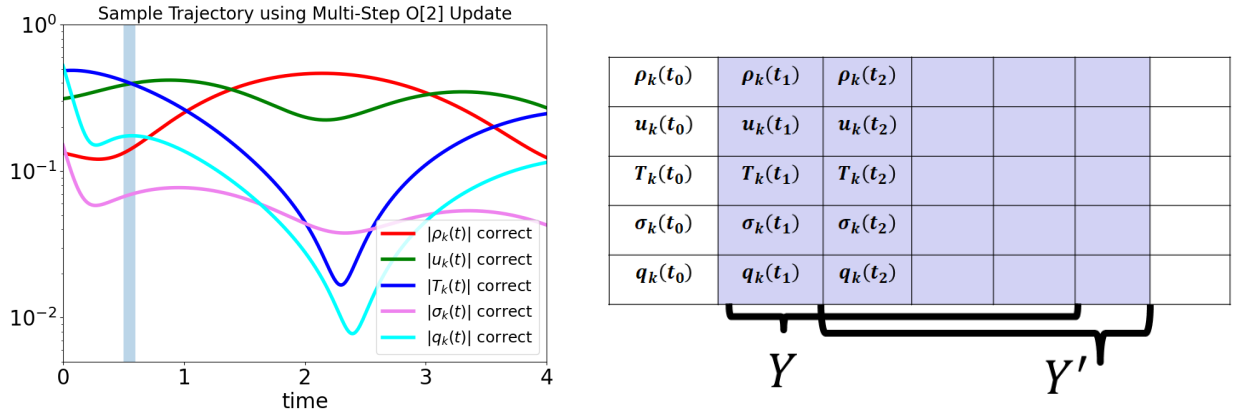

Figure 5.3 Visualization of DMD on a sliding window. DMD is conducted on only the subsequence of data contained in the blue band. Left: View of the sliding window from the global time series level. Right: View of sliding window from the localized data level. The blue window contains 5 time steps, the first 4 comprise Y and the last 4 comprise Y'.

The eigenvalues of K's are represented by $\Lambda = \text{diag}(\lambda_1, \ldots, \lambda_n)$ and the eigenvectors are represented $\Xi = [\xi_1, \ldots, \xi_n]$. From each window of a trajectory we gather eigenvalues and vectors, yielding a time series of eigensystems $\Lambda(t)$ and $\Xi(t)$. For both Grad's closure and the neural closure. the two smallest eigenvalues decrease orders of magnitude by $t = 1$. This indicates dissipation on a similar time scale as seen in the dimension reduction plots. A plot of the eigenvalue time series can be seen in Figure 5.4. Additionally, only one of the neural closure's eigenvalues decays to numerical zero indicating the neural closure carries an additional basis vector in its invariant manifold, demonstrating that the neural closure has an inferior convergence to the invariant manifold. This parallels the neural closure's inferior reducibility. Now consider the eigenvectors which characterize the invariant manifold. To assess whether the sub-sequence of data is discovering the same invariant manifold at each step, we observe the similarity S between the DMD eigenvectors at time t_i and t_j.

$$S_{ij} = \frac{1}{N} \sum_{\text{trajectories}} \langle \xi_k(t_i) | \xi_k(t_j) \rangle \tag{5.10}$$

where N is the number of trajectories. since the system is transient (non-stationary), we do not observe the autocorrelation. Rather, we are looking for the emergence of stationarity, hence our choice of S Eq(5.10). We observe that after $t = 1$, DMD rediscovers the same eigenvector; A plot of the eigenvector similarity across the time series (averaged across 20 random initial conditions) can be seen in Figure 5.5.

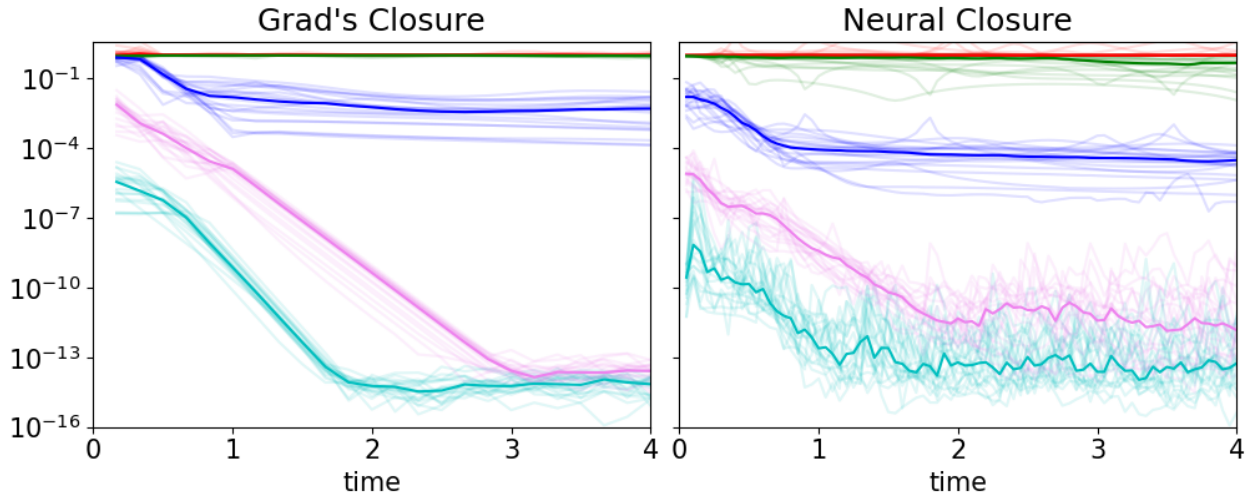

Figure 5.4 Time series of DMD eigenvalues. Left: Sliding Window DMD conducted on full Grad's equations Eq(5.1). Right: Sliding Window DMD conducted on Grad's equations. For both Grad's closure and the neural closure, the eigenvalues separate by orders of magnitude by $t = 1$. This indicates both Grad's closure and the neural closure evolve towards a slow manifold. However, the neural closure converges worse than Grad's closure because the smallest eigenvalues do not reduce to numerical zero.

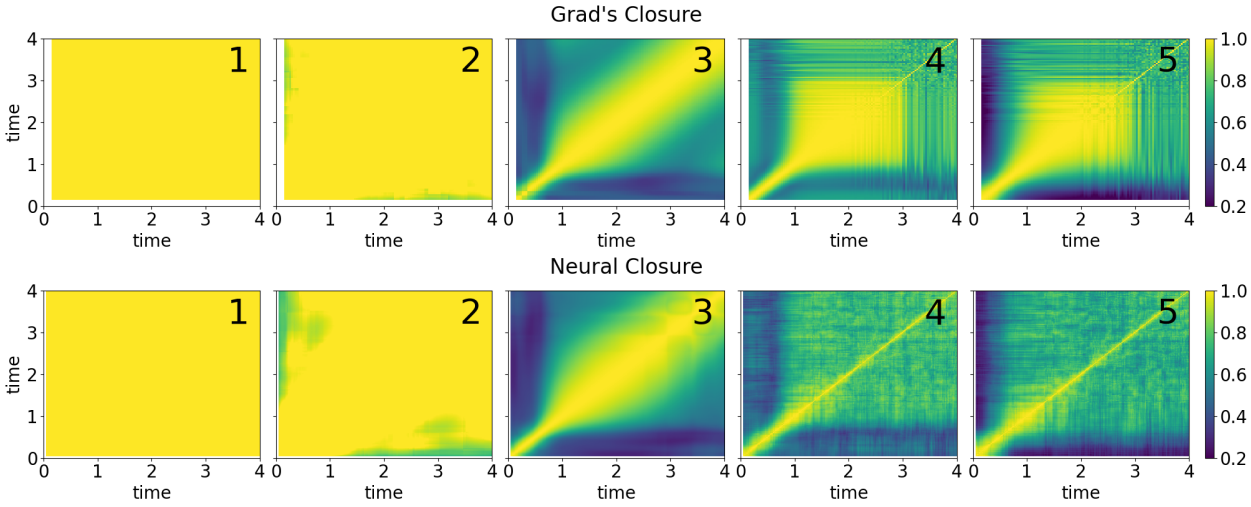

Figure 5.5 Plots of the similarity between a DMD eigenvector at time t_i and at time t_j averaged across 20 random initial conditions (similarity measured by complex dot product). The eigenvector corresponding to the largest eigenvalue is labeled "1", while the eigenvector corresponding to the second largest eigenvalue is labeled "2". A clear transition occurs in both Grad's closure and the neural closure, where the DMD eigenvectors discovered after $t = 1$ are similar to each other. However, with the eigenvectors associated to the neural closure display weaker similarity than the eigenvectors associated to Grad's closure.

In conclusion, the ability to assess convergence to a characterized invariant manifold allows for quantitative comparisons between dissipative closures. Taken together Figures 5.1, 5.2, 5.4, 5.5 indicate that while neural closure incurs a cumulative relative error of less than a tenth of a percent, its overall convergence to an invariant manifold is inferior to Grad's closure. These figures also confirm a visualization of the equilibration process provided in Figure 5.6.

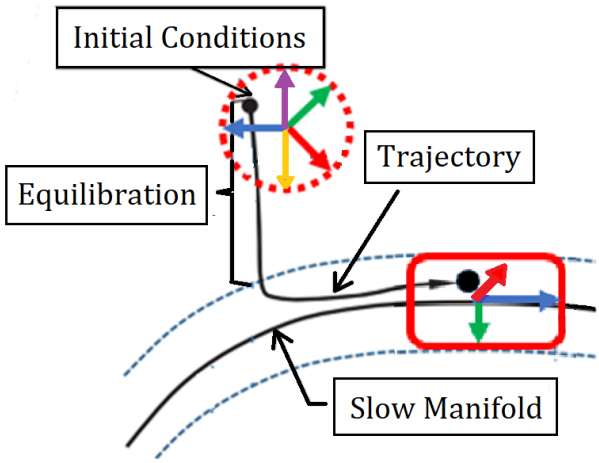

Figure 5.6 Representation of an ensemble of simulations equilibrating according to Grad's eqns towards a slow manifold (image altered from [13]).

5.5 Summary and outlook

In this work, we have presented data-driven approaches to observing a dynamical system's convergence to its slow manifold. These approaches complement previous analytic work done by Gorban and Karlin [13], providing visualizations of the equilibration to the invariant manifold. When the DMD eigenvectors are similar across long time intervals this indicates that the trajectory is evolving on an invariant manifold. When the eigenvectors are dissimilar, we can assess whether the trajectory is exponentially decaying towards or away from an invariant manifold, by the magnitude of the DMD eigenvalues. Together these approaches assess whether the trajectory is transitioning to the invariant manifold characterized by the DMD eigenvectors.

Further, we applied these data-driven techniques to assess the quality of a multi-step neural closure. Our results indicated the neural closures can evolve a system toward an invariant manifold. However, the invariant manifold for the neural closure is a lower quality. This suggests that

the naive neural closure introduces some error which pushes the trajectory off of its invariant manifold, even after the trajectory has converged. In this work, the neural net was not explicitly constrained to converge to the invariant manifold. thus, exploring how to incorporate these data-driven observations as a regularization on the prediction fidelity will be the subject of future work.

BIBLIOGRAPHY

[1] Hans G Rinderknecht, PA Amendt, SC Wilks, and G Collins. Kinetic physics in icf: Present understanding and future directions. *Plasma Physics and Controlled Fusion*, 60(6):064001, 2018.

[2] Nelson M Hoffman, George B Zimmerman, Kim Molvig, Hans G Rinderknecht, Michael J Rosenberg, BJ Albright, Andrei N Simakov, Hong Sio, Alex B Zylstra, Maria Gatu Johnson, et al. Approximate models for the ion-kinetic regime in inertial-confinement-fusion capsule implosions. *Physics of Plasmas*, 22(5), 2015.

[3] Jurriaan Buist, Benjamin Sanderse, Yous van Halder, Barry Koren, and GertJan van Heijst. Machine learning for closure models in multiphase-flow applications. *Crete, Greece*, 2019.

[4] Andrew J Christlieb, Mingchang Ding, Juntao Huang, and Nicholas A Krupansky. Hyperbolic machine learning moment closures for the bgk equations. *arXiv preprint arXiv:2401.04783*, 2024.

[5] Ricky TQ Chen, Yulia Rubanova, Jesse Bettencourt, and David K Duvenaud. Neural ordinary differential equations. *Advances in neural information processing systems*, 31, 2018.

[6] Hugo Melchers, Daan Crommelin, Barry Koren, Vlado Menkovski, and Benjamin Sanderse. Comparison of neural closure models for discretised pdes. *Computers & Mathematics with Applications*, 143:94–107, 2023.

[7] Miles Cranmer, Sam Greydanus, Stephan Hoyer, Peter Battaglia, David Spergel, and Shirley Ho. Lagrangian neural networks. *arXiv preprint arXiv:2003.04630*, 2020.

[8] Pengzhan Jin, Zhen Zhang, Aiqing Zhu, Yifa Tang, and George Em Karniadakis. Sympnets: Intrinsic structure-preserving symplectic networks for identifying hamiltonian systems. *Neural Networks*, 132:166–179, 2020.

[9] Samuel Greydanus, Misko Dzamba, and Jason Yosinski. Hamiltonian neural networks. *Advances in neural information processing systems*, 32, 2019.

[10] Juntao Huang, Yingda Cheng, Andrew J Christlieb, Luke F Roberts, and Wen-An Yong. Machine learning moment closure models for the radiative transfer equation ii: Enforcing global hyperbolicity in gradient-based closures. *Multiscale Modeling & Simulation*, 21(2):489–512, 2023.

[11] Juntao Huang, Yingda Cheng, Andrew J Christlieb, and Luke F Roberts. Machine learning moment closure models for the radiative transfer equation iii: enforcing hyperbolicity and physical characteristic speeds. *Journal of Scientific Computing*, 94(1):7, 2023.

[12] Elena Celledoni, Matthias J Ehrhardt, Christian Etmann, Robert I McLachlan, Brynjulf

Owren, C-B Schonlieb, and Ferdia Sherry. Structure-preserving deep learning. *European journal of applied mathematics*, 32(5):888–936, 2021.

[13] Alexander Gorban and Ilya Karlin. Hilbert's 6th problem: exact and approximate hydrodynamic manifolds for kinetic equations. *Bulletin of the American Mathematical Society*, 51(2):187–246, 2014.

[14] Steven L Brunton, Marko Budisic, Eurika Kaiser, and J Nathan Kutz. Modern koopman theory for dynamical systems. *arXiv preprint arXiv:2102.12086*, 2021.

[15] Yueheng Lan and Igor Mezić. Linearization in the large of nonlinear systems and koopman operator spectrum. *Physica D: Nonlinear Phenomena*, 242(1):42–53, 2013.

[16] Georg A Gottwald and Federica Gugole. Detecting regime transitions in time series using dynamic mode decomposition. *Journal of Statistical Physics*, 179(5-6):1028–1045, 2020.

[17] Sam T Roweis and Lawrence K Saul. Nonlinear dimensionality reduction by locally linear embedding. *science*, 290(5500):2323–2326, 2000.

[18] Harold Grad. On the kinetic theory of rarefied gases. *Communications on pure and applied mathematics*, 2(4):331–407, 1949.

[19] Kaiming He, Xiangyu Zhang, Shaoqing Ren, and Jian Sun. Deep residual learning for image recognition. In *Proceedings of the IEEE conference on computer vision and pattern recognition*, pages 770–778, 2016.

[20] J Agustin Barrachina. Negu93/cvnn: Complex-valued neural networks, November 2022.

[21] Maziar Raissi, Paris Perdikaris, and George Em Karniadakis. Multistep neural networks for data-driven discovery of nonlinear dynamical systems. *arXiv preprint arXiv:1801.01236*, 2018.

[22] Charles Ellison, Frank Graziani, Jeff Haack, Elizabeth Munch, Michael Murillo, and Liam Stanton. Manifold learning to detect the transition from kinetics to hydrodynamics. In *APS Division of Plasma Physics Meeting Abstracts*, volume 2018, pages CM10–006, 2018.

[23] Lawrence K Saul and Sam T Roweis. An introduction to locally linear embedding. *unpublished. Available at: http://www. cs. toronto. edu/˜ roweis/lle/publications. html*, 2000.

[24] Fabian Pedregosa and Jake Vanderplas. locally_linear.py. `https://github.com/scikit-learn/scikit-learn/blob/main/sklearn/manifold/_locally_linear.py`, 2011.

[25] Peter J Schmid. Dynamic mode decomposition of numerical and experimental data. *Journal of fluid mechanics*, 656:5–28, 2010.

APPENDIX 5A

UPDATE ERRORS IN MULTI-STEP NODES AND MULTI-STEP NEURAL CLOSURES

In this appendix, we compare the multi-step neural closure (MsNC) to its unguided multi-step neural ODE (MsNODE) counterpart. For a NODE, every entry on the RHS of Eq(5.5) is estimated by the neural network. Thus, the NODE has 5 outputs, whereas the neural closure has only 2 outputs. To compare these two approaches, we assess the error incurred at each update (mean squared distance from the full Grad's equations updated with RK7) for 20 randomly sampled initial conditions. Comparisons are made for first, second, and third order multi-step update schemes. The first order multi-step update is the common forward Euler update, the second order update is given in Eq(5.6), and the third order update is

$$f(t+\delta t) = f(t) + \delta t \left(\frac{23}{12} \dot{f}^{NN}(t) - \frac{16}{12} \dot{f}^{NN}(t-\delta t) + \frac{5}{12} \dot{f}^{NN}(t-2\delta t) \right). \tag{5A.1}$$

We expect that when conservation of mass, momentum, and energy is enforced the simulation will have lower error and better stability. This is a result that has been demonstrated in countless works on ODEs and constitutes the primary justification for structure preserving methods. We also expect that increasing the order of the multi-step update will decrease the relative difference from the RK7 update because of the order conditions enforced. However, as the update error becomes comparable to the error from the neural network's predictions, increasing the multi-step order yields diminishing returns. Typically, the derivative $\dot{f}$ is calculated at the level of numerical precision. However, this is not the case for a NODE or neural closure because the neural net is trained on derivatives computed via finite difference and the neural net has error in its predictions. These errors, unique to MsNC and MsNODE, are distinct from those incurred by finite step size. Therefore, once the error from finite step size is negligible compared to the error from the neural network's derivative estimate, increasing the multi-step order does not decrease the error. In numerical tests, the MsNC update has lower error and better stability than the MsNODE update. Additionally, both updates improve with increasing order, but diminishing returns are observed. Sample trajectories and error estimates are given in Figure 5A.1.

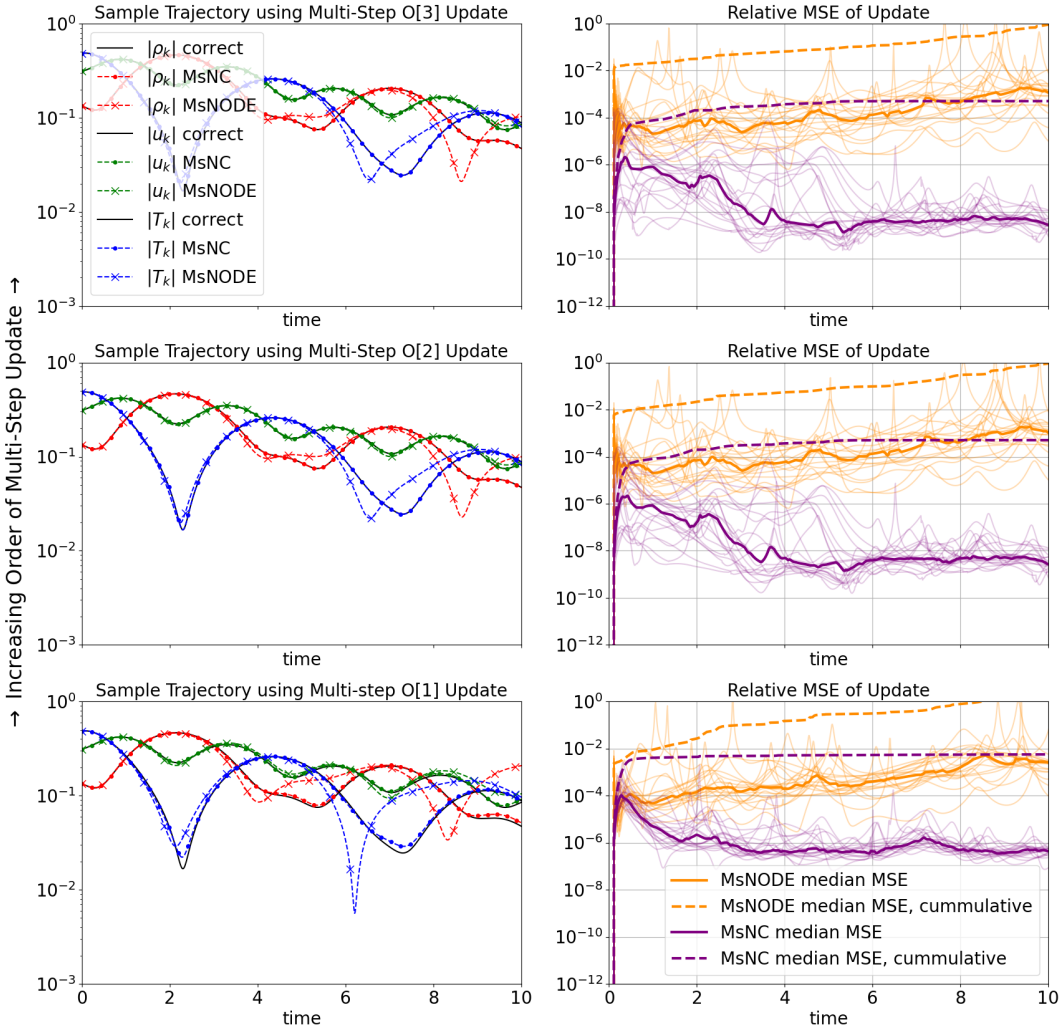

Figure 5A.1 Left: A sample trajectory of Grad's full equations Eq(5.1) updated with RK7, labeled as "correct", alongside a multi-step neural closure trajectory, labeled as MsNC, and a multi-step neural closure trajectory, labeled as MsNODE. The difference between the MsNODE trajectories and the correct trajectory is large enough to be visible. Right: The relative mean square error (MSE) incurred at each update for 20 different trajectories, plotted alongside the smoothed median error and cumulative smoothed median error. The plot demonstrates that the error decreases as the order of the multi-step update increases. This plots demonstrates that using a multi-step neural ODE to update the system leads to a growing relative error across all orders. Alternatively, the relative error decreases, across all orders, when conservation of mass, momentum, and energy is enforced.

CHAPTER 6

SUMMARY AND OUTLOOK

This dissertation begins by pointing out phenomena that are unique to plasmas and defining classification parameters that categorize different plasmas. Then we map the ρT space of hydrogen plasmas and spotlight the high energy density plasmas generated through inertial confinement fusion. We conclude the introduction by motivating the dissertation's major results in the context of high energy density plasmas. In particular, we highlight the demand for models of a plasma's dynamical response and the problems with existing models. We also emphasize that many HED plasmas manifest non-equilibrium conditions which violate the assumptions made in typical HED codes.

In chapter 2, we detail Hilbert's sixth problem and demonstrate, within the many body formalism, how to aggregate microscopic degrees of freedom into macroscopic degrees of freedom. In effect, we show how this aggregation gives rise to closures in molecular dynamics equations, kinetic equations, and fluid dynamics equations. The major results of this dissertation, which are all closures, are then presented in Chapter 3, Chapter 4, and Chapter 5.

In chapter 3, we start from the multi-component Bhatnagar-Gross-Krook kinetic equation and produce a multi-species susceptibility which conserves number and momentum, referred to as the "completed Mermin" susceptibility and explore its properties and uses. We show that the completed Mermin susceptibility satisfies the frequency sum rule. We apply the model to a carbon contaminated deuterium and tritium plasma at NIF direct drive hot spots nT conditions and find that momentum conservation qualitatively impacts the DSF's shape. In our appendices, we provide numerical implementations of the completed Mermin susceptibility for the reader's convenience. Further, we produce a new non-Drude conductivity model, by introducing free parameters on the number and momentum conservation terms of our completed Mermin susceptibility's single species limit. To illustrate how number and momentum conservation impact the dynamical conductivity shape, we apply our conductivity model to dynamical gold conductivity measurements [1]. Finally, comparing our model to the Drude-Smith conductivity model, we conclude that Smith's

phenomenological parameter violates local number conservation. To use this model, the collision rate and the inter-species potential must be supplied. Thus, the next step is to ascertain collision rates and potentials for a particular experiment and apply this model.

In chapter 4, we present a hybrid model which uses a buffer region to transition from a kinetic into a fluid description. Following the original work of Degond et al. [2], we extend the original method of Degond to flows with multiple particle species in 3D. We derive the coupled equations for the multispecies Bhatnagar-Gross-Krook model and its limiting Euler or Navier-Stokes hydrodynamic equations. In the buffer region, both the kinetic and hydrodynamic equations are solved simultaneously while being coupled via a so-called transition function. The transition function ensures a smooth conversion from the coupled model to either the kinetic or continuum approach at the interfaces of the buffer region. With that, the method avoids the need to find direct interface boundary conditions and allows one to localize the use of a high dimensional kinetic model only where it is needed. To validate our model numerically, we simulate a Sod shock problem. Then we apply the hybrid model to investigate kinetic multi-species mixing in the preheat phase of a high energy-density plasma physics experiment. We identify persistent velocity and temperature separation between the species and electro-diffusion at the interfaces. The next step for this work is to include this adaptive capability into our hybrid models. Degond et al. [3] have developed time dependent buffer regions allowing for adapative degrees of freedom.

In chapter 5, we employ Dynamic Mode Decomposition (DMD) [4] and dimension reduction techniques [5], to evaluate whether a closure steers a trajectory towards an invariant manifold and then remains on the slow manifold. These approaches complement previous analytic work done by Gorban and Karlin [6], providing visualizations of the equilibration to the invariant manifold and providing an alternative to evaluating constants of motion to assess whether the simulation is remaining on the invariant manifold. The findings from our data-driven analysis reveal that our neural closure can equilibrate towards a slow manifold, but the quality is inferior to Grad's closure. The next step for this work is to use these data-driven observations to regularize the cost function used to train the neural network.

BIBLIOGRAPHY

[1] Zhijiang Chen, CB Curry, R Zhang, F Treffert, N Stojanovic, S Toleikis, R Pan, M Gauthier, E Zapolnova, LE Seipp, et al. Ultrafast multi-cycle terahertz measurements of the electrical conductivity in strongly excited solids. *Nature communications*, 12(1):1638, 2021.

[2] Pierre Degond, Shi Jin, and Luc Mieussens. A smooth transition model between kinetic and hydrodynamic equations. *Journal of Computational Physics*, 209(2):665 – 694, 2005.

[3] Pierre Degond, Giacomo Dimarco, and Luc Mieussens. A moving interface method for dynamic kinetic-fluid coupling. *Journal of Computational Physics*, 227(2):1176 – 1208, 2007.

[4] Peter J Schmid. Dynamic mode decomposition of numerical and experimental data. *Journal of fluid mechanics*, 656:5–28, 2010.

[5] Sam T Roweis and Lawrence K Saul. Nonlinear dimensionality reduction by locally linear embedding. *science*, 290(5500):2323–2326, 2000.

[6] Alexander Gorban and Ilya Karlin. Hilbert's 6th problem: exact and approximate hydrodynamic manifolds for kinetic equations. *Bulletin of the American Mathematical Society*, 51(2):187–246, 2014.